

# Tropospheric Ozone Precursors: Global and Regional Distributions, Trends, and Variability

Yasin Elshorbany<sup>1\*</sup>, Jerald R. Ziemke<sup>2</sup>, Sarah Strode<sup>2,3</sup>, Hervé Petetin<sup>4</sup>, Kazuyuki Miyazaki<sup>5</sup>, Isabelle De Smedt<sup>6</sup>, Kenneth Pickering<sup>7</sup>, Rodrigo J. Seguel<sup>8</sup>, Helen Worden<sup>9</sup>, Tamara Emmerichs<sup>10</sup>, Domenico Taraborrelli<sup>10</sup>, Maria Cazorla<sup>11</sup>, Suvarna Fadnavis<sup>12</sup>, Rebecca R. Buchholz<sup>9</sup>, Benjamin Gaubert<sup>9</sup>, Néstor Y. Rojas<sup>13</sup>, Thiago Nogueira<sup>14</sup>, Thérèse Salameh<sup>15</sup>, Min Huang<sup>16</sup>

\*Correspondence to: elshorbany@usf.edu

<sup>1</sup> School of Geosciences, College of Arts and Sciences, University of South Florida, St. Petersburg, FL, USA

<sup>2</sup> NASA Goddard Space Flight Center, Greenbelt, Maryland, USA

<sup>3</sup> Goddard Earth Sciences Technology and Research (GESTAR II), Maryland, USA

<sup>4</sup> Earth Sciences Department, Barcelona Supercomputing Center, Barcelona, Spain

<sup>5</sup> Jet Propulsion Laboratory, California Institute of Technology, Pasadena CA

<sup>6</sup> BIRA-IASB, Ringlaan 3 Av. Circulaire, 1180 Brussels, Belgium

<sup>7</sup> Dept. of Atmospheric and Oceanic Science, University of Maryland, College Park, MD USA

<sup>8</sup> Center for Climate and Resilience Research, Department of Geophysics, Faculty of Physical and Mathematical Sciences University of Chile, Chile.

<sup>9</sup> Atmospheric Chemistry Observations and Modeling (ACOM), National Center for Atmospheric Research (NCAR), Boulder CO, USA.

<sup>10</sup> Institute of Energy and Climate Research, IEK-8: Troposphere, Forschungszentrum Jülich, Jülich, Germany.

<sup>11</sup> Universidad San Francisco de Quito USFQ, Instituto de Investigaciones Atmosféricas, Diego de Robles y Av Interoceánica, Quito, Ecuador.

<sup>12</sup> Center for Climate Change Research, Indian Institute of Tropical Meteorology, MoES, Pune, India.

<sup>13</sup> Department of Chemical and Environmental Engineering, Universidad Nacional de Colombia, Bogota, Colombia.

<sup>14</sup> University of São Paulo, São Paulo, Brazil.

<sup>15</sup> IMT Nord Europe, Institut Mines-Télécom, Univ. Lille, Centre for Energy and Environment, 59000, Lille, France.

<sup>16</sup> Earth System Science Interdisciplinary Center, University of Maryland, College Park, MD, USA.

36 **Abstract**

37 Tropospheric ozone results from in-situ chemical formation and stratosphere-troposphere  
38 exchange (STE), with the latter being more important in the middle and upper troposphere than in  
39 the lower troposphere. Ozone photochemical formation is nonlinear, and results from the oxidation  
40 of methane and non-methane hydrocarbons (NMHCs) in the presence of nitrogen oxide  
41 ( $\text{NO}_x = \text{NO} + \text{NO}_2$ ). Previous studies showed that  $\text{O}_3$  short- and long-term trends are nonlinearly  
42 controlled by near-surface anthropogenic emissions of carbon monoxide (CO), volatile organic  
43 compounds (VOCs), and nitrogen oxides. In addition, several studies have demonstrated the  
44 important role of STE in enhancing ozone levels, especially in the midlatitudes. In this article, we  
45 investigate tropospheric ozone spatial variability and trends from 2005 to 2019 and relate those to  
46 ozone precursors on global and regional scales. We also investigate the spatiotemporal  
47 characteristics of the ozone formation regime in relation to ozone chemical sources and sinks. Our  
48 analysis is based on remote sensing products of the Tropospheric Column of Ozone (TrC- $\text{O}_3$ ) and  
49 its precursors, nitrogen dioxide (TrC- $\text{NO}_2$ ), formaldehyde (TrC-HCHO), and total column of CO  
50 (TC-CO) as well as ozonesonde data and model simulations. Our results indicate a complex  
51 relationship between tropospheric ozone column levels, surface ozone levels, and ozone  
52 precursors. While the increasing trends of near-surface ozone concentrations can largely be  
53 explained by variations in VOC and  $\text{NO}_x$  concentration under different regimes, TrC- $\text{O}_3$  may also  
54 be affected by other variables such as tropopause height and STE. Decreasing or increasing trends  
55 in TrC- $\text{NO}_2$  have varying effects on the TrC- $\text{O}_3$ , which is related to the different local chemistry  
56 in each region. We also shed light on the contribution of  $\text{NO}_x$  lightning and soil NO and nitrous  
57 acid (HONO) emissions to trends of tropospheric ozone on regional and global scales.

58

## 59 1. Introduction

60 Tropospheric ozone ( $O_3$ ) is an important air pollutant due to its diverse effects on air quality,  
61 ecosystem (Mills et al., 2018), health (Lefohn et al., 2018; Fleming et al., 2018), and climate  
62 (Boucher et al., 2013; Myhre et al., 2013; Zanis et al., 2022).  $O_3$  is a photochemical product  
63 that results from the oxidation of methane ( $CH_4$ ) and non-methane hydrocarbons (NMHCs) in  
64 the presence of nitrogen oxides ( $NO_x$ ). Tropospheric ozone burdens can also be affected by  
65 stratosphere-troposphere exchange (STE) (Stohl et al., 2003; Zeng et al., 2010; Trickl et al.,  
66 2011; Li et al., 2024).  $O_3$  is considered a short-lived climate forcer (SLCF) and is the third-  
67 most important greenhouse gas with an effective radiative forcing of  $(0.47^{+0.23}_{-0.23}) \text{ W m}^{-2}$ ;  
68 Forster et al., 2021). Since the mid-1990s, free tropospheric ozone trends based on in situ  
69 measurement and satellite retrievals have increased with high confidence by  $1\text{--}4 \text{ nmol mol}^{-1}$   
70  $\text{decade}^{-1}$  across the northern mid-latitudes and  $1\text{--}5 \text{ nmol mol}^{-1} \text{ decade}^{-1}$  within the tropics  
71 (Gulev et al., 2021). In the Southern Hemisphere, with more limited observation coverage  
72 compared with the Northern Hemisphere, the tropospheric column ozone shows an increase  
73 since the mid-1990s by less than  $1 \text{ nmol mol}^{-1} \text{ decade}^{-1}$  with medium confidence at southern  
74 mid-latitudes (Gulev et al., 2021, Cooper et al., 2020). Tropospheric  $O_3$  short- and long-term  
75 trends are nonlinearly controlled by anthropogenic emissions of carbon monoxide (CO),  
76 volatile organic compounds (VOCs), and nitrogen oxides ( $NO_x=NO+NO_2$ ) as well as STE,  
77 especially in the midlatitudes (Li et al., 2024). Coupled Model Intercomparison Project Phase  
78 6 (CMIP6) overestimates observed surface  $O_3$  concentrations in most regions, with larger  
79 variability over Northern Hemisphere (NH) continental regions (e.g., Tarasick et al., 2019;  
80 Turnock et al., 2020). CMIP6 models simulate large increasing trends of surface concentrations  
81 of  $O_3$  and  $PM_{2.5}$  in East and South Asia with an annual mean increase of up to 40 ppb and 12  
82  $\mu\text{g m}^{-3}$ , respectively, over the historical periods (1850-2014; Turnock et al., 2020). However,  
83 these studies found also that CMIP6 models consistently underestimate  $PM_{2.5}$  concentrations  
84 in the NH, especially during the winter months, and with larger variability near natural source  
85 regions, indicating missing sources (e.g., HONO) of  $O_3$  (e.g., Elshorbany et al., 2014). Future  
86 scenarios show that emission control measures can influence future changes to air pollutants.  
87 Although the global increases in  $CH_4$  abundance may offset benefits to surface  $O_3$  from local  
88 emission reductions (Fiore et al., 2002; Shindell et al., 2012; Wild et al., 2012), recent reports  
89 (e.g., Zanis et al., 2022), showed the dominant role of precursor emission changes in projecting  
90 surface ozone concentrations under future climate change scenarios. In this study, we  
91 investigate the relation between ozone trends and the trends of its precursors.

92 Satellite observations have the advantage of large spatial and consistent temporal coverage.  
93 Tropospheric columns of ozone ( $\text{TrC-O}_3$ ), in Dobson unit ( $1 \text{ DU}=2.69\times 10^{20} \text{ molecules m}^{-2}$ ),  
94 are usually used to represent tropospheric ozone levels. The tropospheric column of a species  
95 is the species' concentration integrated from the surface to the top of the troposphere, the  
96 tropopause. The tropopause height is dynamically changing, and it varies over time, increasing  
97 or decreasing as a function of several factors, including tropospheric and stratospheric  
98 temperature (warming or cooling). Steinbrecht et al (1998) found that observed tropospheric  
99 warming of  $0.7\pm 0.3 \text{ K per decade}$  leads to an increase in the tropopause high and a decrease  
100 (at a rate of  $16 \text{ DU/decade}$ ) in the observed column ozone levels. Similarly, after removing the  
101 variations related to major natural forcings, including volcanic eruptions, ENSO (El Niño–  
102 Southern Oscillation), and QBO (Quasi–Biennial Oscillation), Meng et al. (2021) concluded  
103 that a continuous rise of the tropopause in the Northern Hemisphere (NH) from 1980 to 2020  
104 is evident, which they related mainly to tropospheric warming caused by anthropogenic  
105 emissions. Steinbrecht et al (1998) and Meng et al. (2021) calculate the same rate of tropopause

106 increase for the periods 1980-2000 and 1980-2020, respectively. We investigate the trends in  
107 TrC-O<sub>3</sub> and ozone precursors at different column depths and determine their relationships.

108 Global models play a vital role in interpreting the observed trends in ozone precursors,  
109 verifying the consistency of emission inventories with observed precursor concentrations, and  
110 relating trends in ozone precursor emissions to ozone trends. Because satellite measurements  
111 are often sensitive to species concentrations above the surface, models provide additional  
112 information on the vertical distribution of ozone precursors needed to relate emissions or  
113 surface trends to a column or free tropospheric observations. For example, chemical transport  
114 models are used to relate Ozone Monitoring Instrument (OMI) NO<sub>2</sub> columns to surface NO<sub>2</sub>  
115 concentrations and their trends over the United States (e.g. Lamsal et al 2008, 2015; Kharol et  
116 al, 2015) since they provide vertical information on the NO<sub>2</sub> distribution. Models are also used  
117 to infer NO<sub>x</sub> emission trends from observations (e.g. Richter et al., 2005; Stavrou et al.,  
118 2008; Miyazaki et al, 2016) or to examine whether simulations driven by state-of-the-art  
119 emissions inventories can reproduce observed changes in NO<sub>x</sub> (Itahashi et al., 2014;  
120 Godowitch et al, 2010). Models also provide insight into the role of background NO<sub>2</sub> versus  
121 local sources in relating satellite-observed NO<sub>2</sub> columns to NO<sub>x</sub> emissions changes (Silvern et  
122 al, 2019). Similarly, global models are vital for understanding trends in CO, since the lifetime  
123 of CO allows both local emissions and long-range transport and the global background to  
124 influence regional trends of CO and O<sub>3</sub>. Duncan and Logan (2008) attributed the decreasing  
125 CO in the NH from 1998-1997 to decreasing European emissions and highlighted the role of  
126 Indonesian fires in driving interannual variability. Numerical models can also be used to  
127 assimilate satellite CO observations to invert for CO emission fluxes, often highlighting  
128 differences between bottom-up and top-down inventories (e.g., Kopacz et al., 2010; Fortems-  
129 Cheiney et al., 2011; Elguindi et al., 2020; Gaubert et al., 2020). For instance, several modeling  
130 studies found that the increasing emissions from China in recent years in some emission  
131 inventories were inconsistent with the negative trends observed by MOPITT (Yin et al, 2015;  
132 Strode et al., 2016; Zheng et al, 2019), while the decreases over the United States and Europe  
133 are supported by the observed decrease in CO. Jiang et al (2017) and Zheng et al (2019) also  
134 found that a decrease in biomass burning contributes to the negative CO trend in the NH. Mean  
135 calculated O<sub>3</sub> burden using CMIP6 simulation (Griffiths et al, 2021) revealed an increase of  
136 44% from 1850 to the mean of the period of 2005-2014 and by another 17% until 2100 using  
137 the SSP370 experiments. Other sources of NO<sub>x</sub> such as lightning and soil emissions play an  
138 important role in controlling the O<sub>3</sub> budget, especially in low-NO<sub>x</sub> regions. We investigate  
139 these sources and the role they play in determining O<sub>3</sub> trends and variability on regional and  
140 global scales, as well as their determining factors.

141 Previous literature demonstrates the importance of controlling the emissions of ozone  
142 precursors to effectively reduce surface O<sub>3</sub> levels. Therefore, a thorough and rigorous  
143 understanding of the trends and variability for O<sub>3</sub> precursors is of paramount importance for a  
144 global abatement strategy of O<sub>3</sub> levels. In this study, we use ozonesonde, remote sensing, and  
145 global models to evaluate tropospheric O<sub>3</sub> and O<sub>3</sub> precursor trends of CO, HCHO, and NO<sub>2</sub>,  
146 on regional and global scales.

## 147 **2. Methodology**

### 148 **2.1. Trend Analysis**

149 We analyze the historical trends of tropospheric ozone and its precursors CO, NO<sub>2</sub>, and HCHO,  
150 from 2005 to 2019. For trend analysis, we use two methods, the Quantile regression (QR)  
151 method (Chang et al., 2023), and the Weighted Least Squares (WLS). For NO<sub>2</sub>, CO, and HCHO

152 trends are calculated based on the QR method (Chang et al., 2023), as follows: (1) we first  
 153 compute the deseasonalized monthly time series of NO<sub>2</sub> and HCHO tropospheric columns  
 154 (hereafter referred to as TrC-NO<sub>2</sub>, TrC-HCHO), and CO atmospheric column (TC\_CO), (2) we  
 155 use the quantile regression method for computing the trend, focusing here on the median, and (3)  
 156 uncertainties at a 95% confidence level are estimated using the block bootstrapping approach,  
 157 through 1000 iterations with blocks size of  $N^{0.25}$  with N the number of monthly values. They are  
 158 calculated over a 1°x1° grid and only in cells where at least 75% of the monthly values are  
 159 available. TC\_CO column (see sec. 2.2.1) time series trends are also calculated as Weighted  
 160 Least Squares (WLS) of the monthly anomaly, weighted by the monthly regional standard  
 161 deviation (for comparison with the QR method). The tropospheric ozone column (TrC-O<sub>3</sub>),  
 162 trends are calculated based on the WLS method. Tropospheric columns of satellite observations  
 163 are calculated based on the WMO thermal definition of the tropopause. To account for varying  
 164 tropospheric column definitions used in previous literature, we also evaluate the trends at varying  
 165 column depths.

## 166 2.2. Data resources

167 In this section, we present the different data repositories and their characteristics.

### 168 2.2.1. Satellite data

169 A list of the applied satellite data products and their resolution is shown in [Table 1](#). For  
 170 Tropospheric ozone data, we use the Ozone Monitoring Instrument/Microwave Limb Sounder  
 171 (OMI/MLS) product (Ziemke et al., 2006). The OMI/MLS product is the residual of the OMI total  
 172 ozone column and the MLS stratospheric ozone column, available as gridded monthly means. The  
 173 tropospheric NO<sub>2</sub> column retrievals used were the QA4ECV project (<http://www.qa4ecv.eu/ecvs>)  
 174 version 1.1 level 2 (L2) product for OMI (Boersma et al., 2017a), GOME-2 (Boersma et al.,  
 175 2017b), and SCIAMACHY (Boersma et al., 2017c). The ground pixel sizes of the OMI, GOME-  
 176 2, and SCIAMACHY retrievals are 13 km×24 km, 80 km×40 km, and 60 km×30 km, with local  
 177 Equator overpass times of 13:45, 09:30, and 10:00 LT, respectively. We also use HCHO  
 178 tropospheric columns retrieved from OMI (De Smedt et al. 2018) from the QA4ECV project.  
 179 Atmospheric total column CO daytime observations were obtained from the MOPITT instrument  
 180 aboard the Terra Satellite (Barret et al., 2003; Buchholz et al., 2017). Monthly daytime L3 data  
 181 were obtained at 1° gridded horizontal resolution from the NASA Langley Research Center  
 182 Atmospheric Science Data Center (ASDC, 2024), using version 9 (V9) retrievals, and the joint  
 183 near-infrared/thermal-infrared product (Deeter et al., 2022).

184

185 Table 1 Satellite data products and their reference periods.

Parameter	Resolution (Satellite pixel size)	Instrument/Platform	Reference Period	Reference
NO <sub>2</sub>	1°x1° (13 km x 24 km)	OMI/Aura	2005–2020	Boersma et al., 2017a
NO <sub>2</sub>	1°x1°	GOME-2/METOP-A	2007–2018	Boersma et al., 2017b

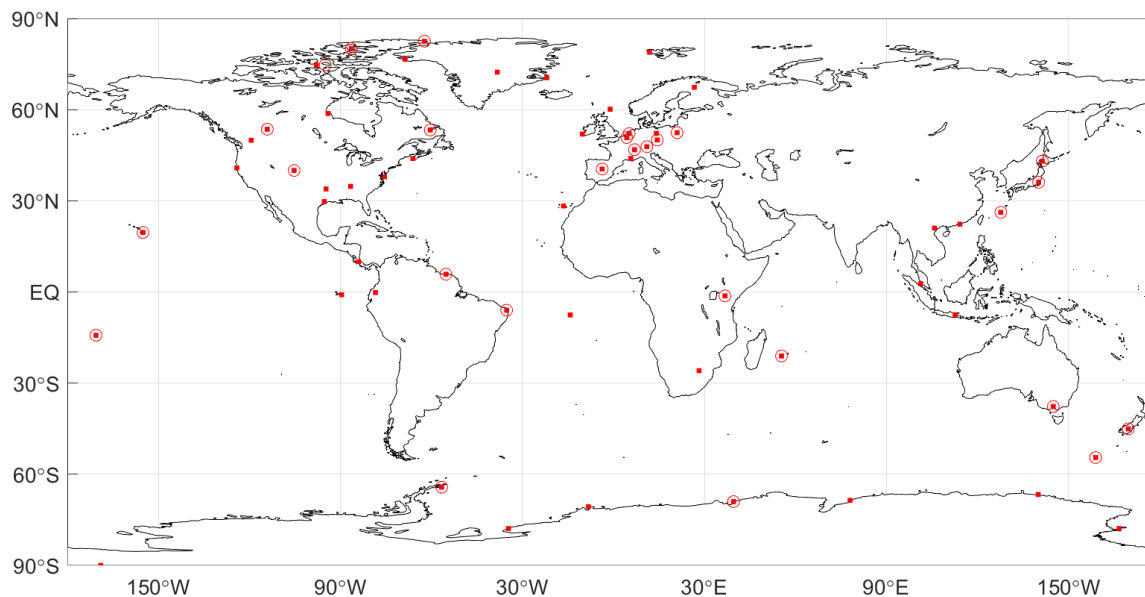
Parameter	Resolution (Satellite pixel size)	Instrument/Platform	Reference Period	Reference
	(40 km x 80 km)			
NO <sub>2</sub>	1°x1° (30 km x 60 km)	SCIAMACHY/ENVISAT	2005–2011	Boersma et al., 2017c
CO	1°x1° (22 km x 22 km)	MOPITT/TERRA	2002–2020	Deeter et al., 2022
HCHO	1°x1° (13 km x 24 km)	OMI/Aura	2004–2020	De Smedt et al., 2018
Ozone	1°x1°	OMI/MLS	2004–2020	Ziemke et al., 2006

186

### 187 2.2.2. Ozonesonde Data

188 Direct sampling of ozone throughout the atmospheric column by ozonesondes on board of high-  
189 altitude balloons is a primary source of information of the ozone abundance and changes in the  
190 free troposphere. Ozonesonde data have been used extensively for satellite ozone product  
191 validations, trend analyses, and as a priori climatology profiles for satellite retrieval algorithms  
192 (McPeters and Labow, 2012; Labow et al., 2015; Hubert et al., 2021; Christiansen et al., 2022;  
193 Newton et al., 2016). Ozonesondes networks around the globe have been providing the ozone  
194 community with accurate in situ measurements of high vertical resolution (100-m) for the last 5  
195 decades in the Northern Hemisphere (Krizan and Lastovicka, 2005), nearing 3 decades at  
196 stations in the tropics (Thompson et al., 2017), and in the last decade, new efforts are  
197 contributing with data from undersampled regions such as the tropical Andes (Cazorla and  
198 Herrera, 2022). Other important contributions include dedicated campaigns for regional studies  
199 (e.g. Newton et al., 2016; Fadnavis et al., 2023). [Figure 1](#) shows a map with ozonesonde stations  
200 around the globe whose data are publicly available from data providers (station names,  
201 coordinates, and links for data access in the Supplementary Material, Table S1). In this work, we  
202 present a review of ozonesonde trends calculated and published in previous studies (Wang et al.,  
203 2022 and Christiansen et al., 2022).

204



205  
 206 Figure 1: Ozone-sounding stations around the globe (red squares) whose data are publicly  
 207 available (Table S1). Stations that meet the criteria to calculate trends (Wang et al., 2022) are  
 208 circled in red.

209  
 210 **2.2.3. Model simulations of ozone precursors and their vertical distribution**

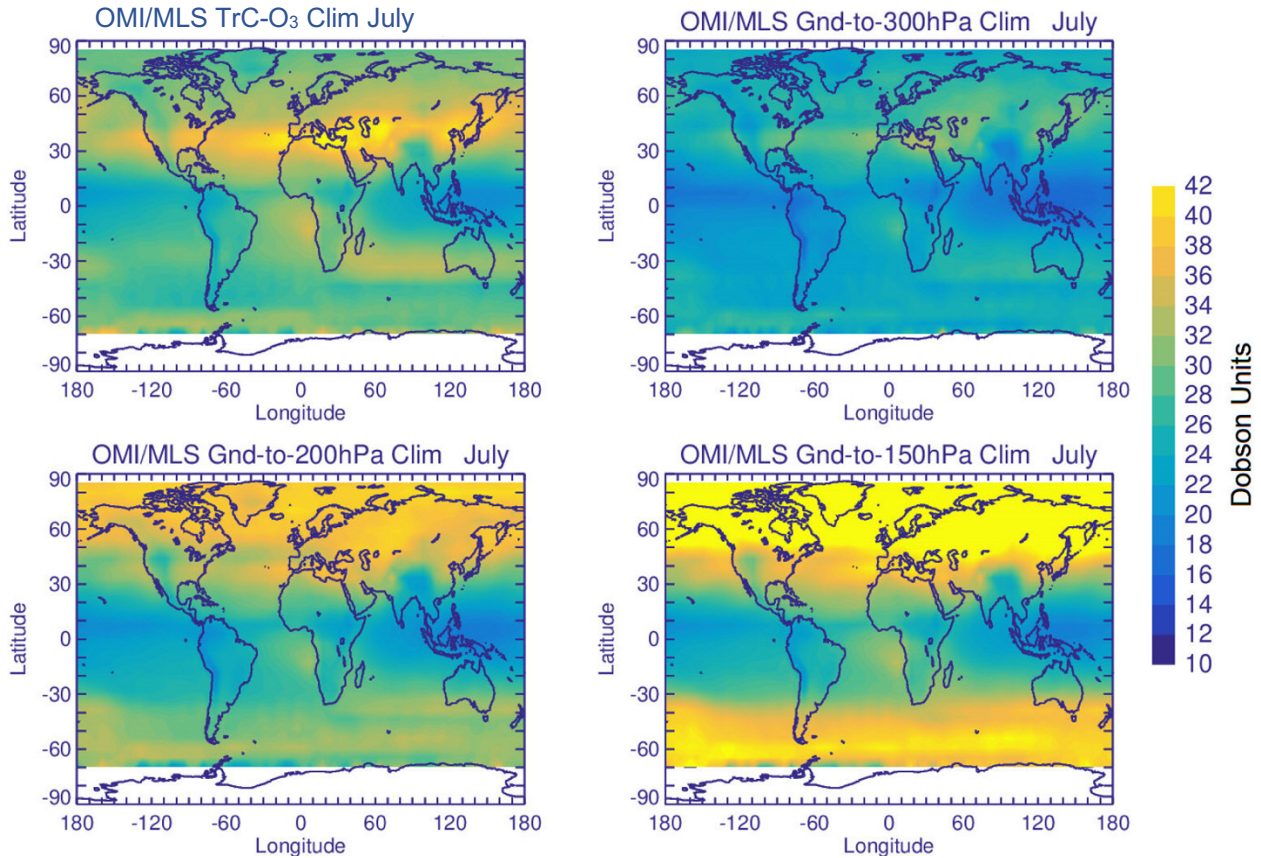
211 Model simulations provide information on the vertical distribution of trace gases that can help  
 212 interpret the observed columns. Here, we use a Goddard Earth Observing System (GEOS) Earth  
 213 System Model (Molod et al, 2015) simulation run with the GMI chemistry mechanism (Duncan  
 214 et al, 2007; Strahan et al, 2007; Nielsen et al, 2017) to simulate the contributions of the lower,  
 215 middle, and upper troposphere to the tropospheric columns of ozone and its precursors. The  
 216 model configuration is described in Fisher et al (2024) and summarized here. The MERRA-2  
 217 reanalysis (Gelaro et al., 2017) constrains the GEOS-GMI meteorology. The GEOS-GMI  
 218 meteorology is replayed to the MERRA-2 meteorology as described in Orbe et al (2017).  
 219 Anthropogenic emissions of NO<sub>2</sub>, CO, and VOCs are based on the MACCity inventory (Granier  
 220 et al, 2011) through 2010 and the RCP8.5 emissions afterward, with NO<sub>2</sub> emissions scaled based  
 221 on OMI. The emissions are downscaled to higher resolution using the EDGAR 4.2 emission  
 222 inventory (Janssens-Maenhout et al., 2013). Biomass burning emissions for the analysis period  
 223 come from the Fire Energetics and Emissions Research (FEER) product (Ichoku and Ellison,  
 224 2014). Liu et al (2022) evaluated another GEOS simulation with GMI chemistry with satellite  
 225 observations of TrC-O<sub>3</sub>, TrC-NO<sub>2</sub>, TrC-HCHO, and TC-CO.

226 **3. Data Analysis and Discussion**

227 **3.1. TrC-O<sub>3</sub> Sensitivity to Tropopause**

228 Calculated TrC-O<sub>3</sub> depends on several factors such as tropospheric ozone levels, atmospheric  
 229 warming (e.g., due to GHG emissions) or cooling (stratospheric or tropospheric (e.g., after major  
 230 volcanic eruptions), and tropopause height (TH). Atmospheric warming or cooling can lead to a  
 231 decrease or an increase, respectively, of TrC-O<sub>3</sub> due to the respective change in the TH. Several  
 232 methods are used to determine the TH. The WMO thermal definition for the first TH, the lowest  
 233 altitude level at which the lapse rate decreases to 2° K km<sup>-1</sup> or less, provided that the average  
 234 lapse rate between this level and all higher levels within 2 km does not exceed 2° K km<sup>-1</sup>. A

235 second tropopause may be also found if the lapse rate above the first tropopause exceeds  $3^{\circ}\text{K}$   
 236  $\text{km}^{-1}$  (WMO, 1992; Hoffmann and Spang (2022). Other studies define the TH based on fixed  
 237 pressure levels (from ground to 150, 200, 300, and 400 hPa). Mean OMI/MLS TrC-O<sub>3</sub> values in  
 238 July (2005-2019) calculated based on the WMO thermal definition, are shown in [Figure 2](#). TrC-  
 239 O<sub>3</sub> values are comparable to previously reported CMIP6 and satellite measurements (Griffiths et  
 240 al., 2021). Partial ozone columns (OC) calculated from the ground to different pressure levels,  
 241 150, 200, and 300 hPa show increasing OC values with increasing column depth, with calculated  
 242 OC at 150 and 200 hPa being the closest to the TrC-O<sub>3</sub> WMO values, still overestimating OC in  
 243 the northern hemisphere (50-90° N), especially for the 150 hPa OC, see [Figure 2](#).  
 244



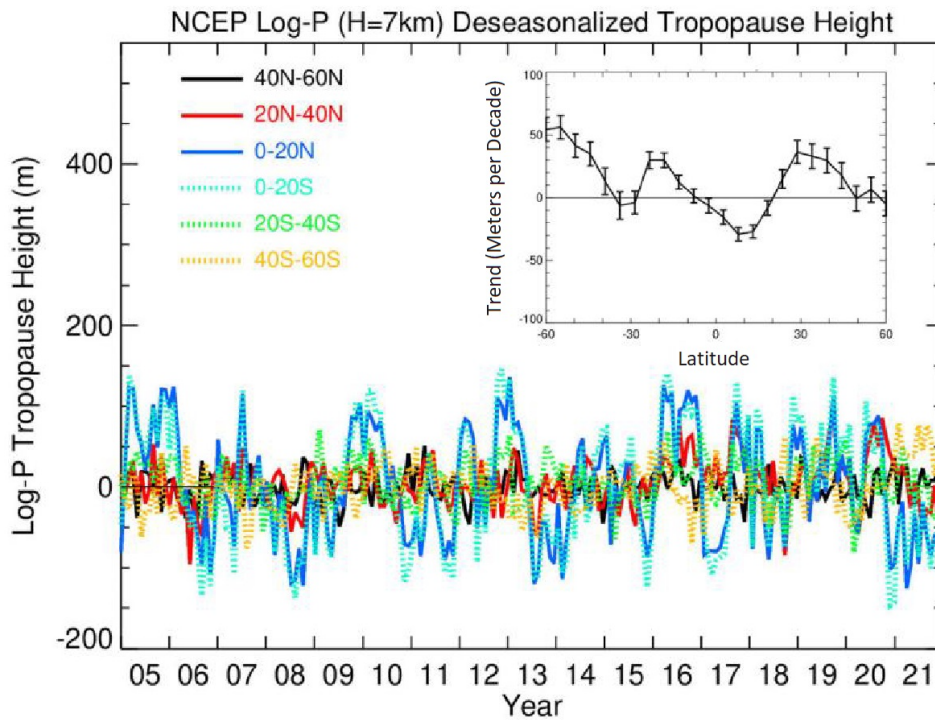
245  
 246 Figure 2: Global Mean (2005-2019) Column Ozone based on the WMO definition, and for  
 247 different column depths.

248  
 249 Steinbrecht et al (1998) found that observed tropospheric warming of  $0.7 \pm 0.3$  K per decade  
 250 leads to an increase in the TH and a decrease in total ozone. They also calculated a decrease of  
 251 16 DU per kilometer increase in TH. These results indicate the importance of TH on calculated  
 252 long-term ozone trends. This could also affect comparisons between trends calculated based on  
 253 different TrC-O<sub>3</sub> definitions and near-surface ozone levels. The time series of deseasonalized TH  
 254 from 2004 to 2021 are shown in [Figure 3](#) together with their zonal mean trends. Trends in TH are  
 255 positive reaching 60 meters/decade except in a narrow band in the tropics from 10°S to 20°N and  
 256 at 30°S, where TH decreases at a rate up to 30 meters/decade. TH in the tropical regions is also  
 257 characterized by high variability (see [Figure 3](#)). These results are also consistent with recent  
 258 reports showing a positive trend of TH from 20-80°N at a rate of 50-60 m/decade (Meng et al.,



259 2021). They related this increase primarily to tropospheric warming. These results show that  
 260 using a fixed pressure level for the tropopause may not be accurate given the change in TH over  
 261 time. In the following sections, tropospheric columns will be calculated based on the WMO  
 262 tropopause definition.

263



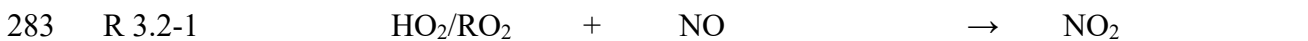
264

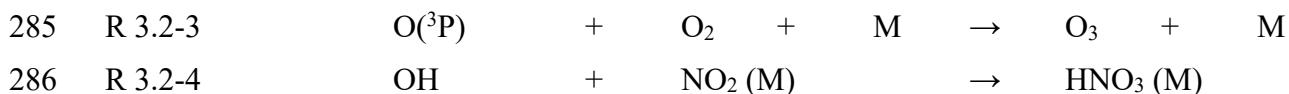
265 Figure 3: National Centers for Environmental Prediction (NCEP) WMO (2K/km) tropopause  
 266 log-P height time series with trends (meters/decade) embedded.

267

### 268 3.2. Spatial Distribution of O<sub>3</sub> and its Precursors

269 Tropospheric O<sub>3</sub> results from in-situ photochemical formation and STE. In-situ O<sub>3</sub> results from  
 270 the photolysis of NO<sub>2</sub>. Therefore, the sources and fate of NO<sub>2</sub> in the atmosphere determine O<sub>3</sub>  
 271 burden and distribution. NO<sub>2</sub> is formed from the reaction of hydrogen peroxy (HO<sub>2</sub>) and alkyl  
 272 peroxy (RO<sub>2</sub>) radicals with NO ([R 3.2-1](#)). While photolysis of NO<sub>2</sub> is the main source of ozone,  
 273 high NO<sub>2</sub> levels can suppress O<sub>3</sub> levels as NO<sub>2</sub> reacts with OH radical forming HNO<sub>3</sub> ([R 3.2-2](#) to  
 274 [R 3.2-4](#)), thus reducing the oxidation rate of hydrocarbons and respectively HO<sub>2</sub> and RO<sub>2</sub> levels,  
 275 leading to a net loss of O<sub>3</sub> (e.g., Finlayson-Pitts and Pitts, 2000; Elshorbany et al., 2010,  
 276 Archibald et al., 2020). Ozone production efficiency is calculated as the ratio of the number of  
 277 NO<sub>2</sub> molecules photolyzed to form O<sub>3</sub> to that lost due to the reaction with OH forming HNO<sub>3</sub>.  
 278 Under NO-sensitive conditions, the decrease in NO<sub>x</sub> leads to a reduction in OH, HCHO, and O<sub>3</sub>.  
 279 However, under high NO conditions, a reduction in NO<sub>x</sub> could lead to an increase in  
 280 photochemical products, OH, HCHO, and O<sub>3</sub> because a reduction in NO<sub>2</sub> leads to a decrease in  
 281 OH loss rate, thus higher HO<sub>2</sub> and RO<sub>2</sub> production (Elshorbany et al., 2012; Archibald et al.,  
 282 2020).



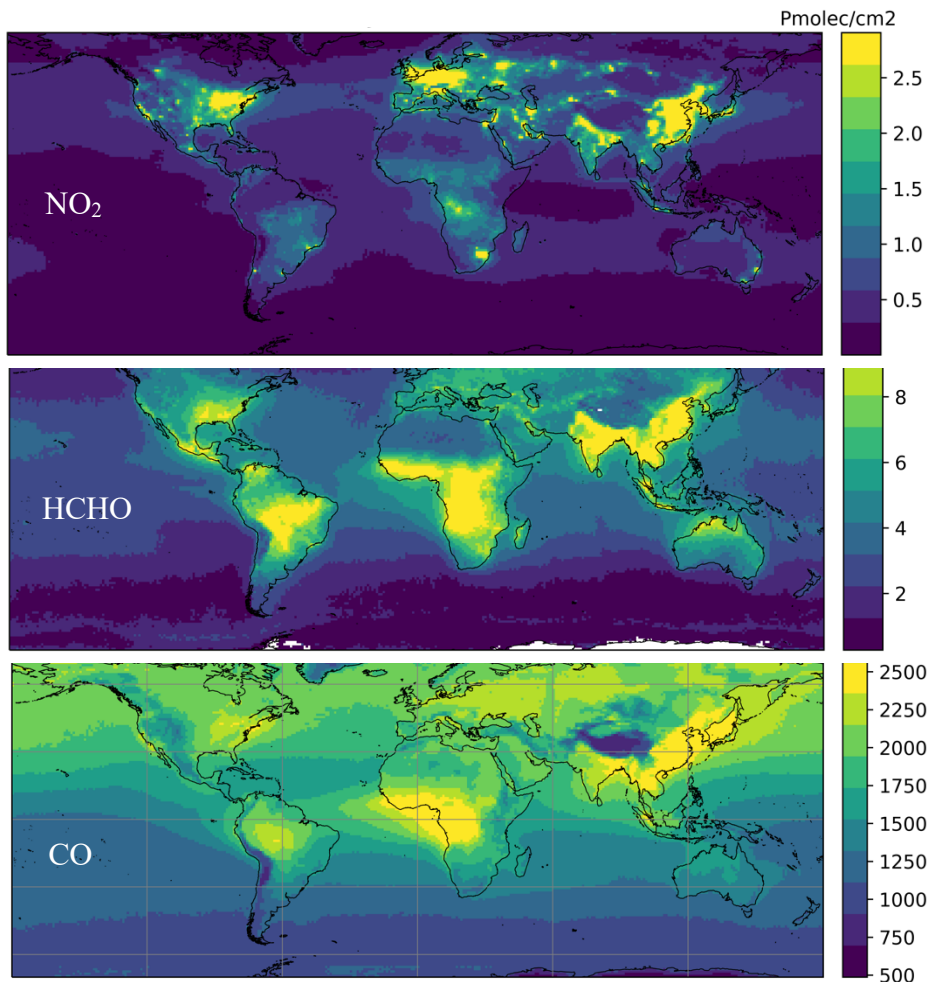
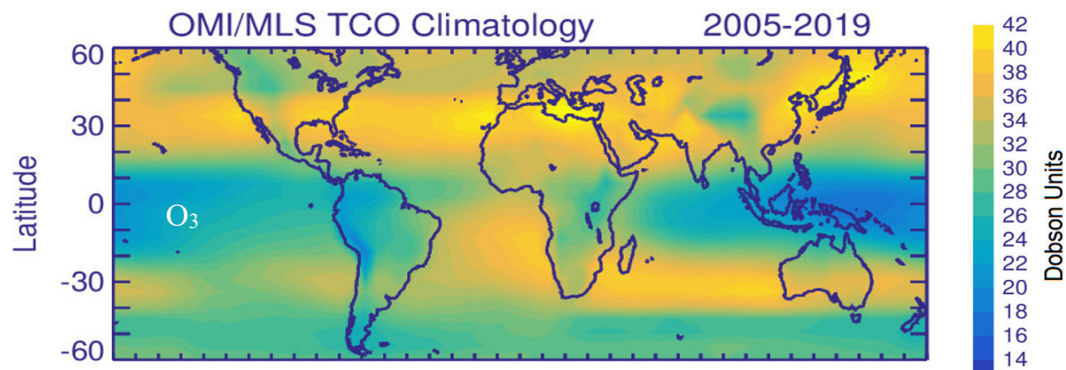


287

288 While this paper focuses on ozone precursors with higher reactivity, we note that methane, with  
 289 an assessed total atmospheric lifetime of  $9.1 \pm 0.9$  years (Szopa et al., 2021), is also a crucial  
 290 driver (Fiore et al., 2002; Isaksen et al., 2014), given its accelerated growing rate of  $7.6 \pm 2.7$   
 291  $nmol\ mol^{-1}\ yr^{-1}$  between 2010 and 2019 (Canadell et al., 2021), largely driven by anthropogenic  
 292 activities (Szopa et al., 2021).

293 The observed mean tropospheric columns of  $O_3$ ,  $NO_2$ , and HCHO and atmospheric column of  
 294 CO from 2005 to 2019 are shown in [Figure 4](#). The unit for column number density is  
 295  $Pmolec/cm^2$  ( $\times 10^{15}$  molecules per square centimeter), except for TrC- $O_3$ , which is Dobson.  $NO_2$   
 296 concentration has decreased since 2005 in North America, Europe, and Australia, mainly due to  
 297 strict measures to reduce air pollution (Lamsal et al., 2015). Since  $O_3$  is a photochemical product  
 298 that is formed based on non-linear chemistry, a reduction in  $NO_2$  may lead to an increase or  
 299 decrease in tropospheric  $O_3$  levels based on the dominant photochemical regime in the respective  
 300 region. In addition, tropospheric ozone levels, especially in the middle and upper troposphere  
 301 may be affected by STE (Li et al., 2024). The highest values of the  $NO_2$  tropospheric column are  
 302 in the northern hemisphere between  $10^\circ N$  and  $50^\circ N$ , especially over the eastern US, northern  
 303 Europe, and east and south Asia, with elevated levels in the Southern Hemisphere (SH) between  
 304  $10$  and  $30^\circ S$ , especially in sub-Saharan Africa, and Brazil. TrC- $O_3$  is also highest over the band  
 305 of  $20$ - $50^\circ N$ , especially over the eastern coast of the US, southern Europe, and east Asia. Some  
 306 differences exist between TrC- $O_3$  and TrC- $NO_2$  spatial patterns which is due to factors including  
 307 different lifetime, photochemical sensitivity (see sec. 3.4), and STE. On average, the northern  
 308 hemisphere has higher TC-CO than the southern hemisphere due to a larger number of sources  
 309 (Buchholz et al., 2021). Additionally, high amounts of CO are found in regions with large  
 310 anthropogenic sources (e.g., eastern China) or in regions with large and regular fire seasons (e.g.,  
 311 central Africa) (Buchholz et al., 2021). HCHO and CO show a similar spatial pattern over  
 312 western Africa due to emissions from biomass burning (Marais et al., 2012, Buchholz et al.,  
 313 2021). In the following sections, global and regional trends of TrC- $O_3$  are investigated along  
 314 with tropospheric ozone precursors.

315

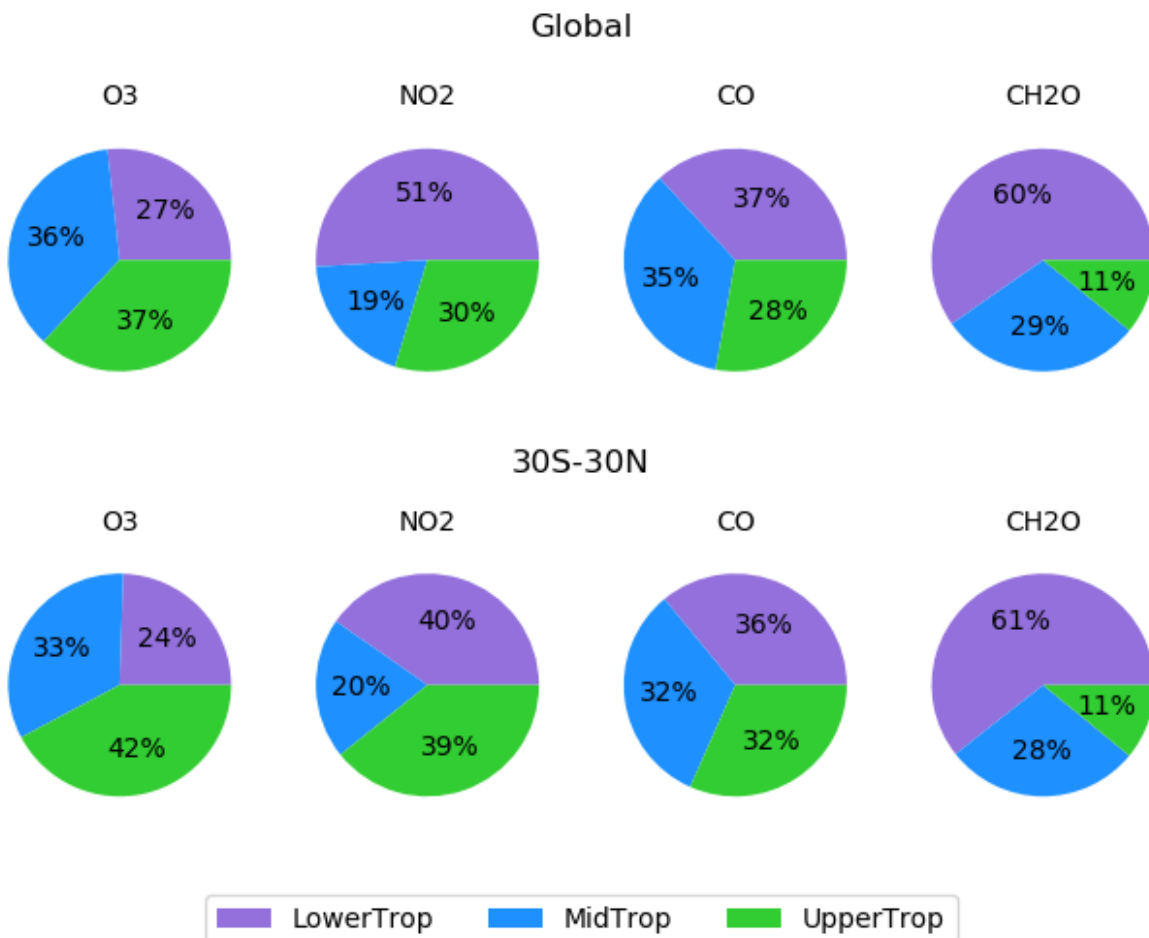


316  
 317 Figure 4: Mean (2005-2019) of TrC-O<sub>3</sub>, TrC-NO<sub>2</sub>, TrC-HCHO, and TC-CO.

318 **3.3. Simulated O<sub>3</sub> Precursors**

319 Ozone and its precursors differ in their vertical distribution through the troposphere. In this  
 320 section, we use the GEOS -simulations to show how the lower, middle, and upper troposphere  
 321 contribute to the simulated columns of O<sub>3</sub> and its precursors to complement the column  
 322 information from satellites. [Figure 5](#) shows the simulated mean (2005-2019) contributions to  
 323 tropospheric columns of O<sub>3</sub>, NO<sub>2</sub>, formaldehyde, and CO, partitioned into the lower (up to  
 324 700hPa), middle (700-400hPa), and upper (400hPa to tropopause) portions of the troposphere for  
 325 the tropical band (30°S:30°N) and the global mean. The middle and upper troposphere make

326 large contributions to the simulated TrC-O<sub>3</sub> and its variability (Figure 5). The lower troposphere  
 327 makes the largest contribution to the TrC-HCHO since it is mainly a photochemical product  
 328 (e.g., Elshorbany et al., 2009), and all three levels make substantial contributions to the CO  
 329 column. Globally, the relative contributions for TrC-O<sub>3</sub>, TrC-HCHO and CO are similar to those  
 330 of the tropics. However, for TrC-NO<sub>2</sub> the lower troposphere makes a smaller contribution in the  
 331 tropics than globally.  
 332



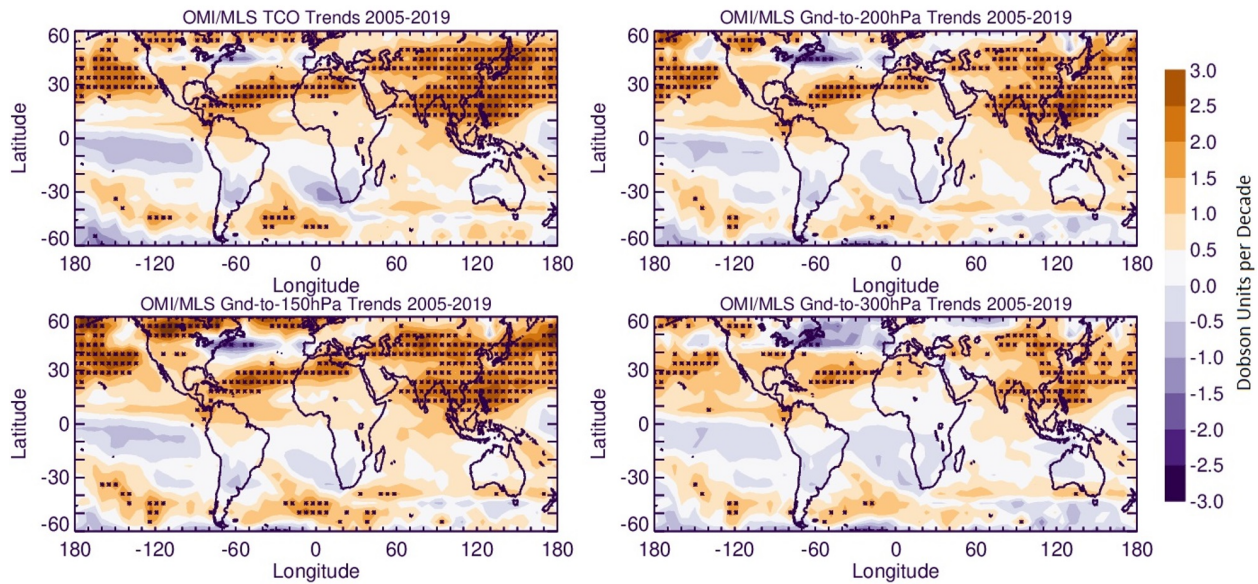
333  
 334 Figure 5: Simulated average (2005-2019) contributions to the tropospheric columns of O<sub>3</sub>, NO<sub>2</sub>,  
 335 formaldehyde, and CO from the lower (surface-700hPa), middle (700-400hPa), and upper  
 336 troposphere (400hPa-tropopause) using NASA GEOS-GMI. The top row is for the global mean,  
 337 while the bottom row is averaged from 30°S-30°N.

### 338 3.4. Tropospheric Trends

#### 339 3.4.1. Global Tropospheric Ozone

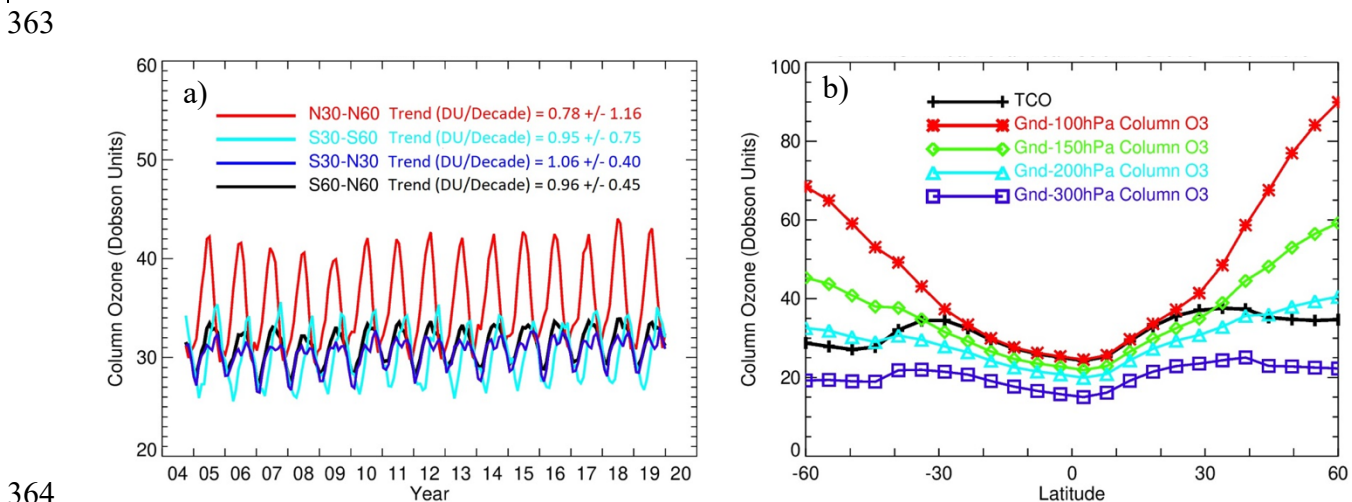
340 Global TrC-O<sub>3</sub> trends calculated for different column depths are shown in Figure 6. Compared to  
 341 TrC-O<sub>3</sub>, OC trends up to 150 hPa seem to be the closest despite OC values being much higher  
 342 than that of the TrC-O<sub>3</sub> (Figure 2). All significant trends are positive indicating increasing trends  
 343 of ozone columns, regardless of the tropopause height. Insignificant (at 2  $\sigma$  levels) decreasing  
 344 TrC-O<sub>3</sub> trends were also found in some locations, e.g., South Australia, South Africa, and the

345 northeastern coast of the US. Increasing trends in the northern midlatitudes may also be partially  
 346 related to STE (Willimas et al, 2019; Li et al., 2024)



347  
 348 Figure 6: Trends in tropospheric column ozone, based on the WMO thermal definition, and the  
 349 trends on ozone columns (from ground to 150, 200, and 300 hPa). Trends are calculated based on  
 350 deseasonalized monthly data from 2005 to 2019. Asterisks denote significant trends (different  
 351 from zero at  $2\sigma$  level).

352  
 353 The time series of OMI/MLS TrC-O<sub>3</sub> averaged over several latitudinal bands and at different  
 354 column depths are shown in [Figure 7](#). Zonal mean TrC-O<sub>3</sub> compares well with partial ozone  
 355 columns in the tropics (from 30°S to 30°N) with the OC of up to 300 hPa differing by about 10  
 356 DU from the TrC-O<sub>3</sub> ([Figure 7b](#)). The lowest TrC-O<sub>3</sub> trends are located in the northern  
 357 hemisphere (30 – 60°N) at  $0.78 \pm 1.16$  DU/decade, followed by the southern hemisphere (30-60°S  
 358 ( $0.95 \pm 0.75$  DU/decade) and the tropical band (30-30°N ( $1.06 \pm 0.40$  DU/decade). In addition, the  
 359 continental trends over Australia, South Africa, and South America in the 30°S -60°S band are  
 360 essentially negative and the positive trends in this band are contributed mainly by oceanic  
 361 regions (see [Figure 6](#)). The positive trends in the 30°N -60°N band are slightly offset by the  
 362 negative trends over the northeastern US and western Europe (see [Figure 6](#)).

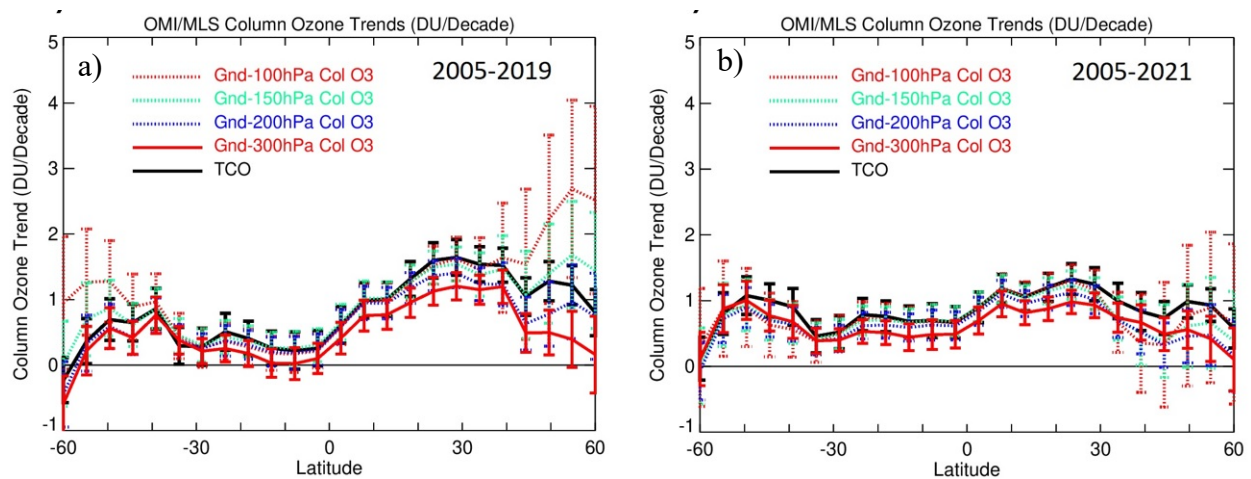


364

365 Figure 7: Time series and zonal mean trends of OMI/MLS TrC-O<sub>3</sub> in different latitudinal bands  
 366 (left) and zonal mean of different column depths (right) from 2005-2019.

367 Observed trends for the time period before COVID-19 (2005-2019) show that OC trends  
 368 were highest in the northern latitudes (0-30° N) reaching about 1.5 DU/decade, followed by the  
 369 northern midlatitudes 30-60°N (Figure 8). The high trends in the 30-60°N band are dominated by  
 370 transpacific impacts as well as some impacts from East Asia. The positive trends in the southern  
 371 hemisphere (0-30° S) are mainly over Amazonia and Southeast Asia, being offset by small  
 372 negative trends over Western Australia and South Africa. The trends during the time period  
 373 (2005-2021) show a decline in O<sub>3</sub> column trends in the northern hemisphere but a slightly  
 374 increasing trend in the southern hemisphere (Figure 8b). The decreasing trends in the northern  
 375 hemisphere during the COVID-19 is consistent with previous literature showing a decrease in  
 376 several pollutants including NO<sub>2</sub> and O<sub>3</sub> due to the extended lockdown periods imposed during  
 377 the pandemic (e.g., Bauwens et al., 2020; Elshorbany et al., 2021; Steinbrecht et al., 2021; Putero  
 378 et al., 2023). The decrease of NO<sub>2</sub> in some parts of Europe and the northeastern USA led to a  
 379 decrease in tropospheric O<sub>3</sub>.

380 Zonal mean trends (Figure 8) show that OC up to 150 hPa is almost identical to that of  
 381 TrC-O<sub>3</sub> except for the high latitudes 45°-60° S and 45°-60° N. The decreasing trends above 30°N  
 382 and 30°S are due to the offsetting impact of negative trends over the northeastern US and western  
 383 Europe in the north, and Australia and South Africa in the south, respectively. This impact is less  
 384 apparent in the 150 hPa OC due to the lower positive trends in that band compared to TrC-O<sub>3</sub>.  
 385 The 200 hPa OC comes next with a very good agreement from 60° S to 10° N. followed by the  
 386 100 hPa which is only in good agreement from 30° S to 30°N, while the 300 hPa OC was the  
 387 farthest from the TrC-O<sub>3</sub>. The decrease of O<sub>3</sub> in the northeastern US and western Europe is  
 388 consistent with decreasing NO<sub>2</sub> trends and NO-sensitive conditions dominating these regions.  
 389 The decreasing trends of NO<sub>2</sub> (see below) are due to the successful measures applied since 2004  
 390 to mitigate air pollution in these regions.



391  
 392 Figure 8: Tropospheric column ozone (TrC-O<sub>3</sub>) and trends for different column depths before the  
 393 COVID-19 pandemic (2005-2019) and including the pandemic (2005-2021).

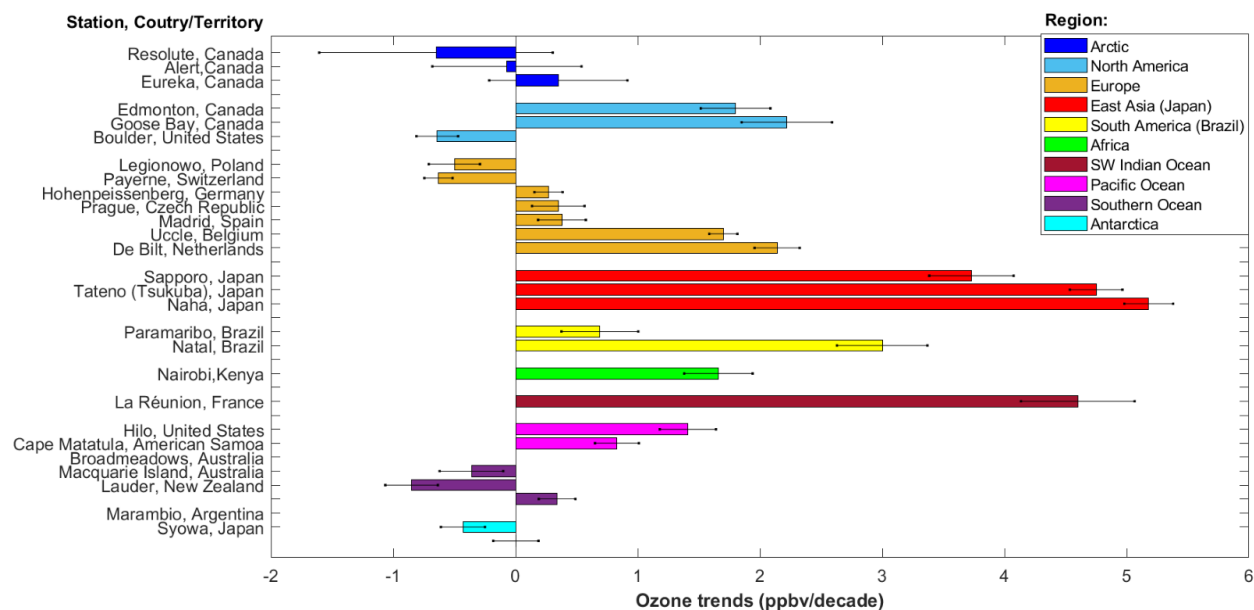
394

### 395 3.4.2. Free tropospheric trends

396 Trends of ozone in the free troposphere presented here are based on previous work published in  
 397 the literature. Despite the high stability of ozonesonde measurements across the global networks

398 over several decades (Stauffer et al., 2022), the spatial sparsity of sounding stations and non-  
399 uniform sampling frequency among sites is a limitation in using these data to produce trends.  
400 These shortcomings have constrained the ability to include data from many stations in previously  
401 published analyses. For example, Chang et. al (2020) estimated that at least 18 profiles per  
402 month are needed at a single station to calculate accurate long-term trends, while uncertainty  
403 increases at lower sampling rates (Chang et al 2024). However, such high sampling frequency is  
404 only achieved at three European stations (Hohenpeissenberg, Germany; Payerne, Switzerland,  
405 and Uccle, Belgium), while the rest of the global stations work at lower sampling rates.  
406 Nonetheless, high-quality ozonesonde observations continue to be the gold standard against  
407 which satellite measurements are validated. Likewise, ozonesonde data continue to provide  
408 spaceborne observations with climatological feedback. Thus, recent studies have softened the  
409 sampling frequency criteria in order to take advantage of the valuable data set collected by the  
410 global ozonesonde networks. For example, the latest trend studies establish the minimum  
411 frequency requirement to calculate trends to at least three profiles per month (Wang et al., 2022;  
412 Christiansen et al., 2022) with at least eight months of sampling in a year, and at least 15 annual  
413 means for an analysis of about two decades (Wang et al., 2022). With these criteria, recent  
414 ozonesonde trend analyses indicate that ozone concentration increased globally by 1.8+/-1.3  
415 ppbv/decade in the free troposphere within 800 to 400 hPa (Christiansen et al., 2022). However,  
416 there is significant regional variability, as illustrated in [Figure 9](#) where ozone trends published by  
417 Wang et. al. (2022) (1995-2017 data between 950-250 hPa) are organized by regions and  
418 stations. For example, ozone in East Asia (Japan) has been increasing at a rate of 3.5 to 5  
419 ppbv/decade, particularly since 2010 (Christiansen et al., 2022). Over the Southwestern Indian  
420 Ocean (La Réunion), trends are of similar magnitude (>4.5 ppbv/decade). In tropical South  
421 America, over the Atlantic basin region (Paramaribo and Natal), sounding measurements also  
422 show ozone increases by almost 3 ppbv/decade (Natal), but other regions in South America  
423 continue to lack sufficient measurements to produce trends. At tropical stations in Africa  
424 (Nairobi) and the Pacific Ocean (Hilo and American Samoa) trends are also positive, although of  
425 lower magnitudes (0.83-1.7 ppbv/decade). In contrast, polar stations both at the Arctic and  
426 Antarctica as well as the Southern Ocean show overall decreasing ozone concentrations to non-  
427 significant trends. Exceptions are the Eureka station in Canada and Lauder station in New  
428 Zealand, which both show slight ozone increases (less than 0.5 ppbv/decade). The direction of  
429 regional trends by Wang et. al. (2022) is consistent with regional trends presented in similar  
430 independent research (Christiansen et al., 2022). As atmospheric composition continues to  
431 become modified under the current regime of climate change, building consistent and longer  
432 time series of ozonesonde measurements at other regions will continue to be an important source  
433 of firsthand information to assess tropospheric ozone changes and trends.

434



435  
 436 Figure 9: Ozone trends in the free troposphere from ozonesonde measurements calculated by  
 437 Wang et. Al. (2022) and organized by region and station. Data covers the 1995-2017 period  
 438 within 950 to 250 hPa. Error bars show 1- $\sigma$  uncertainty. The coordinates of ozonesonde stations  
 439 are listed in Table S1.

440

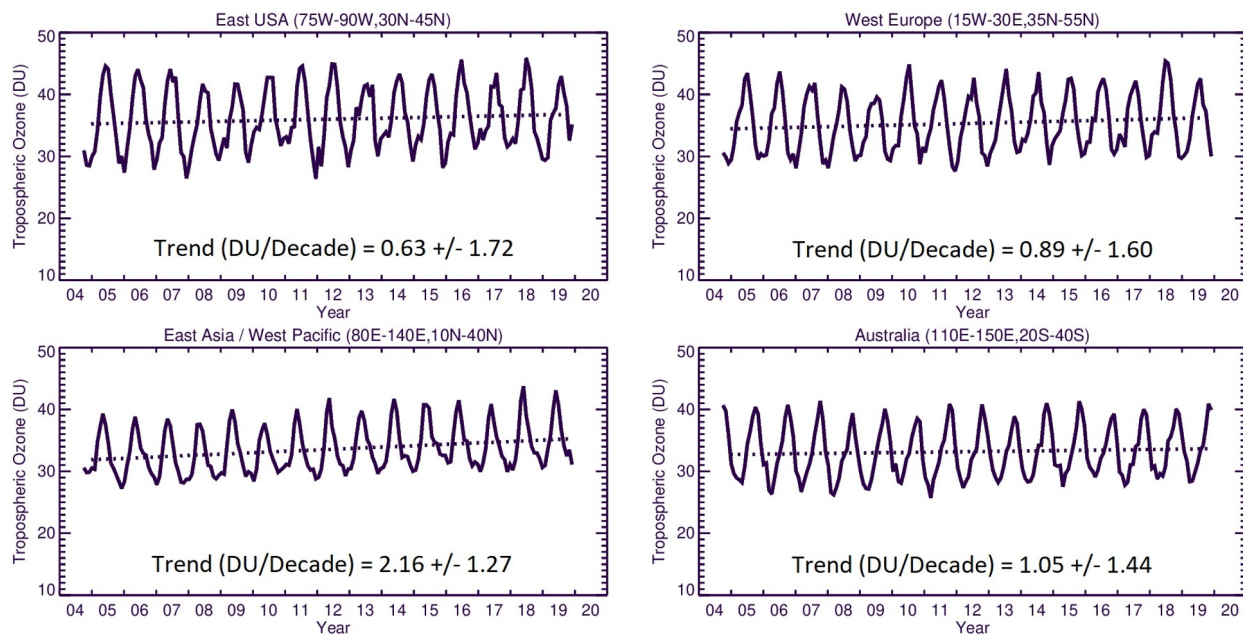
### 441 3.4.3. Regional Ozone Trends

442 As shown in [Figure 10](#), the highest OMI/MLS regional trend is observed over East Asia  
 443 ( $2.16 \pm 1.27$  DU/decade) while the lowest trend is calculated over Eastern USA ( $0.63 \pm 1.72$ )  
 444 followed by Western Europe ( $0.89 \pm 1.60$ ) and Australia ( $1.05 \pm 1.44$ ) DU/decade. We next  
 445 calculate the monthly trends from the GEOS-GMI simulation to investigate how the simulated  
 446 trends vary through the tropospheric column.

447

448





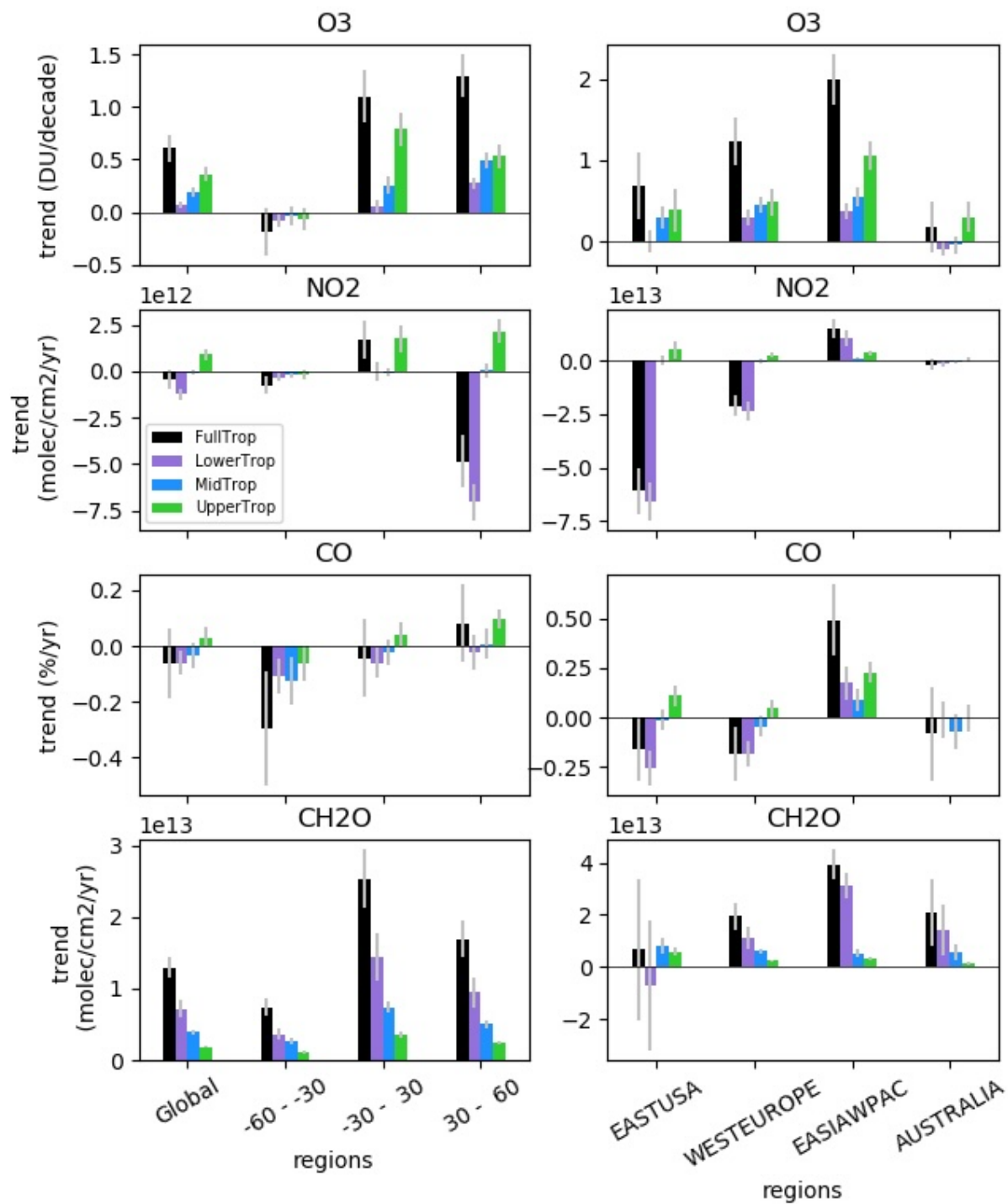
449

450 Figure 10: OMI/MLS observed regional mean trends of TrC-O<sub>3</sub>.

451

452 The simulated trends in partial columns (lower, middle, and upper troposphere), as well as the  
 453 TrC-O<sub>3</sub>, TrC-NO<sub>2</sub>, TrC-HCHO, and TC-CO from 2005 to 2019, are shown in [Figure 11](#). The  
 454 simulated tropospheric columns of TrC-O<sub>3</sub> and TrC-HCHO show a positive trend in most  
 455 regions ([Figure 11](#)), consistent with the results of Liu et al (2022) using a different GEOSCCM  
 456 simulation. Liu et al (2022) highlighted the importance of formaldehyde trends for analyzing the  
 457 simulated trends in tropospheric ozone. Considering different latitude bands, the highest trends  
 458 are simulated between 30° S and 60° N, consistent with calculated trends based on satellite  
 459 observations (see sec. 3.4). In contrast, the simulated NO<sub>2</sub> and CO trends are mostly negative,  
 460 although positive trends are simulated over East Asia. The largest NO<sub>2</sub> negative trends are in the  
 461 northern hemisphere between 30°N and 60°N. The decrease in NO<sub>2</sub> trends is consistent with the  
 462 successful measures to curb emissions of pollution criteria in the US and Europe. The increased  
 463 trends in TrC-O<sub>3</sub> but decreased trends in TrC-NO<sub>2</sub>, and TC-CO might indicate STE contribution  
 464 (Trickl et al., 2020; Li et al., 2024) in addition to the local chemistry.

465



466

467 Figure 11: Global and regional trends in O<sub>3</sub>, NO<sub>2</sub>, CO, and HCHO calculated from the GEOS-  
 468 GMI simulation for the tropospheric column (black), lower troposphere (purple), middle  
 469 troposphere (blue), and upper troposphere (green) from 2005 to 2019. The lower, middle, and  
 470 upper troposphere are defined as in [Figure 5](#).

471

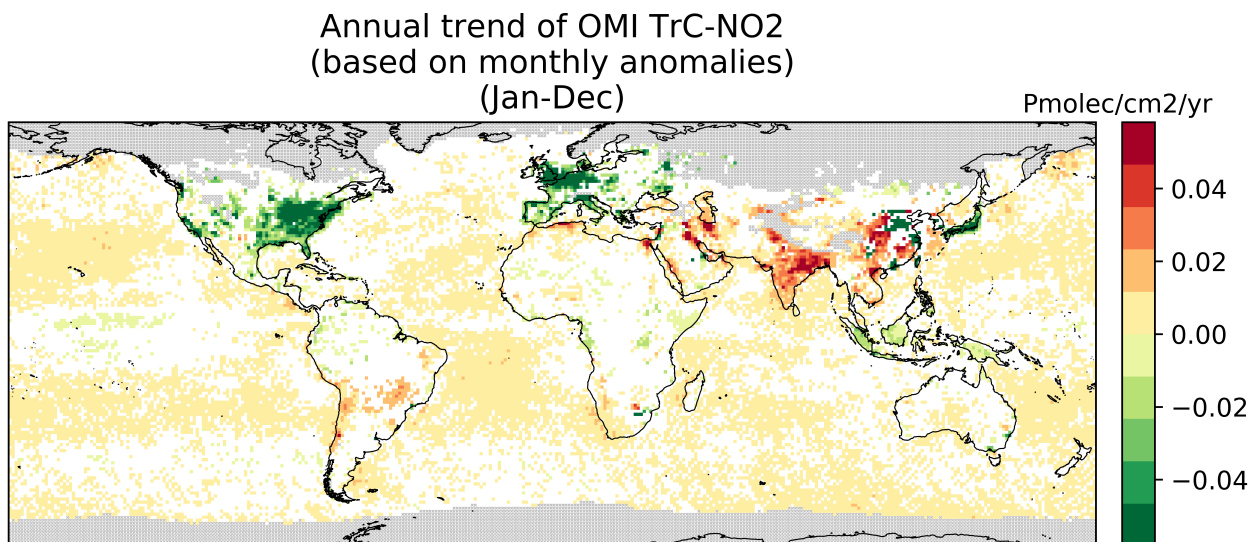
472 The GEOS-GMI simulation provides an estimate of the relative contribution from different  
 473 portions of the tropospheric column to the column trends and shows that this contribution varies  
 474 by region and constituent. The middle and upper troposphere make the largest contributions to

475 the simulated TrC-O<sub>3</sub> trend globally, with large contributions from the upper troposphere driving  
476 the simulated TrC-O<sub>3</sub> trend at 30°S-30°N (Figure 11). The middle and upper troposphere  
477 contribute most of the simulated positive TrC-O<sub>3</sub> trend over the eastern USA, while all three  
478 levels contribute over western Europe and East Asia. The upper troposphere makes the primary  
479 contribution to the simulated trend over Australia. Simulated TrC-O<sub>3</sub> trends are also quite  
480 comparable to those observed by OMI/MLS within the measurement model uncertainty (see  
481 Figure 10 and Figure 7). Over Australia, the OMI/MLS trend of  $1.05 \pm 1.44$  DU/decade is higher  
482 than the model trend of about  $0.18 \pm 0.308$  DU/decade (see Figure 11). However, since OMI/MLS  
483 trend has a calculated uncertainty ( $2\sigma$ ) of 1.44 DU/decade, both the model and OMI/MLS for  
484 Australia are not statistically different.

485 While the upper troposphere is a major driver of the simulated TrC-O<sub>3</sub> trends, the lower  
486 troposphere is the largest contributor to the simulated trends in the tropospheric NO<sub>2</sub>, CO, and  
487 HCHO globally and over many regions (Figure 11). Exceptions include the simulated NO<sub>2</sub> in the  
488 tropics (30°S-30°N), which is dominated by the upper troposphere, the simulated HCHO column  
489 over the eastern USA, which is driven by the middle and upper troposphere; an important role  
490 for upper tropospheric CO over East Asia; and the CO trend over Australia driven by the middle  
491 tropospheric contribution. Figure 11 also shows that in some regions, such as the eastern USA  
492 for all 3 precursors, the upper and lower tropospheric trends counteract each other, reducing the  
493 magnitude of the column trend. In the following sections, we investigate trends and variability in  
494 O<sub>3</sub> precursors, NO<sub>2</sub>, CO, and HCHO.

#### 495 3.4.4. NO<sub>2</sub> Trends

496 The TrC-NO<sub>2</sub> trends over 2005-2019 are shown in Figure 12 with a regional summary in Figure  
497 13. On a global scale, there is a strong spatial variability of the TrC-NO<sub>2</sub> trends. About a third of  
498 the oceans show significantly increasing TrC-NO<sub>2</sub> (at 95% confidence level), especially at mid-  
499 latitude, with trends up to  $+0.01$  Pmolec/cm<sup>2</sup>/yr while only a few cells in the equatorial Pacific  
500 show a significant decrease.  
501



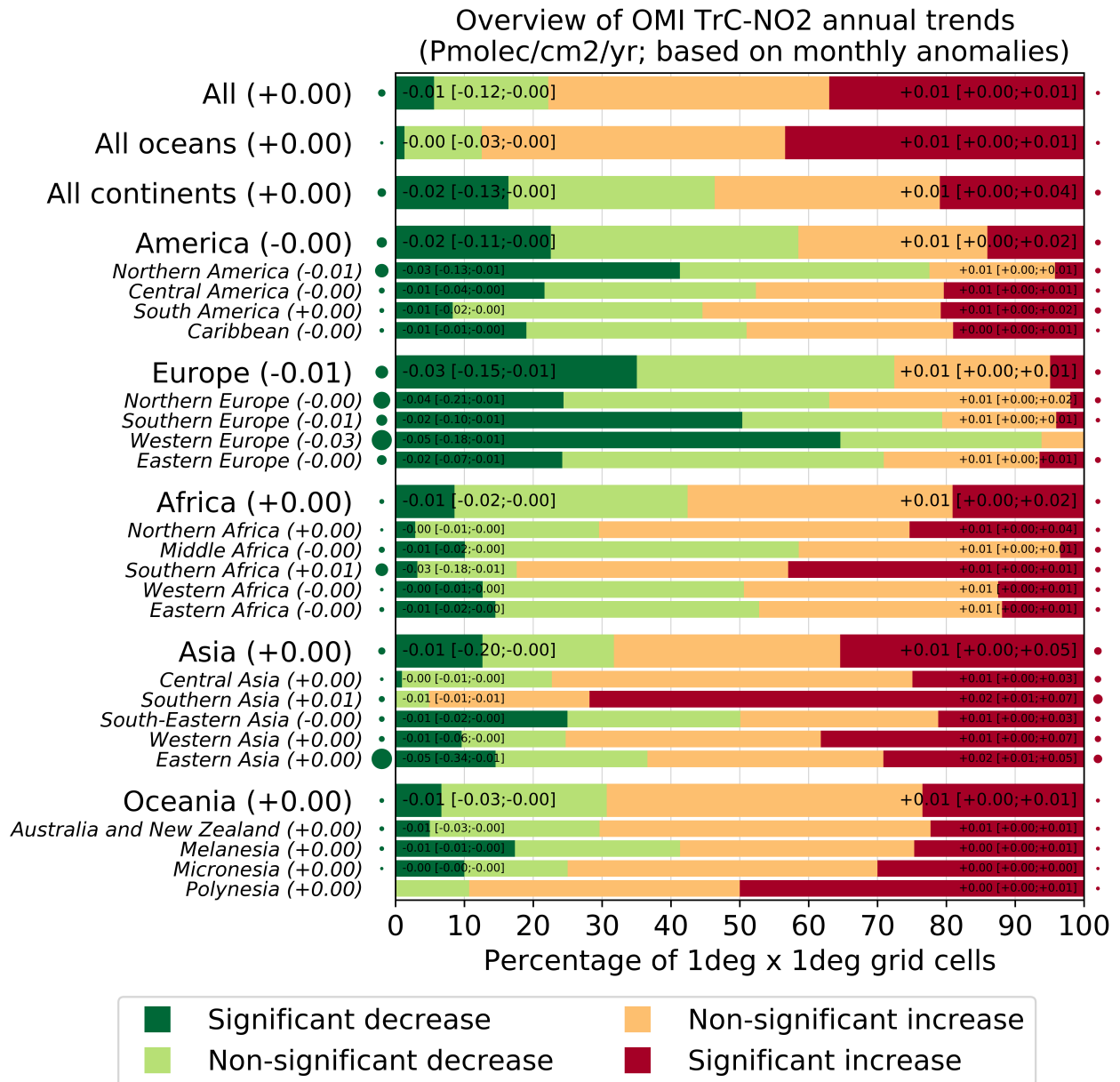
502  
503 Figure 12: Global trends of OMI NO<sub>2</sub> tropospheric column (TrC-NO<sub>2</sub>) over 2005-2019 (see text  
504 for details on the calculation of the trends). Grey areas correspond to areas without enough data,  
505 white areas correspond to regions where the trends remain statistically insignificant at a 95%  
506 confidence level.

507 Regional trends are shown in [Figure 13](#). For significant trends in a given region, the  
508 numbers correspond to the percentiles 5/50/95 of trends among the different cells of the region  
509 where trends are significant. Each region is tagged with a circle whose size is proportional to the  
510 p50 of the significant trends (red for positive and green for negative), which allows us to quickly  
511 see regions where the trend is strong. For instance, for Eastern Asia (this region includes 1442  
512  $1^\circ \times 1^\circ$  grid cells) about 15% of the grid cells (about 216 grid cells) in this region show a  
513 significant decrease in TrC-NO<sub>2</sub>. Over these specific 216 cells with a significant decrease of  
514 TrC-NO<sub>2</sub>, the 5th and 95th percentile of the trend is -0.34 and -0.01, respectively,  
515 Pmolec/cm<sup>2</sup>/yr. About 28% of the grid cells in this region show a significant increase of TrC-  
516 NO<sub>2</sub> (which means about 403 grid cells). Over these specific 403 cells with a significant increase  
517 of TrC-NO<sub>2</sub>, the 5th (resp 95th) percentile of the trend is +0.01 (resp 0.05) Pmolec/cm<sup>2</sup>/yr.  
518 Therefore, the Eastern Asia region shows sub-regions with significantly decreasing TrC-NO<sub>2</sub>,  
519 others with significantly increasing TrC-NO<sub>2</sub>, and the rest with non-significant (positive and  
520 negative) trends. This figure allows us to quickly understand the distribution of the trends within  
521 a given region while the overall regional trend is given by the 50<sup>th</sup> percentile and the circles  
522 tagging each region. It's a regional summary of what is shown in the trend global map. In Eastern  
523 Asia, the area where trends are significantly positive is more extended than for the significant  
524 decrease (28% versus 15%), but the trend values tend to be smaller (at least when comparing the  
525 50<sup>th</sup> percentiles, -0.05 versus +0.01 Pmolec/cm<sup>2</sup>/yr). The map of regions is included in the  
526 supplement. Canada is included in northern America but as shown in the trend map, most of  
527 Canada does not have OMI data

528 Over continental areas, significant positive and negative trends are found in about 15-  
529 20% of the grid cells each ([Figure 12](#)). Regions with predominantly decreasing TrC-NO<sub>2</sub> include  
530 western and southern Europe (where about 50-60% of cells with a significant decrease), northern  
531 America (40% of cells with a significant decrease, mostly located in the eastern United States),  
532 Japan, and Indonesia. In absolute terms, these negative trends reach values of about -0.03  
533 Pmolec/cm<sup>2</sup>/yr. Specific eastern regions of China also show similar significant TrC-NO<sub>2</sub>  
534 decreases but overall, a larger part of the country faces increasing trends up to +0.03  
535 Pmolec/cm<sup>2</sup>/yr. Similar positive trends are observed over most of India, as well as in specific  
536 parts of south-eastern Asia (mainly Vietnam) and the Middle East (mainly Iran and Iraq).  
537 Conversely, TrC-NO<sub>2</sub> trends in Africa and South America remain mainly insignificant, except in  
538 a few specific regions with significant increases (e.g. South Africa, Morocco, Chile, and parts of  
539 Brazil).

540 The trends in NO<sub>2</sub> have varying effects on the tropospheric ozone column, which is  
541 related to the different local chemistry in each region. The concomitant decrease in TrC-O<sub>3</sub> and  
542 TrC-NO<sub>2</sub> trends over some parts of the eastern US, and western Europe is consistent with the  
543 strict NO<sub>x</sub> control measures that were applied over the last two decades. STE can also contribute  
544 to increased TrC-O<sub>3</sub> trends, especially in the mid-latitudes. A decreasing trend of TrC-NO<sub>2</sub> but  
545 an increasing trend of TrC-O<sub>3</sub> is present in some other regions such as in the central US, which  
546 might be due to local chemistry and STE.

547



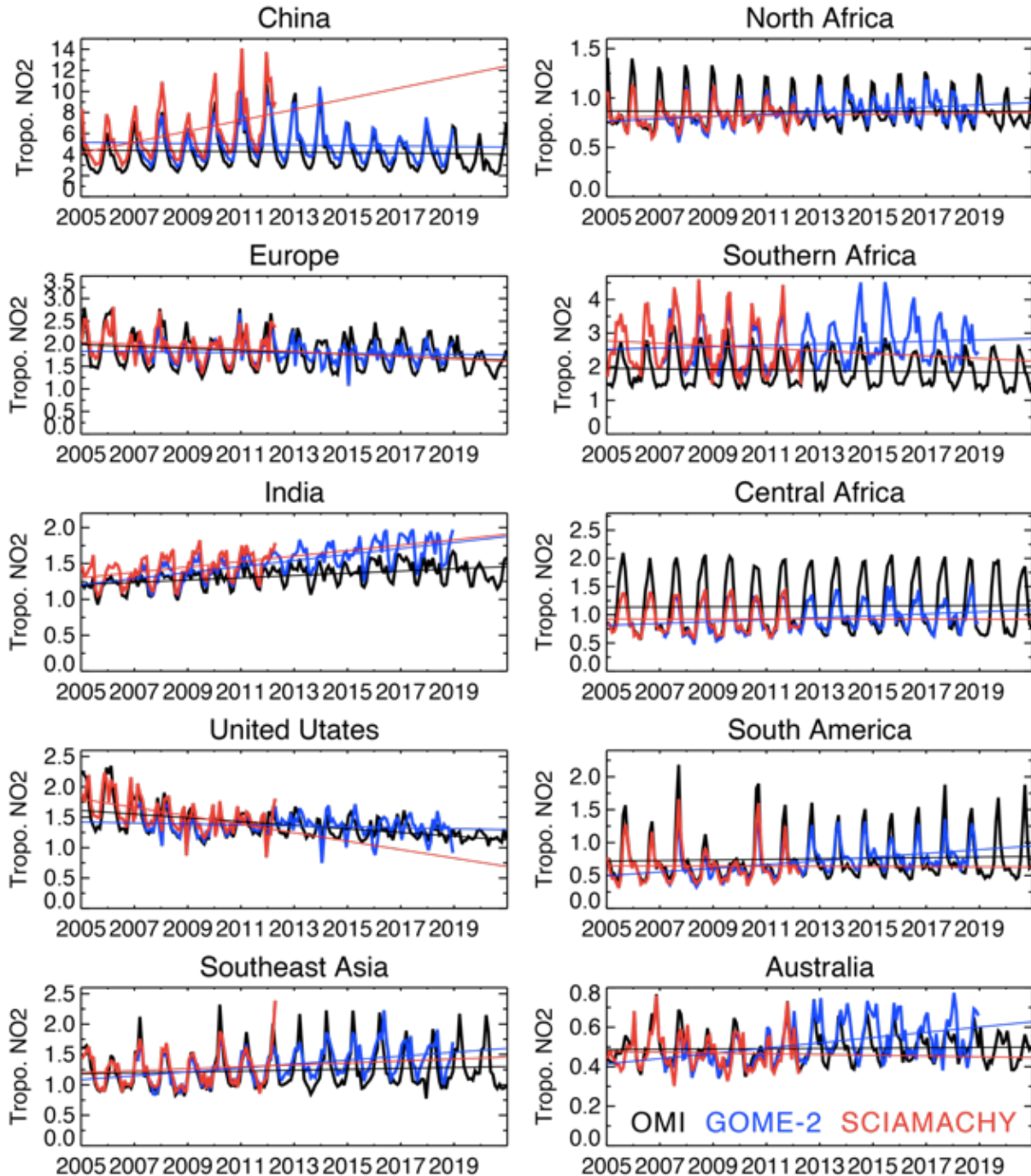
549

550 Figure 13: Summary of the statistically significant and insignificant regional trends of OMI NO<sub>2</sub>  
 551 tropospheric column (TrC-NO<sub>2</sub>) trends over 2005-2019, at a 95% confidence level (see text for  
 552 details on the calculation of the trends). For each region, the trend on the bars is in the format:  
 553 p50 [p5; p95], which represents the 50<sup>th</sup>[5<sup>th</sup>, and 95<sup>th</sup>] percentiles of the trends.

554

555 [Figure 14](#) shows the time series of regional mean tropospheric NO<sub>2</sub> concentrations from three  
 556 satellite instruments, OMI for 2005-2020, GOME-2 for 2007-2018, and SCIAMACHY for 2005-  
 557 2012. All the instruments exhibit common large seasonal and year-to-year variations over both  
 558 industrial regions and biomass-burning areas. Slight systematic differences among the instruments  
 559 can mainly be attributed to the different overpass times. The satellite observations show positive  
 560 trends over China by 2010, followed by a continued decrease. Over the USA and Europe, all the  
 561 retrievals show a downward trend over the analysis period. Over the US, the observed TrC-NO<sub>2</sub>

562 levels decreased rapidly during 2005–2009 and subsequently show weaker reductions, as  
 563 discussed by Jiang et al. (2018). A similar slowdown trend is found in Europe. Over India, the  
 564 OMI observations show positive trends over the 14 years ( $+1.6\% \text{ yr}^{-1}$ ). The seasonal and year-to-  
 565 year variations over Southeast Asia and northern and central Africa are associated with changes in  
 566 biomass-burning activity (Ghude et al., 2009).  
 567



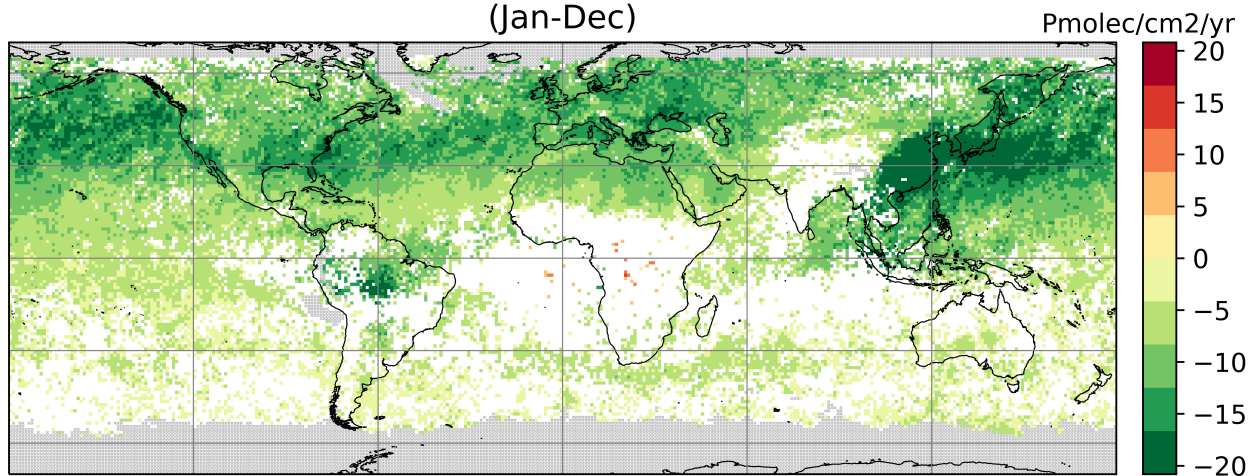
568  
 569 Figure 14: Time series of regional monthly mean tropospheric NO<sub>2</sub> columns (in 10<sup>15</sup> molecules  
 570 cm<sup>-2</sup>) averaged over China (110–123° E, 30–40° N), Europe (10° W–30° E, 35–60° N), the US  
 571 (70–125° W, 28–50° N), India (68–89° E, 8–33° N), South America (50–70° W, 20° S–Equator),

572 northern Africa (20° W–40° E, Equator–20° N), central Africa (10–40° E, Equator–20° S),  
573 southern Africa (25–34° E, 22–31° S), southeastern Asia (96–105° E, 10–20° N), and Australia  
574 (113–155° E, 11–44° S) obtained from OMI (black), GOME-2 (blue), and SCIAMACHY (red).

### 575 3.4.5. CO Trends

576 CO trends are calculated based on MOPITT v9 products, see sec. 2.2.1. Observed CO trends  
577 below show a slowing in the trend compared to a previous analysis (Buchholz et al. (2021)). In  
578 the northern hemisphere, CO trends are largely negative over the US and Europe, which is  
579 consistent with improvements in combustion efficiency and policies implemented to reduce air  
580 pollution since 2004. Except for small sporadic positive trends, no significant trends can be  
581 calculated over Central Asia (India and China), while there is a strong negative trend in East  
582 China due to the recent strong focus on air quality improvement, and no significant trend in the  
583 SH.

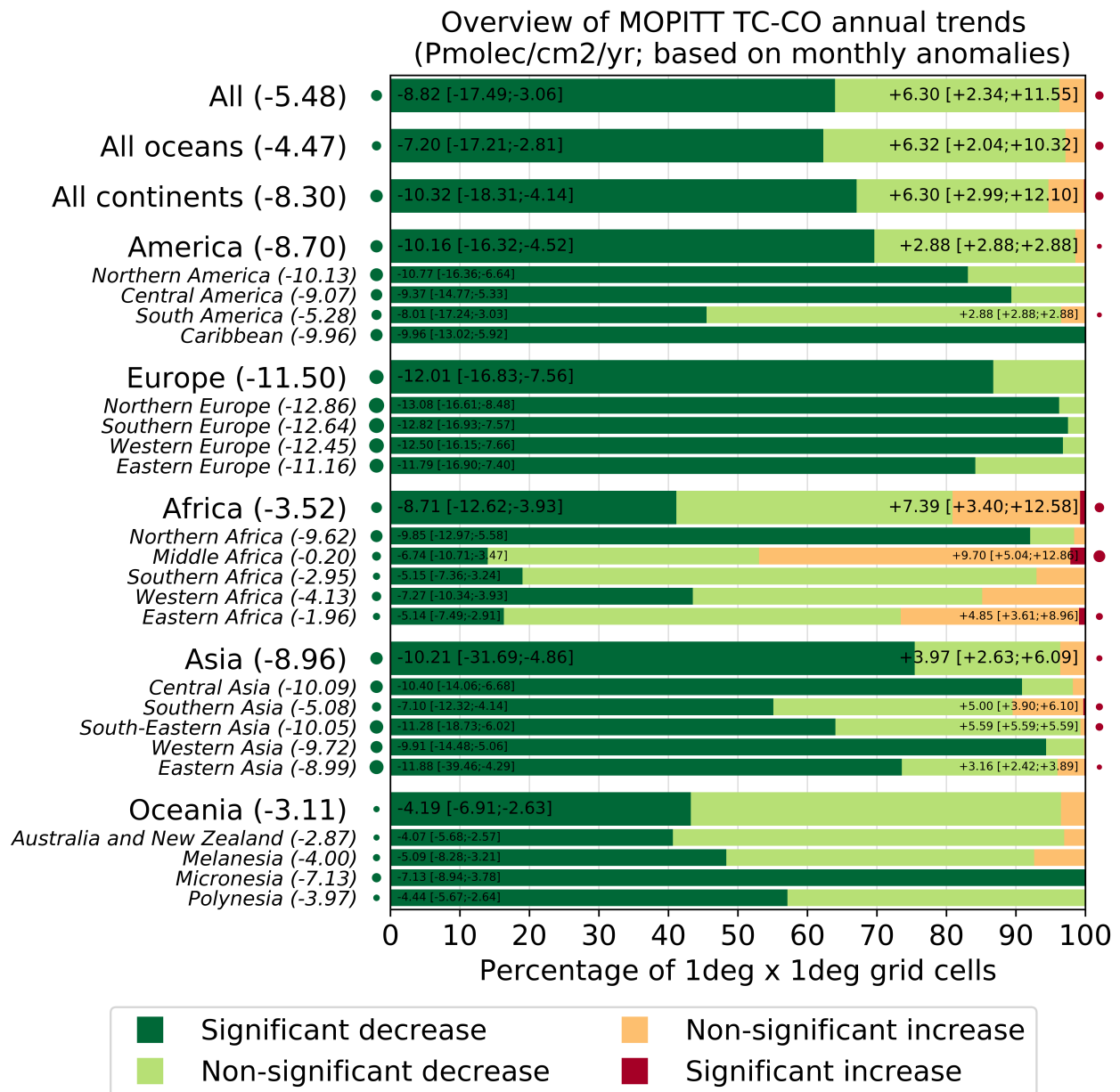
Annual trend of MOPITT TC-CO  
(based on monthly anomalies)  
(Jan-Dec)



584  
585 Figure 15: Trends in TC-CO from MOPITT V9J data, 2005-2019 (see text for details on the  
586 calculation of the trends). Grey areas correspond to areas without enough data, white areas  
587 correspond to regions where the trends remain statistically insignificant at a 95% confidence  
588 level.

589  
590 A regional summary of the trends in the global map is shown in [Figure 16](#). CO trends are  
591 predominantly negative everywhere except for some sporadic positive trends over middle Africa.  
592 Decreasing TC-CO trends are highest in Europe, followed by Asia and America with about 86%,  
593 75%, and 69% of their cells being negative, respectively. The 50 percentiles of the trends in  
594 these cells are -12.01, -10.21, and -10.16 Pmolec/cm<sup>2</sup>/yr, respectively. Africa shows the lowest  
595 decreasing trends as the negative trends in North Africa are being offset by small increasing  
596 trends in middle Africa. Overall, about 41% of the cells in Africa show decreasing trends, and  
597 50% of the trends in these cells account for -8.71 Pmolec/cm<sup>2</sup>/yr. Thus, even though the NH  
598 accounts for most of CO emissions, decreasing trends of TC-CO are evident in these regions.

599



600

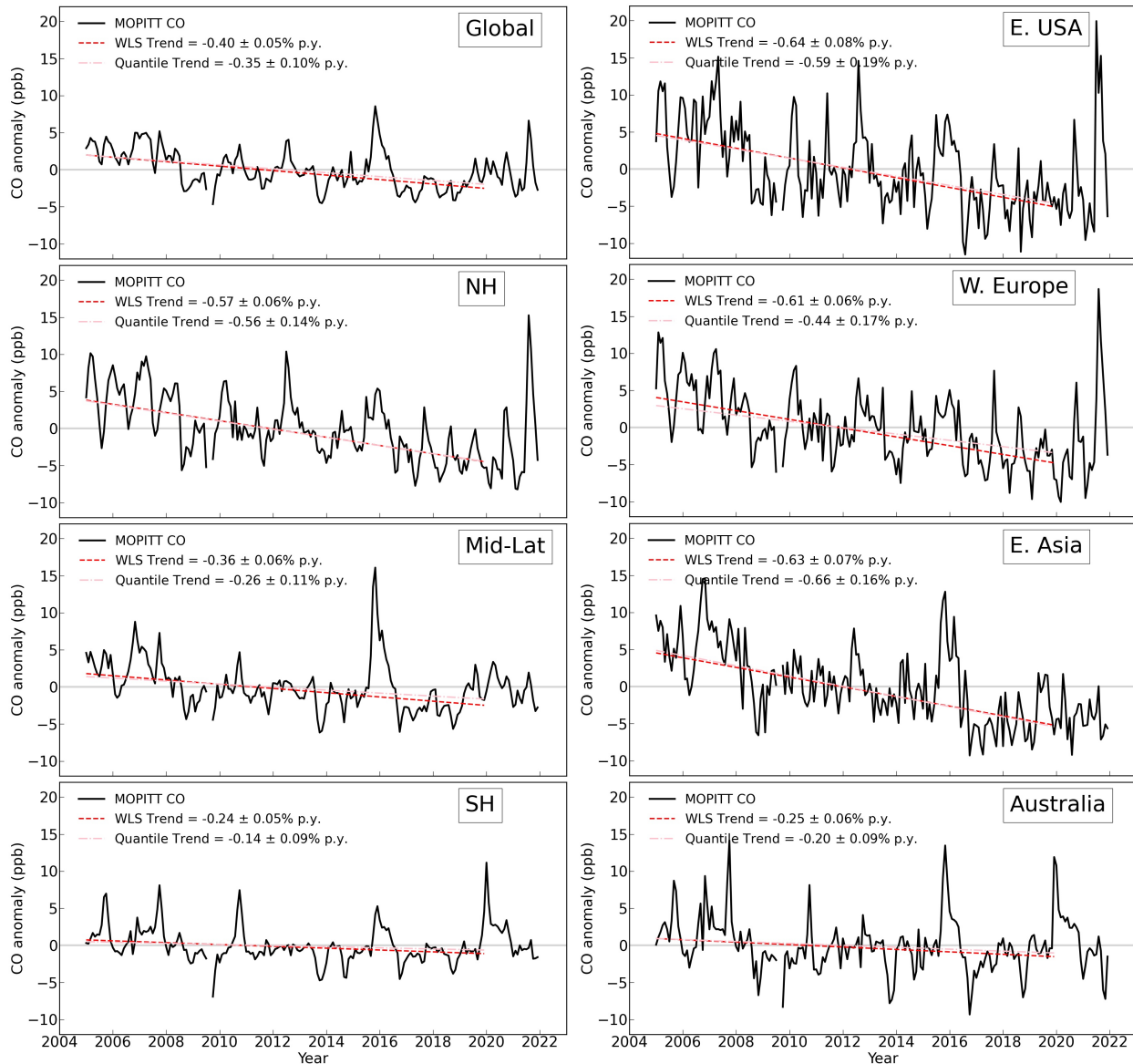
601 Figure 16: Summary of the statistically significant and insignificant regional trends of MOPITT  
 602 TC-CO trends over 2005-2019, at a 95% confidence level (see text for details on the calculation  
 603 of the trends). For each region, the trends reported on the left (resp. right) represent the 5<sup>th</sup>, 5<sup>0th</sup>  
 604 and 9<sup>5th</sup> percentiles of the trends calculated over the different grid cells showing a significant  
 605 TC-CO increase or decrease.

606

607 Shown below are also the trends in the MOPITT column average volume mixing ratio (VMR)  
 608 anomalies from 2005 to 2019 (Figure 17) using QR as well as Weighted least squares (WLS)) as  
 609 Buchholz et al. (2021). The region boundaries are the same as used in Fig. 10 and 11. Results  
 610 show a significant decreasing trend in the NH (-0.35 ± 0.1% annually), a smaller decreasing trend  
 611 in the Mid-latitudes (-0.26 ± 0.1% annually) and no significant trend in the SH (-0.14 ± 0.1%  
 612 annually). The three anthropogenic regions investigated in the NH all show strong decreases in  
 613 CO. The larger negative trend over Australia (-0.2 ± 0.1% annually) than the average SH,



614 suggests sources from the other two land regions (Southern Africa and South America) may be  
 615 counteracting negative trends in CO for the SH.  
 616



617  
 618 Figure 17: MOPITT monthly average CO anomalies in column average volume mixing ratio  
 619 (VMR, ppb), 2005-2021 (black). Updated dataset based on Buchholz et al. (2021). Data is Level  
 620 3, monthly average daytime observations, using version 9 joint NIR/TIR retrievals (V9J).  
 621 Regions are defined in [Figure 10](#) and [Figure 11](#). Trends are calculated on anomalies 2005-2019.  
 622 The weighted Least Squares trend (red) is weighted by the monthly regional standard deviation.  
 623 The quantile regression trend is also shown (pink). Grey dashed lines indicate a zero trend.

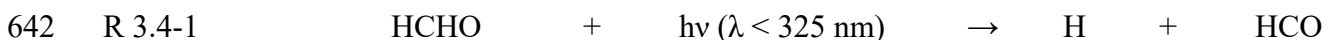
624  
 625 We also compare CO trends with Community Earth System Model (CESM) simulations  
 626 (Supplement Fig S1). While the magnitude of modeled CO tends to be underestimated relative to  
 627 observations, the anomalies between the model and measurements are comparable, indicating the  
 628 model reproduces interannual variability well. The negative trends in the NH are also reproduced

629 by CESM, although to a smaller degree than observations, suggesting that the trends in sources  
 630 or loss processes (such as OH oxidation) are underestimated in the model. These processes will  
 631 impact the feedback into modeled ozone and the resulting interpretation of driving factors for  
 632 ozone abundance and variability. Interestingly, CESM correctly represents a negative trend in  
 633 CO for the NH and East Asia while GEOS-GMI has a positive CO trend in those regions (Fig.  
 634 11), likely due to the well-known misrepresentation of East Asia air quality improvements in  
 635 emission inventories (Yin et al, 2015; Strode et al., 2016; Zheng et al, 2019). In the SH, CESM  
 636 does not predict significant trends.

637

### 638 **3.4.6. HCHO Trends**

639 HCHO, mainly a photochemical product results from hydrocarbon oxidation. HCHO is itself a  
 640 source of OH and ozone through its photolysis producing HO<sub>2</sub>, which can be recycled back to  
 641 OH if sufficient NO levels are present.



646 Unlike higher aldehydes, the OH reaction with HCHO leads also to the formation of a formyl  
 647 radical (HCO), which ultimately forms HO<sub>2</sub> ([R 3.4-3](#)).

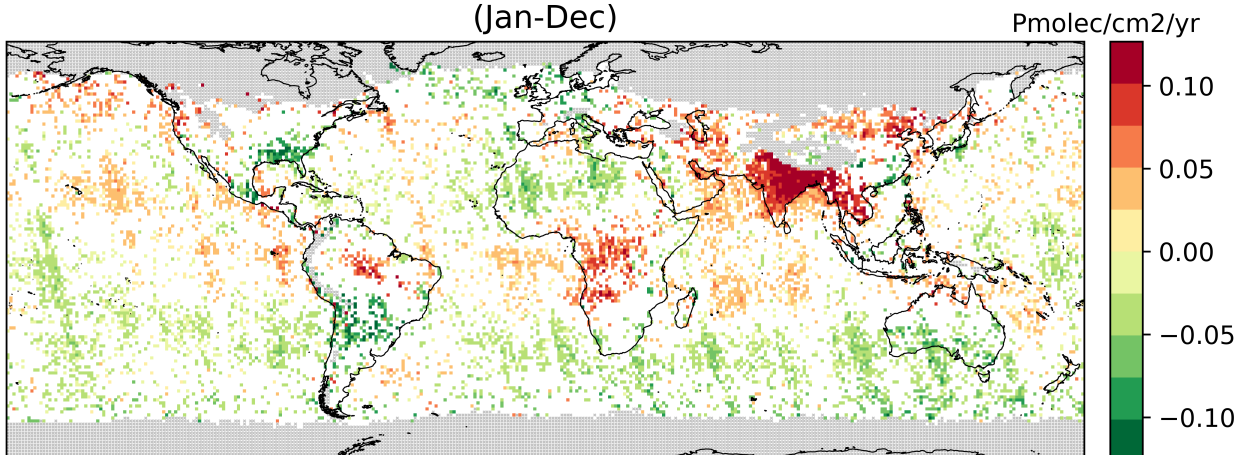


649 Due to its solubility, the variability of HCHO also depends on the presence of clouds, and wet  
 650 deposition ultimately represents another important sink for HCHO (Lelieveld and Crutzen, 1991).  
 651 Overall, HCHO plays a key role in the O<sub>3</sub> budget, both in polluted and remote regions.

652 Trends of the OMI HCHO tropospheric columns (hereafter referred to as TrC-HCHO) are  
 653 computed as described for OMI TrC-NO<sub>2</sub>. TrC-HCHO trends over 2005-2019 are shown in  
 654 [Figure 18](#) with a regional summary in [Figure 19](#). The first global feature to highlight on the  
 655 global trends map is the presence of stripes along the OMI orbits. The number of rows affected  
 656 by the OMI row anomaly has increased over the years (Boersma et al., 2018). The affected rows  
 657 are filtered out in the HCHO data, but the change in the sampling and the related increase in the  
 658 noise impact the trend analysis. Along orbit stripes in the trend analysis should be ignored but  
 659 zonal trends are still valid ([Figure 18](#)).

660

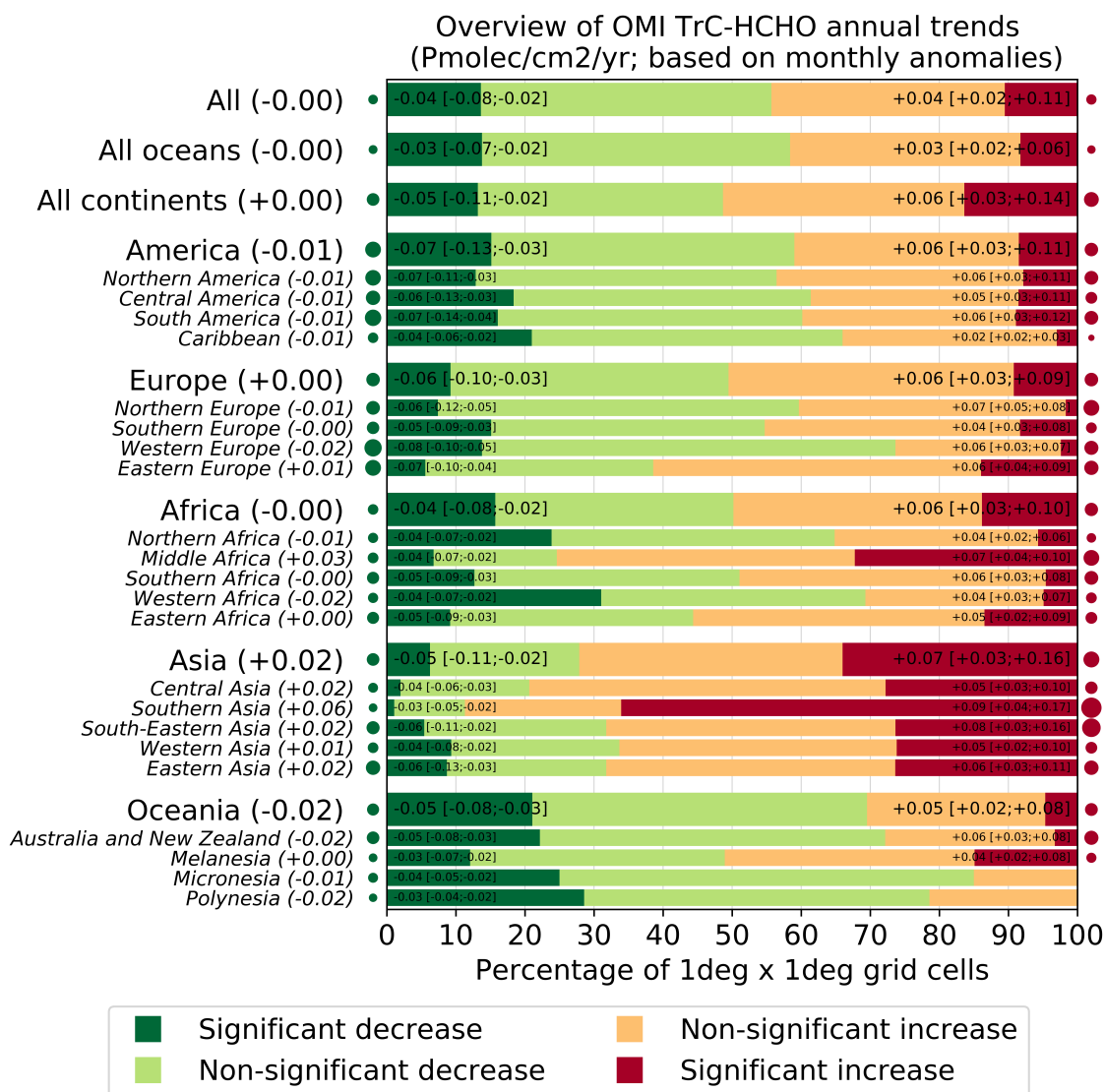
Annual trend of OMI TrC-HCHO  
(based on monthly anomalies)  
(Jan-Dec)



661  
662 Figure 18: Global trends of OMI HCHO tropospheric column (TrC-HCHO) over 2005-2019 (see  
663 text for details on the calculation of the trends). Grey areas correspond to areas without enough  
664 data, white areas correspond to regions where the trends remain statistically insignificant at a  
665 95% confidence level.

666 Despite the fact that TrC-HCHO trends remain insignificant over a large part of the globe,  
667 specific regions do highlight clear trends. The region with clearest changes is unambiguously  
668 southern Asia where about 65% of the cells show increasing trends with a median of +0.09  
669 Pmolec/cm<sup>2</sup>/yr. The other regions with a large portion (25-30% of the cells) of increasing trends  
670 include the rest of Asia and central Africa, with median TrC-HCHO trends ranging between  
671 +0.05 and +0.08 Pmolec/cm<sup>2</sup>/yr, as well as some parts of central Brazil (Amazonians).  
672 Conversely, some significant decreases of TrC-HCHO are observed in the south-eastern US, the  
673 southern half of Southern America, North and western Africa, and southern Australia, although  
674 part of them overlap with the aforementioned stripes and might thus not be real.

675



676

677 Figure 19: Summary of the statistically significant and insignificant regional trends of OMI  
 678 HCHO tropospheric column (TrC-HCHO) trends over 2005-2019, at a 95% confidence level  
 679 (see text for details on the calculation of the trends). For each region, the trends reported on the  
 680 left (resp. right) represent the 5<sup>th</sup>, 50<sup>th</sup> and 95<sup>th</sup> percentiles of the trends calculated over the  
 681 different grid cells showing a significant TrC-HCHO increase or decrease.

682

683 HCHO trends are inconsistent with that of O<sub>3</sub> (sec. 3.4.1) in some regions which might be due to  
 684 several factors, such as their different sensitivity to NO<sub>x</sub> and hydrocarbons (Luecken et al., 2018)  
 685 but also possible STE contribution to tropospheric ozone levels, especially in midlatitudes  
 686 (Willimas et al., 2019; Li et al., 2024). For example, while TrC-O<sub>3</sub> is increasing in the  
 687 southeastern US, TrC-NO<sub>2</sub>, TC-CO, and TrC-HCHO are decreasing, which, in addition to the  
 688 local chemistry, might indicate a STE signal. TrC-NO<sub>2</sub> trends are decreasing over the northern  
 689 coast of Australia while those of TrC-O<sub>3</sub> and TrC-HCHO are increasing. While the increase of  
 690 HCHO/NO<sub>2</sub> might indicate a trend toward NO-limited conditions (see below), the increase of  
 691 TrC-O<sub>3</sub> trends in this region might also indicate increasing trends of STE contribution (Li et al.,  
 692 2024). Similarly, while NO<sub>2</sub> trends are slightly increasing over central and southern Australia,

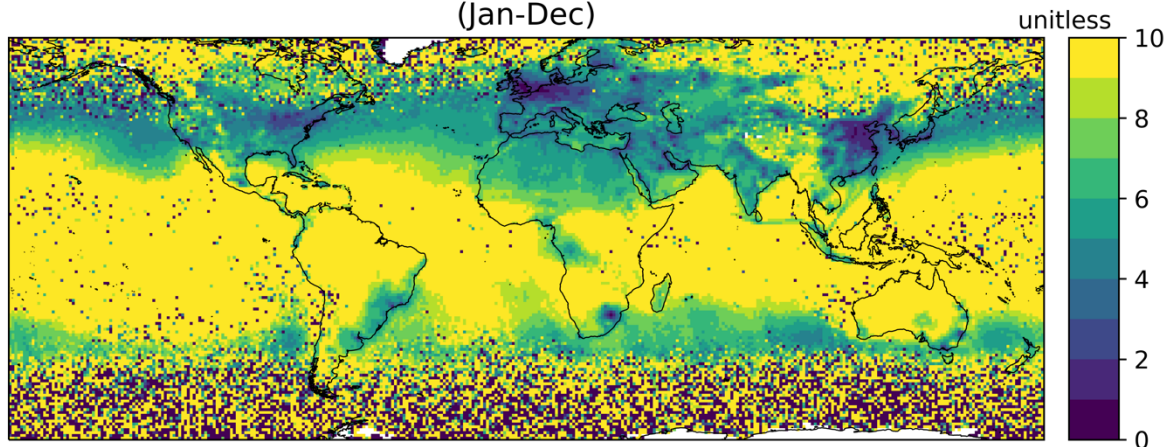
693 trends of TrC-O<sub>3</sub> and TrC-HCHO are decreasing, which indicates a trend toward VOC-limited  
694 conditions (see below).

695

### 696 3.4.7. HCHO/NO<sub>2</sub>

697 The ratio of TrC-HCHO/TrC-NO<sub>2</sub> observed from space (e.g., Martin et al., 2004) has been used  
698 in a number of studies to give insights on the O<sub>3</sub> chemical regime, higher (resp. lower) TrC-  
699 HCHO/TrC-NO<sub>2</sub> ratios indicate NO<sub>x</sub>-limited (resp. RO<sub>x</sub>-limited) regimes. Although imperfect  
700 (e.g. Sourì et al., 2023), this indicator yet provides some qualitative information on the evolution  
701 of the O<sub>3</sub> regime over the last years (Nussbaumer et al., 2023). We note that this analysis does not  
702 consider variations in the ratios and their trends with respect to season or altitude. The mean TrC-  
703 HCHO/TrC-NO<sub>2</sub> over 2005-2019 are shown in Figure 20, and the trend results are in Figure 21  
704 with a regional summary in Figure 22. The highest ratios are observed in the tropical regions due  
705 to strong TrC-HCHO from biogenic sources and fire NMVOC emissions in tropical South America  
706 and Africa combined with relatively low TrC-NO<sub>2</sub>. Conversely, lower TrC-HCHO/TrC-NO<sub>2</sub> ratios  
707 are observed across western Europe and north-eastern Asia, and to a lesser extent, the northeastern  
708 US.  
709

Mean OMI TC-HCHO/TC-NO<sub>2</sub>  
(Jan-Dec)



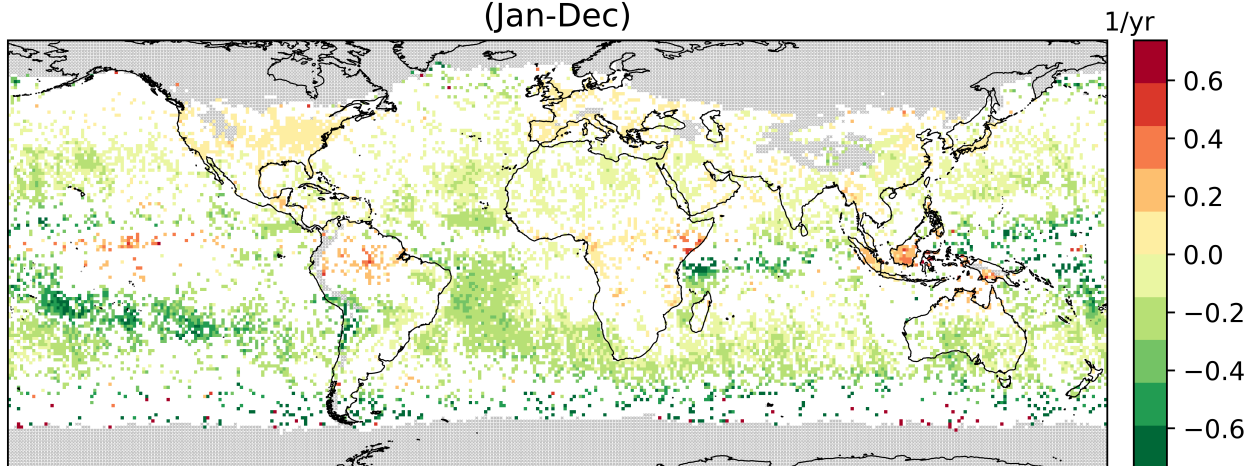
710

711 Figure 20: Global mean OMI HCHO/NO<sub>2</sub> tropospheric column ratio over 2005-2019.

712

713 At a global scale, the significant changes in TrC-HCHO/TrC-NO<sub>2</sub> trends (Figure 21-Figure 22)  
714 mostly go in the direction of a reduction, with about 25% of the grid cells showing a median trend  
715 of -0.52 yr<sup>-1</sup>. (while only 5% of the cells show a significant increase of +0.03 yr<sup>-1</sup>) as shown in  
716 Figure 22. This suggests that these areas are evolving toward VOC-sensitive conditions (which  
717 does not necessarily imply that they are already in this regime). This situation is observed over a  
718 large part of Oceania (especially Polynesia) and specific parts of Africa, Asia, and South America.  
719 The opposite significant trends, toward more NO-sensitive conditions, are mainly observed over  
720 Europe and northern America, as well as south Asia. We note that the mean TrC-HCHO/TrC-NO<sub>2</sub>  
721 indicates the mean status of the chemical regime over this period of time (2005-2019). However,  
722 the trends of the TrC-HCHO/TrC-NO<sub>2</sub> ratio show the changing sensitivity of the chemical regime  
723 over this period of time. For example, while the ratio in Eastern US indicates VOC-sensitive  
724 conditions, the trends of TrC-HCHO/TrC-NO<sub>2</sub> indicate a direction toward NO-sensitive  
725 conditions.

Annual trend of OMI TrC-HCHO/NO<sub>2</sub>  
(based on monthly anomalies)  
(Jan-Dec)



727

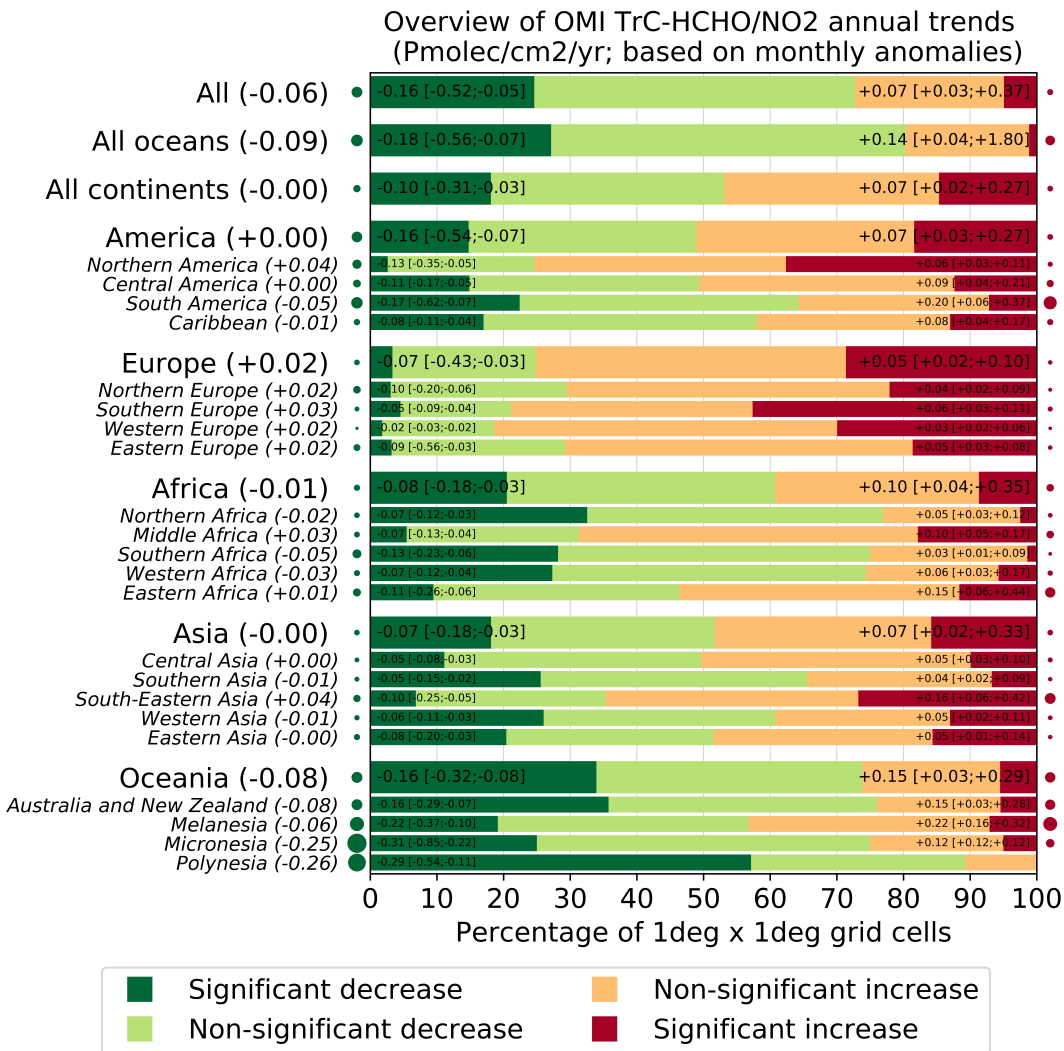
728 Figure 21: Global trends of OMI HCHO/NO<sub>2</sub> tropospheric column ratio over 2005-2019 (see  
729 text for details on the calculation of the trends). Grey areas correspond to areas without enough  
730 data, white areas correspond to regions where the trends remain statistically insignificant at a  
731 95% confidence level.

732

733 The trends on the TrC-HCHO/TrC-NO<sub>2</sub> ratio is mainly driven by specific trends on TrC-HCHO  
734 and/or TrC-NO<sub>2</sub>, depending on the region. The ratio increase in southern and western Europe and  
735 southeast Asia appears primarily due to decreasing TrC-NO<sub>2</sub>, since TrC-HCHO does not change  
736 significantly. Over North America, observed TrC-HCHO values decrease but less than TrC-NO<sub>2</sub>,  
737 which thus drives the ratio toward an increase. Conversely, the increase of TrC-HCHO/TrC-NO<sub>2</sub>  
738 in equatorial Africa and Amazonians appears mainly driven by increasing TrC-HCHO. The  
739 regions where TrC-HCHO/TrC-NO<sub>2</sub> is significantly decreasing include Chile and Australia, due  
740 to both decreasing TrC-HCHO and increasing TrC-NO<sub>2</sub> (Figure 22), indicating a trend towards a  
741 VOC-limited regime. Note that over the US, Jin et al. (2020) demonstrated the reasonable ability  
742 of the OMI-based TrC-HCHO/TrC-NO<sub>2</sub> trends to capture the transition from RO<sub>x</sub>-limited to NO<sub>x</sub>-  
743 limited regimes over main US cities and found a relatively good consistency between observed  
744 changes of the surface O<sub>3</sub> and space-based HCHO/NO<sub>2</sub> increasing trends.

745

746



747  
748  
749  
750  
751  
752  
753  
754

Figure 22: Summary of the statistically significant and insignificant regional trends of OMI TrC-HCHO/TrC-NO<sub>2</sub> tropospheric column ratio trends over 2005-2019, at a 95% confidence level (see text for details on the calculation of the trends). For each region, the trends reported on the left (resp. right) represent the 5<sup>th</sup>, 50<sup>th</sup> and 95<sup>th</sup> percentiles of the trends calculated over the different grid cells showing a significant TrC-HCHO/TrC-NO<sub>2</sub> increase or decrease.

### 756 **3.5. Lightning NO<sub>x</sub> and Its Effects on Tropospheric NO<sub>x</sub> and O<sub>3</sub>**

757 Nitric oxide (NO) is produced in lightning flash channels and quickly comes into equilibrium with  
758 NO<sub>2</sub>. Cloud-scale simulations of thunderstorms indicate that 55-75% of lightning NO<sub>x</sub> (LNO<sub>x</sub>) is  
759 detrained above 8 km (Pickering et al., 1998) where it enhances upper tropospheric NO<sub>y</sub>, OH, and  
760 O<sub>3</sub> (Labrador et al., 2005; Allen et al., 2010; Liaskos et al., 2015) and contributes to enhanced  
761 longwave radiative absorption by O<sub>3</sub> (Lacis et al., 1990; Finney et al., 2018). Enhanced OH leads  
762 to a decrease in CH<sub>4</sub> lifetime and decreased longwave radiative absorption (Fiore et al., 2006;  
763 Finney et al., 2018). The lifetime of NO<sub>x</sub> in the upper troposphere is controlled by the chemical  
764 cycling of NO<sub>x</sub> with reservoir species and is 10-20 days away from deep convection (Prather and  
765 Jacob, 1997) but only 2-12 hours in the vicinity of convection (Nault et al., 2016, 2017). This  
766 chemical recycling provides a source of NO<sub>x</sub> downwind of thunderstorms, which causes the ozone  
767 production efficiency of emitted NO<sub>x</sub> to be 4-20 times higher in the upper troposphere than at the  
768 surface. Thus, LNO<sub>x</sub> has a disproportionate impact on the tropospheric O<sub>3</sub> budget (Pickering et al.,  
769 1990; Grewe et al., 2001; Sauvage et al., 2007).

770 The distribution of lightning is fairly well known over much of the Earth due to remote  
771 sensing observations and an increase in the number and capability of ground-based lightning  
772 networks. However, the LNO<sub>x</sub> production efficiency (PE, mol fl<sup>-1</sup>) is a continued source of  
773 uncertainty. Schumann and Huntrieser (2007) reviewed the literature on LNO<sub>x</sub> production, finding  
774 a best estimate of 250 moles per flash, with uncertainty factors ranging from 0.13 to 2.7. The PE  
775 can be estimated from theoretical and laboratory considerations (Price et al., 1997; Koshak et al.,  
776 2014), using thunderstorm anvil observations by aircraft (Ridley et al., 2004; Huntrieser et al.,  
777 2008, 2011; Pollack et al., 2016; Nault et al., 2017; Allen et al., 2021a), based on satellite data  
778 (Bucsela et al., 2010; Beirle et al., 2010; Pickering et al., 2016; Bucsela et al., 2019; Lapierre et  
779 al., 2020; Zhang et al., 2020; Allen et al., 2019, 2021b), or using cloud-resolved (e.g., DeCaria et  
780 al., 2000; 2005; Fehr et al., 2004; Ott et al., 2007, 2010; Cummings et al., 2013; Pickering et al.,  
781 2023) or global model simulations with chemistry (e.g. Martin, et al., 2007; Murray et al., 2012;  
782 Miyazaki et al., 2014; Marais et al., 2018). These various techniques have yielded PE estimates  
783 ranging from <50 to >1000 mol fl<sup>-1</sup>, with most estimates in the 100-400 mol fl<sup>-1</sup> range. Miyazaki  
784 et al. (2014) assimilated OMI NO<sub>2</sub>, MLS and TES O<sub>3</sub>, and MOPITT CO into a chemical transport  
785 model to provide comprehensive constraints on the global LNO<sub>x</sub> source, resulting in an estimate  
786 of mean PE of 310 moles per flash. Marais et al. (2018) used cloud-sliced upper tropospheric NO<sub>2</sub>  
787 from OMI together with the GEOS-Chem model to estimate a mean LNO<sub>x</sub> PE of 280 moles per  
788 flash. Lightning is the dominant source of NO<sub>x</sub> in the tropical upper troposphere year-round and  
789 in the northern mid-latitudes in summer. Lightning is responsible for 10-15% of NO<sub>x</sub> emissions  
790 globally. Assuming 100-400 mol fl<sup>-1</sup>, the global LNO<sub>x</sub> production is likely 2 – 8 Tg N a<sup>-1</sup>  
791 (Schumann and Huntrieser, 2007; Verma et al., 2021). LNO<sub>x</sub> impacts air quality and deposition  
792 (Kaynak et al., 2008; Allen et al., 2012). On average LNO<sub>x</sub> adds 1-2 ppbv to surface O<sub>3</sub> (Kang et  
793 al., 2019b), although contributions as large as 18 ppbv have been seen for individual events  
794 (Murray et al., 2016). Allen et al. found that the addition of LNO<sub>x</sub> to the Community Multiscale  
795 Air Quality (CMAQ) model increased wet deposition of oxidized nitrogen at National  
796 Atmospheric Deposition Program (NADP) sites by 43%, reducing low biases from 33% to near-  
797 zero. Kang et al. (2019b) found similar improvements for wet deposition and also found that  
798 including LNO<sub>x</sub> resulted in smaller biases with respect to ozonesondes and aircraft profiles taken  
799 during the NASA DISCOVER-AQ field campaign (Flynn et al., 2016). Thus, to accurately assess  
800 its impacts on air quality, it is critical that LNO<sub>x</sub>-producing deep convection is accurately  
801 simulated.



802 Only in recent years with the advent of satellite observations of lightning flashes and improved  
803 coverage by ground-based lightning networks has there been sufficient data to make estimates of  
804 trends in the occurrence of lightning. However, it is unknown whether trends in LNO<sub>x</sub> production  
805 are similar to those of lightning itself. Lightning characteristics such as the ratio of intracloud (IC)  
806 flashes to cloud-to-ground (CG) flashes, the multiplicity (i.e., the number of strokes per flash), and  
807 the peak current or energy associated with flashes may vary over time. All of these lightning  
808 characteristics may have effects on the magnitude of LNO<sub>x</sub> production. We have insufficient data  
809 to take into account these possible effects on LNO<sub>x</sub> production over large spatial domains or over  
810 sufficiently long periods of time.

### 811 **3.5.1. Global Historical Trends of Lightning**

812 The first attempts at an examination of trends in thunderstorm activity were conducted in terms of  
813 thunder-days (in Japan by Kitagawa et al., 1989; in Brazil by Pinto et al., 2013). A more recent  
814 global analysis was conducted by Lavigne et al. (2019), who analyzed trends in thunder-days  
815 (number of days with audible thunder at weather observation stations) over 43 years and in flashes  
816 recorded by the Lightning Imaging Sensor (LIS) on the Tropical Rainfall Measuring Mission  
817 (TRMM) for 16 years. Thunder-days increased since the 1970s in the Amazon Basin, the Maritime  
818 Continent, India, Congo, Central America, and Argentina. Decreases in thunder-days were found  
819 in China, Australia, and the Sahel region of Africa. Lavigne et al. (2019) do not provide a global  
820 trend in thunder days, but an average trend computed over the nine primary lightning regions that  
821 they considered, weighted by the mean annual thunder days in each region, yields a near global  
822 estimate of +3.8% per decade. How well do thunder-days represent lightning flash rate? Lavigne  
823 et al. found a positive correlation between thunder-days and LIS flash rates in China, the Maritime  
824 Continent, South Africa and Argentina, but disagreement on the trend in India and West Africa.

825 Large-scale ( $\pm 38^\circ$  latitude) trends in lightning flashes have been examined in the data collected by  
826 the LIS on the TRMM satellite (January 1998 – December 2014) and on the International Space  
827 Station (February 2017 – December 2021). Füllekrug et al. (2022; see Figure SB2.1b) demonstrate  
828 that the annual mean deviations from the 1998 – 2021 mean are no more than ~5% except for ~-  
829 10% in 2020 and ~-8% in 2021. However, no long-term trend is evident from the LIS data. The  
830 possibility that these larger negative deviations in 2020 and 2021 are due to Covid-19 lockdowns  
831 and general declines in economic activity has been speculated. The link may be provided by  
832 changes in Aerosol Optical Depth (AOD) as suggested by Liu et al. (2021) who demonstrated 10-  
833 20% flash reductions in March – May 2020 relative to the 2018 – 2021 mean for those months  
834 from the GLD360 and WWLLN ground-based lightning networks. Regional lightning reductions  
835 were consistent with AOD reductions noted by Sanap (2021). Larger reductions in lightning were  
836 noted over Africa/Europe and Asia/Maritime Continent and lesser reductions over the Americas.

### 837 **3.5.2. Regional Historical Trends of Lightning**

838 Widely varying trends in lightning over China have been reported in the literature. To some extent,  
839 whether the trend in lightning is upward or downward depends on the particular region studied and  
840 on the period of time considered. Yang and Li (2014) were the first to report on lightning trends  
841 in China. They used lightning data from the TRMM/LIS sensor and human-observed thunderstorm  
842 day occurrence over the period 1990 to 2012 in southeastern China. Thunderstorms and lightning  
843 occurrence increased over the period as well as LIS precipitation radar echo tops heights. These  
844 increases were accompanied by decreases in visibility, indicating increases in pollution aerosol.  
845 Detailed work on lightning trends in China has been performed in relation to aerosols. Shi et al.  
846 (2020) correlated flashes from the TRMM/LIS Low-Resolution Monthly Time Series (2.5 deg.  
847 resolution) with AOD from MODIS-Terra V6.1 Level 3 over the period 2001 to 2014. For AOD

848 < 1.0,  $r = 0.64$ , indicating a likely microphysical effect on lightning flash rate. For  $AOD > 1.0$ ,  $r =$   
849  $-0.06$ , which could indicate that with higher aerosol concentration there is a radiation effect  
850 stabilizing the atmosphere and/or a decrease in the number of graupel particles in the mixed-phase  
851 region of the storms that is important for charging. Flashes were also correlated with surface  
852 relative humidity and Convective Available Potential Energy (CAPE). As AOD generally  
853 increased over much of the early portion of this time period and then decreased, lightning flash  
854 rates followed similar trends. Wang et al. (2021) examined a 9-year record (2010- 2018) of CG  
855 lightning from the China Lightning Detection Network in three polluted urban areas of China  
856 (Chengdu, Wuhan, and Jinan). They found decreasing trends (see Wang et al., 2021) in CG  
857 lightning and total AOD (from the MERRA-2 reanalysis). Annual mean lightning density in these  
858 three regions decreased by 50 – 75% as annual mean AOD fell from 0.70 – 0.75 to 0.53 to 0.62.

859 Qie et al. (2022) analyzed the OTD/LIS record from 1996 through 2013, and found that lightning  
860 increased over the eastern Tibetan Plateau by  $0.072 \pm .069$  fl  $\text{km}^2 \text{yr}^{-1}$ . Over the 18 years, this  
861 increase amounted to a total of  $1.3$  fl  $\text{km}^2 \text{yr}^{-1}$ , compared with a climatological value of  $7.7$  fl  $\text{km}^2$   
862  $\text{yr}^{-1}$ , thereby indicating a significant increase. The ground-based World Wide Lightning Location  
863 Network (WWLLN) also showed an increase in strokes in this region. The increase in lightning  
864 frequency in this region was found to be due to an increase in thunderstorm frequency, and not  
865 due to increased storm intensity.

866 Koshak et al. (2015) analyzed National Lightning Detection Network (NLDN) CG flashes over  
867 the contiguous United States (CONUS) from 2003 to 2012. The five-year mean flashes over 2008  
868 to 2012 decreased by 12.8% from the five-year mean for 2003 to 2007 (Table 1). The CONUS  
869 average wet bulb temperature also trended downward during this period, which may have led to  
870 lesser or weaker storms. However, US Environmental Protection Agency air quality trends show  
871 an 18% decrease in PM<sub>2.5</sub> concentrations over CONUS between the two subperiods, which also  
872 could have had an influence on the flash rates. A recent effort to update the Koshak et al. (2015)  
873 analysis is underway. NLDN flashes have been reprocessed (Kenneth Cummins, personal  
874 communication) from 2015 through 2021 to ensure that the classification of IC and CG flashes is  
875 done consistently with data prior to 2015. Trend analysis of NLDN CG flashes from 2003 (a major  
876 upgrade of the NLDN network hardware) through 2022 (William Koshak, personal  
877 communication) shows a significant reduction in CG flashes over CONUS, comparing the mean  
878 CG flashes over 2003-2004 with the mean over 2021 -2022. Within this period a major decrease  
879 (~25%) in CONUS CG flashes occurred from 2011 to 2012. Flashes in 2013 remained low, but  
880 recovered by 2014-2015. A major decrease (~27%) occurred from 2019 to 2020, with a small  
881 increase in 2021. These results have been obtained from ongoing efforts by Dr. William Koshak  
882 of the NASA Marshall Space Flight Center, and are presently part of a draft manuscript by lead  
883 author Koshak that extends and refines the earlier work in Koshak et al. (2015). Details concerning  
884 these trends will be contained in that manuscript.

885 A possible contributing factor to the CONUS decline in CG flashes over 2003 to 2021 is the  
886 substantial decrease in aerosol. Surface annual average PM<sub>2.5</sub> concentrations averaged over  
887 CONUS decreased by 37% from 2000 to 2021 according to the EPA National Air Quality Trends  
888 Report (<https://www.epa.gov/air-trends/air-quality-national-summary>). However, no decrease in  
889 CONUS annual average PM<sub>2.5</sub> was seen from 2019 to 2020. As mentioned previously, AOD may  
890 be a better indicator of the aerosol amount that may become incorporated into thunderstorm clouds.  
891 Sanap (2021) showed negative anomalies of AOD of ~0.1 in portions of CONUS in March and  
892 April 2020 and 0.1 to 0.2 in May 2020. The major decrease in CONUS CG flashes from 2011 to  
893 2012 has been related to drought conditions during Summer 2012 over the South Central and  
894 Southeastern US (Koshak et al., 2015). The reason for the number of CONUS flashes remaining

895 lower in 2013 is uncertain. Koehler (2020) analyzed 26 years (1993 – 2018) of NLDN CG  
896 lightning data to construct a thunder-day climatology for CONUS. Positive anomalies from the  
897 26-year mean were found from Texas to Colorado during 2003 to 2007, and negative anomalies  
898 in this region during 2008 to 2012. These anomalies were consistent with precipitation anomalies  
899 associated with ENSO.

900

901 Holzworth et al. (2021) analyzed primarily CG lightning data from WWLLN for June, July, and  
902 August for the years 2010 through 2020. The ratio of lightning strokes north of 65° N latitude to  
903 the total global strokes increased by a factor of three over this period. This increase occurred as  
904 the surface temperature anomaly in this region increased by 0.3°C (see Holzworth et al., 2021).  
905 These results suggest a substantial increase in upper tropospheric NO<sub>x</sub> and subsequent ozone  
906 production at high northern latitudes.

907

### 908 **3.5.3. Future Lightning Trends**

909 Parameterizations in global chemistry and climate models have been developed for  
910 lightning flash rate. These schemes typically use kinematic, thermodynamic or microphysical  
911 variables from the model as predictors. In some studies such predictors have simply been applied  
912 to output from multiple climate models. This is the case with the Romps et al. (2014) work, which  
913 showed that when a lightning parameterization scheme using CAPE x Precipitation Rate is applied  
914 to 11 climate models an increase in CG lightning by 12 +/- 5% per degree Celsius of climate  
915 warming was computed. This work simply used the 12-hour resolution time series of spatial means  
916 of these variables over CONUS as input. Changes in IC lightning flashes were not considered. IC  
917 flashes typically outnumber CG flashes by a factor of 3 averaged over CONUS. Therefore, the  
918 result of this work is unknown with respect to the amount of change in LNO<sub>x</sub> emission. Romps et  
919 al. (2018) updated their analysis using CAPE from 3-hourly North American Regional Reanalysis  
920 (NARR) data and hourly precipitation from NOAA River Forecast Centers, finding that CAPE x  
921 Precipitation Rate captures the spatial, seasonal, and diurnal variations of NLDN CG flash rate  
922 over land, but does not predict the pronounced land-ocean contrast in flash rates. Therefore, these  
923 analyses are of limited value in estimating trends of LNO<sub>x</sub> over broader-scale regions. Romps et  
924 al (2019) tested four lightning proxies in a cloud-resolved 4-km resolution simulation over  
925 CONUS with the Weather Research and Forecasting (WRF) model, and over the tropical oceans  
926 with a Radiative Convective Equilibrium model. The proxies were CAPE x Precipitation Rate,  
927 precipitation with vertical velocity > 10 m/s, vertical ice flux at the 260K isotherm, and vertical  
928 integral of cloud ice and graupel product. The fractional change in proxy values per 1 degree  
929 Celsius of warming over CONUS was +8 to +16%. Over the tropical oceans the changes in proxy  
930 values per degree ranged from +12% for CAPE x Precipitation Rate to -1% for ice flux and -3%  
931 for the cloud ice and graupel product. Therefore, over broad regions of the Earth, there is great  
932 uncertainty on future trends in lightning.

933 Finney et al. (2016; 2018) compared lightning projections for 2100 using vertical ice flux  
934 (Finney et al., 2014) and cloud-top height parameterizations for flash rate in the UK Chemistry  
935 and Aerosols Model. They obtained -15% global change in total flash rate with ice flux under a  
936 strong global warming scenario (see Finney et al., 2018), which was composed of a greater  
937 decrease in the tropics and small increases in mid-latitudes. In terms of LNO<sub>x</sub> emissions this work  
938 using the ice flux scheme produced -0.15 TgN K<sup>-1</sup> change over the years from 2000 to 2100,  
939 implying less O<sub>3</sub> production. With the cloud-top height scheme they obtained +0.44 TgN K<sup>-1</sup> LNO<sub>x</sub>  
940 change, implying increased O<sub>3</sub> production. However, the ice flux scheme provided a more realistic

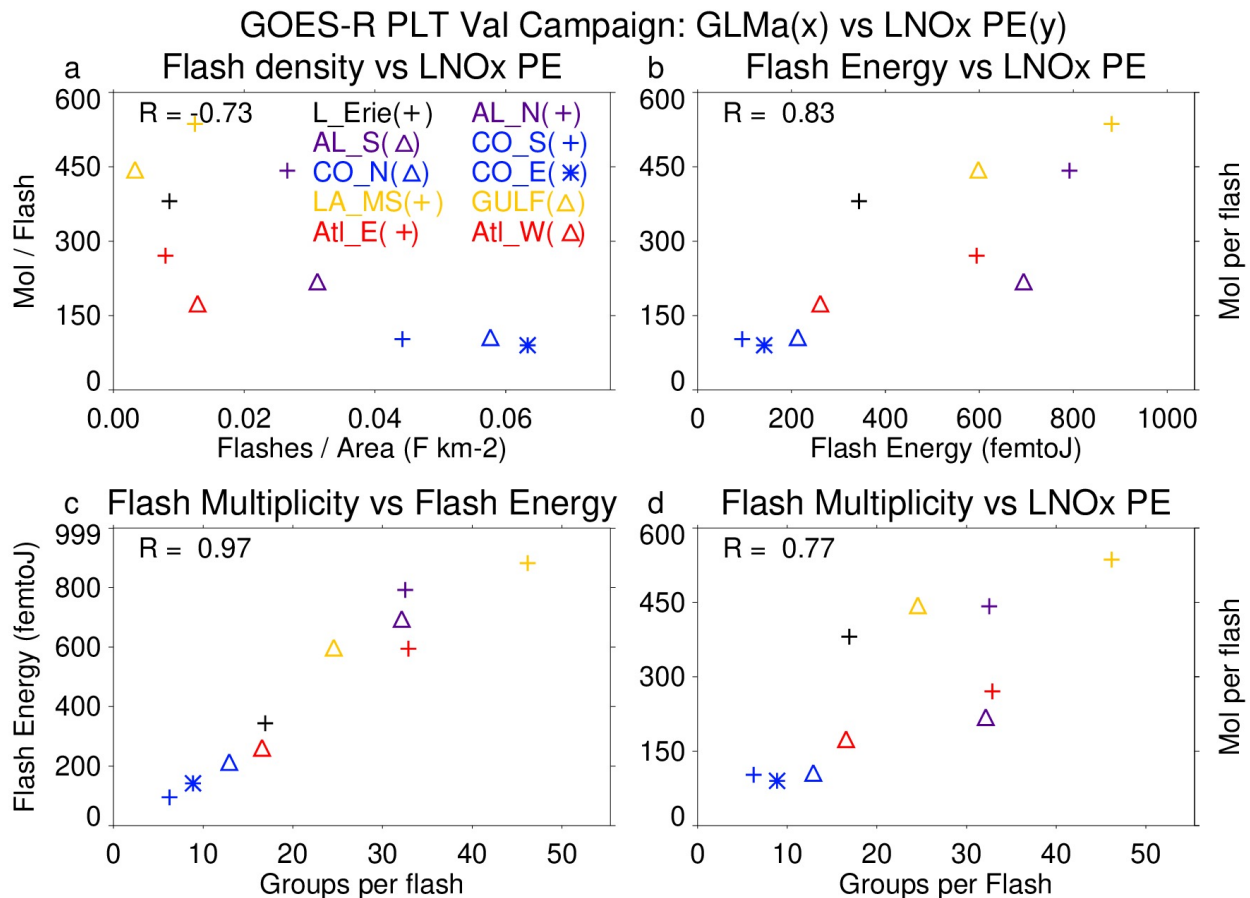
941 representation of global lightning for present day. Therefore, the negative LNO<sub>x</sub> emissions change  
 942 from this scheme may be more realistic. If indeed the ice flux scheme better represents the current  
 943 distribution of lightning, both the Romps and Finney results suggest no significant increase in  
 944 LNO<sub>x</sub> emission in future climate, and possibly a small global decrease. Murray (2018) points out  
 945 that the ice flux scheme is a closer representation of the underlying charging mechanism, but this  
 946 scheme needs to be tested in multiple global chemistry and climate models.

947

### 948 3.5.4. Recent findings concerning LNO<sub>x</sub> PE

949 Recent satellite-based estimates of LNO<sub>x</sub> production (Figure 23) have suggested a possible flash  
 950 rate dependence of LNO<sub>x</sub> production per flash (Bucsela et al., 2019; Allen et al., 2019; 2021).  
 951 Smaller values of LNO<sub>x</sub> PE in these studies were found to be associated with high flash rates,  
 952 likely due to smaller flashes in these conditions (Bruning and Thomas, 2015). Allen et al. (2021a)  
 953 noted positive correlations (Figure 23) of LNO<sub>x</sub> PE with flash energy and with flash multiplicity  
 954 (number of strokes per flash). Laboratory studies by Wang et al. (1998) found a positive correlation  
 955 between peak current and LNO<sub>x</sub> production. Koshak et al. (2015) found an 8% increase in peak  
 956 current from the 2003-2007 period to the 2008-2012 period that accompanied the 12.8% decrease  
 957 in CG flashes. These findings make it difficult to project future LNO<sub>x</sub> production given only a  
 958 prediction of future lightning flashes.

959



960

961 Figure 23. Scatterplots showing the GLMa-derived relationship between (a) LNO<sub>x</sub> PE (mol per  
 962 flash) and flash density (flashes km<sup>-2</sup>), (b) LNO<sub>x</sub> PE and flash energy (fJ), (c) flash energy and

963 flash multiplicity, and (d) LNO<sub>x</sub> PE and flash multiplicity. Colors are used to separate flight days  
964 while symbols are used to separate system within each flight day. Correlations are shown in the  
965 upper right. LNO<sub>x</sub> PE derived from airborne remote sensor, the Geo-CAPE Airborne Simulator  
966 (GCAS) during the GOES-R Post-launch Test field campaign. GLMa indicates Geostationary  
967 Lightning Mapper data adjusted for missing data. From Allen et al. (2021a).

968

### 969 **3.5.5. Impacts of LNO<sub>x</sub> on upper tropospheric O<sub>3</sub>**

970 The literature concerning the effects of lightning NO<sub>x</sub> production on upper tropospheric ozone  
971 focuses on photochemical ozone production in storm outflow The STERAO-A storm simulation  
972 by DeCaria et al. (2005) indicated that additional ozone production attributable to lightning NO  
973 within the storm cloud during the lifetime of the storm was very small (~2 ppbv). However,  
974 simulation of the photochemistry over the 24 hours following the storm showed that an additional  
975 10 ppbv of ozone production in the upper troposphere can be attributed to lightning NO production.  
976 Convective transport of HO<sub>x</sub> precursors led to the generation of a HO<sub>x</sub> plume, which substantially  
977 aided the downstream ozone production. Ott et al. (2007) simulated the July 21, 1998 EULINOX  
978 thunderstorm. During the storm, the inclusion of lightning NO<sub>x</sub> in the model combined with  
979 convectively-transported boundary layer NO<sub>x</sub> from the Munich, Germany region resulted in  
980 sufficiently large NO<sub>x</sub> mixing ratios to cause a small titration loss of ozone (on average less than  
981 4 ppbv) at all model levels. Simulations of the chemical environment in the 24 hours following the  
982 storm show on average a small increase in the net production of ozone at most levels resulting  
983 from lightning NO<sub>x</sub>, maximizing at approximately 5 ppbv per day at 5.5 km. Between 8 and 10.5  
984 km, lightning NO<sub>x</sub> caused decreased net ozone production. Ren et al. (2008) found that net  
985 tropospheric ozone production proceeded at a median rate of ~11 ppbv per day above 9 km in the  
986 Intercontinental Transport Experiment (INTEX-A) in which the effects of frequent deep  
987 convection over the United States dominated the upper troposphere. Apel et al. (2012) noted that  
988 a box model calculation indicated a net ozone increase of ~10 ppbv over a few hours following  
989 observed convection with lightning over Canada in the Arctic Research of the Composition of the  
990 Troposphere from Aircraft and Satellite (ARCTAS) experiment. Apel et al. (2015) performed box  
991 modeling of the chemistry downwind of two DC3 storms in northeast Colorado on June 22, 2012  
992 finding greater ozone production over 2 days (14 ppbv) in the southern storm with more LNO<sub>x</sub>  
993 than in the northern storm (11 ppbv). Brune et al. (2018) studied ozone production in the outflow  
994 of the June 21, 2012 DC3 mesoscale convective system. Their Box model calculations yielded a  
995 13 ppbv increase in ozone over 5 hours, similar to the observed 14 ppbv increase. This rate of  
996 increase is larger than others in the literature, perhaps because for a portion of the 5 hours the  
997 outflow was in cirrus cloud, in which photolysis rates may have been larger than clear-sky values  
998 due to multiple scattering. Using a regional chemistry model, Pickering et al. (2023) estimated that  
999 net ozone production in the upper tropospheric outflow of a severe high flash rate storm observed  
1000 over Oklahoma proceeded at a rate of 10-11 ppbv day<sup>-1</sup> during the first 24 hours of downwind  
1001 transport. Downwind photochemical production of ozone due to LNO<sub>x</sub> accounted for much of the  
1002 recovery of upper tropospheric ozone following large reductions due to convective transport of  
1003 lower ozone boundary layer air.

### 1004 **3.5.6. Summary of LNO<sub>x</sub>**

1005 LNO<sub>x</sub> is responsible for the largest fraction of upper tropospheric ozone in the tropics year-round  
1006 and in the mid-latitudes in summer. Effects on longwave radiation due to ozone are most sensitive  
1007 due to the ozone near the tropopause. Therefore, it is of great importance to have knowledge of  
1008 the trends in ozone in this region that are due to changes in frequency and characteristics of

1009 lightning flashes. Considerable uncertainty remains concerning trends in global thunder days. No  
1010 long-term trend in global flash rates has been found. However, regionally important trends have  
1011 been noted in CONUS and in China, which tend to be correlated to the decreasing atmospheric  
1012 aerosol content. An increasing trend at Arctic latitudes has been noted, as that region rapidly  
1013 warms. Future trends in flash rate also are uncertain, with conflicting predictions coming from  
1014 models with differing flash rate parameterizations. Flash characteristics (e.g., flash rate, flash  
1015 extent, flash energy or peak current, intracloud fraction) have been found to have important  
1016 implications for LNO<sub>x</sub> production per flash. Insufficient knowledge of these characteristics on a  
1017 global scale makes it highly uncertain to estimate changes in LNO<sub>x</sub> production, even with  
1018 knowledge of flash rate trends.

1019

### 1020 **3.6. Soil NO and HONO emissions and their impacts on O<sub>3</sub>**

1021 Nitrous acid (HONO) is produced from microbial activity in soils with a similar mechanism and  
1022 strength as NO (Oswald et al., 2013). This emission source may partially account for the current  
1023 mismatch between observed and simulated HONO levels in the lower troposphere (Su et al.,  
1024 2011; Yang et al., 2020). Zhang et al. (2016) estimate a 29 % contribution of soil-HONO to the  
1025 HONO sources in China. This may also contribute significantly to OH production with important  
1026 implications for the HO<sub>x</sub> and O<sub>3</sub> budget. To account for this emission source and assess the  
1027 global potential for atmospheric pollution soil-HONO emissions have been parameterized based  
1028 on the HONO/NO emission ratio measured at multiple field samples (taken from different  
1029 regions of the world) and up-scale it to the 4 major land cover types applied to the whole globe.  
1030 The study estimates a global emission source of 7 TgN/yr from soil-HONO in 2009 (Emmerichs  
1031 et al., 2023). This is at the lower end of the estimated range of 7.4-12 TgN/yr presented by Wu et  
1032 al. (2022) for 2017 who employ an empirical and statistical model in combination with  
1033 observations. Due to the importance of NO and HONO soil emissions for the O<sub>3</sub> budget their  
1034 variability and historical and future trends are described here and linked to O<sub>3</sub>. Additionally, we  
1035 discuss a modification of the soil NO emission scheme.

#### 1036 **3.6.1. Global modeling of reactive nitrogen emissions from soil**

1037 In this section, we present a short overview of the soil-NO emission algorithms and estimates for  
1038 regional and global emissions. The emission of nitrogen oxides (NO) from the soil is the major  
1039 source of NO<sub>x</sub> in unpolluted regions accounting for 15-25 % of global emissions (Weng et al.,  
1040 2020, Vinken et al., 2014). Thereby, NO is produced from the nitrification in soil (microbial  
1041 activity) and depends non-linearly on soil properties like pH, carbon and nutrient content,  
1042 temperature, and soil moisture (Gödde and Conrad 2000, Oswald et al. 2013). Model algorithms  
1043 estimate soil-NO emissions with a function dependent on biological and meteorological drivers.  
1044 The common empirical approach by Yienger and Levy (1995), which is used in the current  
1045 CMIP6 simulations (Szopa et al. 2022), is based on a biome-specific emission factor, soil  
1046 temperature, precipitation, and the canopy uptake reduction factor. The resulting global estimate  
1047 is in the range of 3.3-7.7 TgN/yr which is, however, only at the lower end of the more recent  
1048 model and observation-based estimates. The Yienger and Levy (1995) approach generally  
1049 underestimates soil NO for all landcover types except in the tundra and rainforest due to the  
1050 pulsing parameterization, which describes a large NO<sub>x</sub> release at the wetting of very dry soil and  
1051 the subsequent rapid decay (Steinkamp et al., 2009). This is accounted for in the more  
1052 mechanistic approach by Hudman et al. (2012) representing pulsing of the emissions following  
1053 dry spells and N-inputs from chemical fertilizer and atmospheric N-deposition. This approach  
1054 calculates spatial and temporal patterns of soil moisture, temperature, pulsing, fertilizer, manure

1055 and atmospheric N deposition and biome overall replacing the emission factors by Yienger and  
 1056 Levy (1995) which yields in comparison 34 % more annual global soil emissions of nitrogen  
 1057 oxide (10.7 TgN/yr). Satellite top-down estimates range from 7.9 TgN/yr (Miyazaki et al., 2017:  
 1058 2005-2014, assimilation of satellite data sets) to 16.7 TgN/yr (Vinken et al., 2014; GEOS-Chem  
 1059 and OMI). The emission of soil-NO varies regionally with small sources in Australia (~0.5  
 1060 TgN/yr), Europe, Russia and Southern Hemisphere (SH) Africa (0.7 TgN/yr, 0.8 TgN/yr),  
 1061 America (0.9-1 TgN/yr) and high values in S.E. Asia and Northern Hemisphere (NH) Africa (2-  
 1062 2.1 TgN/yr). The emission estimates (here for 0.25° lat. × 0.3125° lon.) increase with resolution  
 1063 in some regions like Europe by 38 % (Weng et al., 2020).

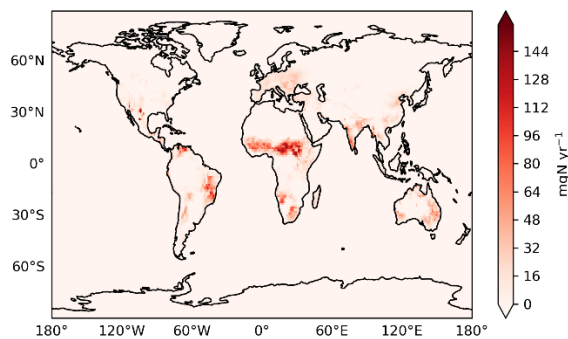
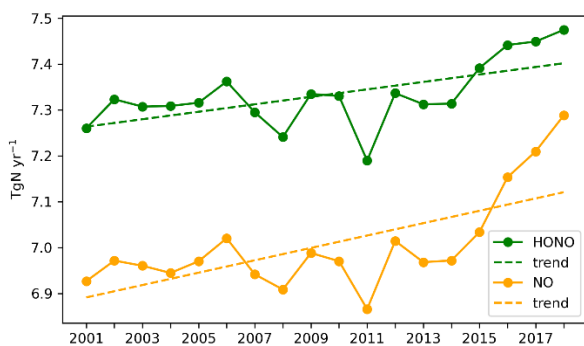
1064 Nitrous acid (HONO), a major OH source, is also produced from microbial activity in soils with  
 1065 a similar mechanism and strength as NO (Oswald et al., 2013). This additional emission source  
 1066 may account for the current mismatch between models and measurements representing HONO  
 1067 levels in the lower troposphere (Su et al., 2011; Yang et al., 2020). Soil emissions of HONO play  
 1068 a major role in the daytime-HONO concentrations in rural areas (in the lowest layers) where  
 1069 traffic emissions and NO<sub>2</sub> heterogeneous reactions occur less than in urban areas (Wu et al.  
 1070 2022). HONO photolysis is a main OH source and impacts the oxidation capacity of the  
 1071 atmosphere (Zhang 2016, 2019). Therefore, this may also contribute significantly to OH  
 1072 production with important implications for the HO<sub>x</sub> and O<sub>3</sub> budget.

### 1073 3.6.2. Variability and trends of soil emissions of NO and HONO in the last 15 years

1074 The magnitude of soil emissions varies strongly with season where the emissions rise from  
 1075 January and July by a factor of 2.5 (Weng et al., 2020). This follows the meteorological  
 1076 variability as for instance, heavy rainfall over dry grasslands/forests causes a pulse of soil NO  
 1077 emissions coupled with the usage of fertilizer (Hudman et al., 2012). According to the CCM1  
 1078 simulations by Jöckel et al. (2016) (following the future ('medium high') climate scenario  
 1079 RCP6.0 the soil NO emissions show a positive trend since pre-industrial times with a steeper  
 1080 increase of up to 0.3 TgN/decade from the year 2000. As soil emissions of HONO rely on the  
 1081 same biogeochemical process with similar dependencies on temperature and water content as NO  
 1082 also increased from 2000 to 2019.

1083 For soil-HONO, however, the trend over 2005-2019 is much smaller, most pronounced in  
 1084 Central Africa (Figure 25). Thereby, the highest positive monthly anomalies occur mainly in the  
 1085 5 most recent years which is likely due to the more frequent heat wave occurrence, e.g. in Europe  
 1086 and North America. Overall, Africa relates the most (~30%) to the global anomaly (Figure 24 -  
 1087 Figure 25).

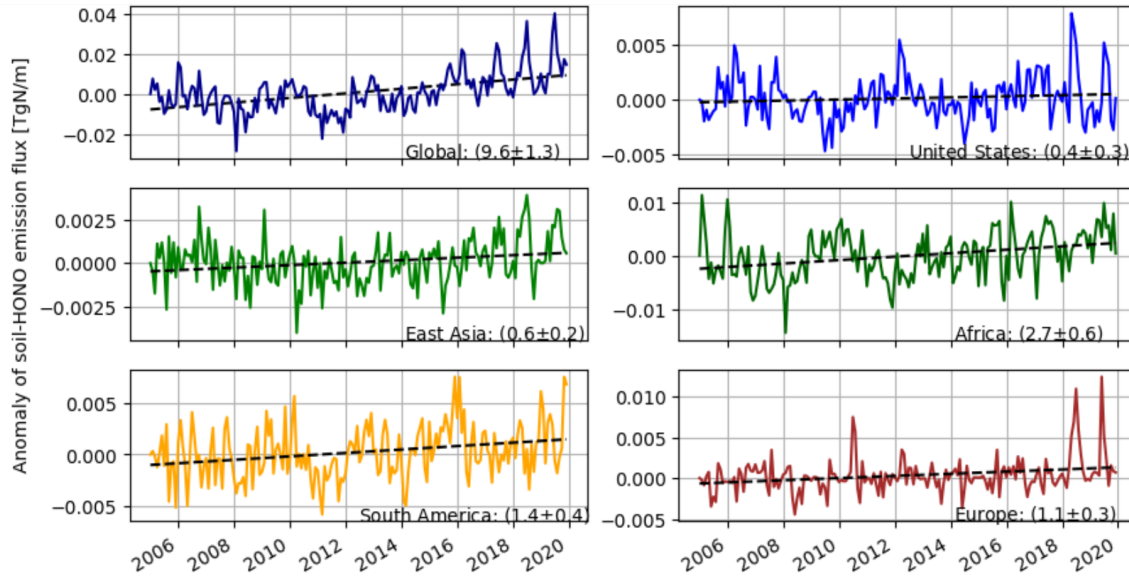
1088



1089

1090 Figure 24: Time series of soil-HONO and soil-NO emissions and their trends (left) and the mean  
 1091 global distribution of the soil-HONO emission trend for 2005-2019 based on monthly anomalies  
 1092 (right).

1093  
 1094  
 1095



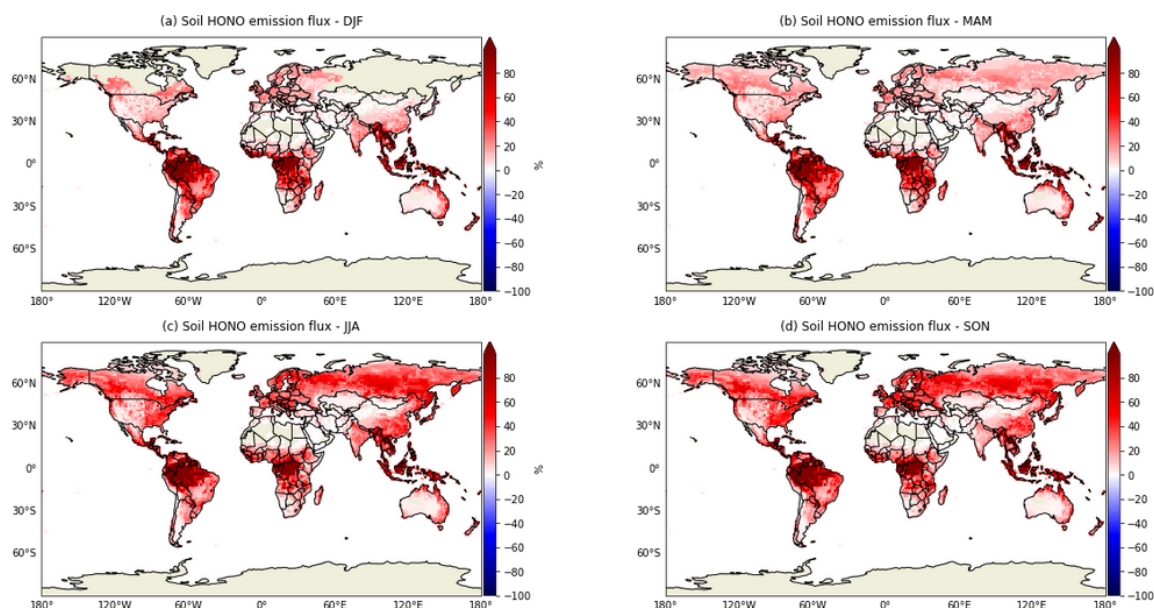
1096  
 1097 Figure 25: Monthly anomalies of HONO emissions from soil (de-seasonalized). The trend is  
 1098 given in  $10^{-5}$ , including the uncertainty estimate ( $2 \times$  standard deviation).

### 1099 3.6.3. Canopy Reduction Factor

1100 Most NO soil emission models (Yienger and Levy, 1995; Hudman et al., 2012) rely on an  
 1101 empirical canopy reduction scheme which represents loss processes in plants as the diffusion of  
 1102  $\text{NO}_2$  through the stomata and direct deposition to the cuticle. In particular, a large fraction of  
 1103  $\text{NO}_x$  (and peroxyacyl nitrate) loss during the night may be only explainable by non-stomatal  
 1104 processes (Delaria et al., 2020b). Mechanistically, the canopy reduction can be described by an  
 1105 efficient  $\text{NO}_x$  deposition to plants. Thus, Delaria et al. (2020a) points out that models already  
 1106 represent the uptake by vegetation and do not need to use a canopy reduction scheme. The  
 1107 potential change of NO soil emissions is shown by employing the global model  
 1108 ECHAM/MESy ( $1^\circ \times 1^\circ$ ) with an explicit trace gas uptake at stomata and cuticle (Emmerichs et  
 1109 al., 2021) for two different seasons in 2005 and 2006. Removing the canopy reduction factor in  
 1110 the model leads to a significant increase of soil NO emissions highest over tropical forests  
 1111 (Figure 26). The temporal variation follows the vegetational growth as in the Northern  
 1112 Hemisphere summer 50% higher emissions occur. These findings are reasonable as Hudman et  
 1113 al. (2012) estimated that the canopy reduction scheme overall lowers the NO emissions by 10-  
 1114 15% at grasslands and up to 85% over forests (GEOS-Chem at  $2^\circ \times 2.5^\circ$  in 2006). Consequently,  
 1115 improper accounting for the canopy reduction factor may imply a strong underestimation of the  
 1116 soil-N in densely forested regions and globally by about 31% (2005-2006).

1117





1118

1119 Figure 26: Relative difference Canopy Reduction soil HONO

1120

1121 **3.6.4. Projections of soil NO and variability in different climates**

1122 The future land use is predicted to change as a consequence of the growing demand for  
 1123 nutrition and biofuels which implies an increasing use of fertilizer. Consequently, NO soil  
 1124 emissions are estimated to rise by ~28% during the century to 11.5 TgN/yr at the end of 2100  
 1125 (Fowler et al., 2015). Similarly, Liu et al. (2021) estimate an increasing soil NO emission of 8.9  
 1126 TgN/yr by the year 2050 due to intensive nitrification processes.

1127 An increase of LAI by 10 %, in contrast, would lead to 1% lower emissions. In addition, several  
 1128 responses are expected from the changing climate. In fact, the 1°C higher temperature would  
 1129 cause ~5% increase of emissions (Weng et al., 2020). Following the future ('medium high')  
 1130 climate scenario RCP6.0 (Representative Concentration Pathway, 6 W/m<sup>2</sup> radiative forcing until  
 1131 2500, stabilization after 2150) used for the CMIP5 (Climate Model Intercomparison Project)  
 1132 simulations. Jöckel et al. (2016) suggest an increase of ~15 % soil NO emissions due to  
 1133 increasing soil temperature (an increase of soil microbes) since present-day (2010) until 2100.  
 1134 However, the most significant implications for large-scale denitrification activity are changing  
 1135 rainfall and the regional hydrological cycles (Fowler et al., 2015). In general, soil NO<sub>x</sub> will play  
 1136 a more important role for the global budget in the troposphere due to the decreasing  
 1137 anthropogenic emissions in the future. Therefore, increasing NO<sub>x</sub>-soil emissions may slow down  
 1138 the decrease of O<sub>3</sub> in response to declining anthropogenic emissions (Wu et al. 2022).

1139

1140 **3.6.5. Next steps with biogeochemical models implemented in ESMs**

1141 Uncertainties of modeling soil nitrogen emissions are associated with the model input and  
 1142 parameters (Wang and Chen 2012). Process-based biogeochemical models which also consider  
 1143 the complexity of soil emission processes as DNDC (Denitrification–Decomposition) are needed  
 1144 (Li et al., 2011). The capability to represent interactive biogeochemical cycles allows for  
 1145 instance for the online calculation of crop nutrition from soil. Also, a model like CLM5  
 1146 distinguishes between natural and agricultural soils which more accurately predicts the fertilizer

1147 usage (Fung et al., 2022). Resolving the soil and litter biogeochemical dynamics vertically, in  
1148 addition, lead to a more efficient retainment and recycling of N by the ecosystem (Koven et al.,  
1149 2013). However, these models should be calibrated to multiple sites (Wang et al., 2019) which is  
1150 limited by the availability of measurement data, especially when it comes to global modeling.

1151

#### 1152 **4. Conclusion**

1153 In this article, we investigate temporal and spatial trends and variability of tropospheric ozone in  
1154 relation to its precursors using satellite products, ozonesonde measurements, and model  
1155 simulations. Our results show that ozone has positive trends at all latitudes and column depths  
1156 regardless of the tropopause height within  $\pm 100$  hPa. The positive trends in the 30-60°N band are  
1157 due to increasing trends over Canada and Alaska and are slightly offset by the small negative  
1158 trends over the northeastern US and Europe. The lower trends in the bands 30-60°N and 30-60°S  
1159 are due to the offsetting impact of negative trends over Eastern US and Europe in the north, and  
1160 Australia and South Africa in the south, respectively. The decreasing trends of TrC-O<sub>3</sub> over parts  
1161 of the northeastern US and Europe are likely due to the decreasing trend of TrC-NO<sub>2</sub>, which is  
1162 due to the effective measures applied over the last two decades to mitigate air pollution in these  
1163 regions. TrC-HCHO trends are decreasing in the Eastern US, some parts of northern and western  
1164 Africa, and western and northern Europe, and increasing in South Asia, central Africa, northern  
1165 Australia, and Brazil. TrC-HCHO trends are consistent with that of TrC-O<sub>3</sub> over Eastern US and  
1166 Europe. Simulated O<sub>3</sub> and its precursors are in good agreement with satellite measurements.  
1167 Considering different latitude bands, the TrC-O<sub>3</sub> highest trends are simulated between 30° S and  
1168 60° N, consistent with calculated trends based on satellite observations. The middle and upper  
1169 troposphere make the largest contributions to the simulated TrC-O<sub>3</sub> trend globally, with large  
1170 contributions from the upper troposphere driving the simulated TrC-O<sub>3</sub> trend at 30°S-30°N and  
1171 counteracting the negative TrC-O<sub>3</sub> trend in the southern midlatitudes.

1172 We have also shed light on NO<sub>x</sub> lightning and its relation to ozone trends. LNO<sub>x</sub> is responsible  
1173 for the largest fraction of upper tropospheric ozone in the tropics year-round and in the mid-  
1174 latitudes in summer. Ozone Radiative forcing is due to the ozone near the tropopause. An  
1175 increasing trend of LNO<sub>x</sub> at Arctic latitudes has been noted, as that region rapidly warms.  
1176 However, future trends in flash rate are uncertain, with conflicting predictions coming from  
1177 models with differing flash rate parameterizations. Soil HONO emissions had their highest  
1178 positive monthly anomalies mainly in the 5 most recent years which is likely due to the more  
1179 frequent heat wave occurrence, e.g. in Europe and North America. Soil HONO trends are highest  
1180 in Africa accounting for ~30% of the global anomaly. Soil NO<sub>x</sub> emissions could play an  
1181 important role in the tropospheric NO<sub>x</sub> global budget due to the decreasing anthropogenic  
1182 emissions in the future. Therefore, the expected increase in NO<sub>x</sub>-soil emissions may slow down  
1183 the decrease of O<sub>3</sub> in response to declining anthropogenic emissions. Overall, this study  
1184 presented a comprehensive overview of tropospheric ozone trends in relation to its precursors in  
1185 different spatial and temporal scales.

1186 Competing interests: At least one of the (co-)authors is a member of the editorial board of  
1187 Atmospheric Chemistry and Physics

#### 1188 **Acknowledgment**

1189 This study was partially funded by the NSF AGS, grant number 1900795, USF Creative  
1190 Scholarship Grant 2022. A part of the research was conducted at the Jet Propulsion Laboratory,  
1191 California Institute of Technology, under a contract with NASA. HP has received funding from

1192 the Ministerio de Ciencia e Innovación through the MITIGATE project (grant no. PID2020-  
1193 113840RA-I00 funded by MCIN/AEI/10.13039/501100011033) and the Ramon y Cajal grant  
1194 (RYC2021-034511-I, MCIN / AEI / 10.13039/501100011033 and European Union  
1195 NextGenerationEU/PRTR). The GEOS-GMI simulation was supported by the NASA's Making  
1196 Earth System Data Records for Use in Research Environments (MEaSUREs) program and the  
1197 high-performance computing resources for GEOS-GMI were provided by the NASA Center for  
1198 Climate Simulation (NCCS).

1199

## 1200 5. References

- 1201 Allen, D., Pickering, K., Duncan, B., and Damon, M. (2010), Impact of lightning NO  
1202 emissions on North American photochemistry as determined using the Global  
1203 Modeling Initiative (GMI) model, *J. Geophys. Res.*, 115, D22301,  
1204 doi:10.1029/2010JD014062.
- 1205 Allen, D. J., Pickering, K. E., Pinder, R. W., Henderson, B. H., Appel, K. W., and Prados, A.  
1206 (2012), Impact of lightning-NO on eastern United States photochemistry during the  
1207 summer of 2006 as determined using the CMAQ model, *Atmos. Chem.*  
1208 *Phys.*, 12, 1737-1758, doi:10.5194/acp-12-1737-2012.
- 1209 Allen, D. J., Pickering, K. E., Bucsela, E., van Geffen, J., Lapierre, J., Koshak, W., & Eskes,  
1210 H. (2021b). Observations of Lightning NO<sub>x</sub> production from Tropospheric Ozone  
1211 Monitoring Instrument Case Studies over the United States, *J. Geophys. Res.*, 126  
1212 (10), <https://doi.org/10.1029/2020JD034174>.
- 1213 Allen, D. J., Pickering, K. E., Lamsal, L., Mach, D., Quick, M. G., Lapierre, J., Janz, S.,  
1214 Koshak, W., Kowalewski, M. & Blakeslee, R. (2021a), Observations of Lightning  
1215 NO<sub>x</sub> production from GOES-R Post Launch Test Field Campaign Flights, *J. Geophys.*  
1216 *Res.*, 126 (8), <https://doi.org/10.1029/2020JD033769>.
- 1217 Allen, D., J., Pickering, K. E., Bucsela, E., Krotkov, N., and Holzworth, R. (2019), Lightning  
1218 NO<sub>x</sub> Production in the Tropics as Determined Using OMI NO<sub>2</sub> Retrievals and  
1219 WWLLN Stroke Data, *J. Geophys. Res.*, <https://doi.org/10.1029/2018JD029824>.
- 1220 Apel, E. C., J. R. Olson, J. H. Crawford, R. S. Hornbrook, A. J. Hills, C. A. Cantrell, L. K.  
1221 Emmons, D. J. Knapp, S. Hall, R. L. Mauldin III, A. J. Weinheimer, A. Fried, D. R.  
1222 Blake, J. D. Crouse, J. M. St. Clair, P. O. Wennberg, G. S. Diskin, H. E. Fuelberg,  
1223 A. Wisthaler, T. Mikoviny, W. Brune, and D. D. Riemer, (2012) Impact of the deep  
1224 convection of isoprene and other reactive trace species on radicals and ozone in the  
1225 upper troposphere, *Atmos. Chem. Phys.*, 12, 1135–1150, [www.atmos-chem-](http://www.atmos-chem-phys.net/12/1135/2012/)  
1226 [phys.net/12/1135/2012/](http://www.atmos-chem-phys.net/12/1135/2012/)doi:10.5194/acp-12-1135-2012.
- 1227 Apel, E. C., et al. (2015), Upper tropospheric ozone production from lightning NO<sub>x</sub>-  
1228 impacted convection: Smoke ingestion case study from the DC3 campaign, *J.*  
1229 *Geophys. Res. Atmos.*, 120, doi:10.1002/2014JD022121.
- 1230 Archibald, A.T., et al. 2020. Tropospheric Ozone Assessment Report: A critical review of  
1231 changes in the tropospheric ozone burden and budget from 1850 to 2100. *Elem Sci*  
1232 *Anth*, 8: 1. DOI: <https://doi.org/10.1525/elementa.2020.034>, 2020.

- 1233 ASDC, MOPITT CO gridded monthly means (Near and Thermal Infrared Radiances) V009  
1234 [Data set]. NASA Langley Atmospheric Science Data Center DAAC. Retrieved from  
1235 <https://doi.org/10.5067/TERRA/MOPITT/MOP03JM.009>, 2024.
- 1236 Barret, B., De Mazière, M., and Mahieu, E.: Ground-based FTIR measurements of CO from  
1237 the Jungfraujoch: characterisation and comparison with in situ surface and MOPITT  
1238 data, *Atmos. Chem. Phys.*, 3, 2217–2223, <https://doi.org/10.5194/acp-3-2217-2003>,  
1239 2003.
- 1240 Bauwens, M.; Compornolle, S.; Stavrakou, T.; Müller, J.; Gent, J.; Eskes, H.; Levelt, P.F.;  
1241 van der A, R.; Veefkind, J.P.; Vlietinck, J.; et al. Impact of Coronavirus Outbreak on  
1242 NO<sub>2</sub> Pollution Assessed Using TROPOMI and OMI Observations. *Geophys. Res.*  
1243 *Lett.* 2020, 47.
- 1244 Beirle, S., H. Huntrieser, and T Wagner (2010), Direct satellite observation of lightning-  
1245 produced NO<sub>x</sub>, *Atmos. Chem. Phys.*, 10(22), 10965-10986, doi:10.5194/acp-10-  
1246 10965.
- 1247 Boersma, K., Eskes, H., Richter, A., De Smedt, I., Lorente, A., Beirle, S., Van Geffen, J.,  
1248 Peters, E., Van Roozendaal, M., and Wagner, T.: QA4ECV NO<sub>2</sub> tropospheric and  
1249 stratospheric vertical column data from OMI (Version 1.1) (data set), Royal  
1250 Netherlands Meteorological Institute (KNMI), [https://doi.org/10.21944/qa4ecv-no2-  
1251 omi-v1.1](https://doi.org/10.21944/qa4ecv-no2-omi-v1.1), 2017a.
- 1252 Boersma, K., Eskes, H., Richter, A., De Smedt, I., Lorente, A., Beirle, S., Van Geffen, J.,  
1253 Peters, E., Van Roozendaal, M., and Wagner, T.: QA4ECV NO<sub>2</sub> tropospheric and  
1254 stratospheric vertical column data from GOME-2 (Version 1.1) (data set), Royal  
1255 Netherlands Meteorological Institute (KNMI), [https://doi.org/10.21944/qa4ecv-no2-  
1256 gome2a-v1.1](https://doi.org/10.21944/qa4ecv-no2-gome2a-v1.1), 2017b.
- 1257 Boersma, K., Eskes, H., Richter, A., De Smedt, I., Lorente, A., Beirle, S., Van Geffen, J.,  
1258 Peters, E., Van Roozendaal, M., and Wagner, T.: QA4ECV NO<sub>2</sub> tropospheric and  
1259 stratospheric vertical column data from SCIAMACHY (Version 1.1) (data set), Royal  
1260 Netherlands Meteorological Institute (KNMI), [https://doi.org/10.21944/qa4ecv-no2-  
1261 scia-v1.1](https://doi.org/10.21944/qa4ecv-no2-scia-v1.1), 2017c.
- 1262 Boersma, K. F., Eskes, H. J., Richter, A., De Smedt, I., Lorente, A., Beirle, S., van Geffen, J.,  
1263 H. G. M., Zara, M., Peters, E., Van Roozendaal, M., Wagner, T., Maasackers, J. D.,  
1264 van der A, R. J., Nightingale, J., De Rudder, A., Irie, H., Pinardi, G., Lambert, J.-C.,  
1265 and Compornolle, S. C.: Improving algorithms and uncertainty estimates for satellite  
1266 NO<sub>2</sub> retrievals: results from the quality assurance for the essential climate variables  
1267 (QA4ECV) project, *Atmos. Meas. Tech.*, 11, 6651–6678, [https://doi.org/10.5194/amt-  
1268 11-6651-2018](https://doi.org/10.5194/amt-11-6651-2018), 2018.
- 1269 Brune, W. H., et al. (2018) Atmospheric oxidation in the presence of clouds during the Deep  
1270 Convective Clouds and Chemistry (DC3) study, *Atmos. Chem. Phys.*, 18, 14493–14510,  
1271 2018, <https://doi.org/10.5194/acp-18-14493-2018>.
- 1272 Bruning, E. C. & Thomas, R. J. (2015), Lightning channel length and flash energy  
1273 determined from moments of the flash area distribution, *J. Geophys. Res. Atmos.*,  
1274 120, 8925–8940, doi:[10.1002/2015JD023766](https://doi.org/10.1002/2015JD023766)

- 1275 Buchholz, R.R.; Deeter, M.N.; Worden, H.M.; Gille, J.; Edwards, D.P.; Hannigan, J.W.;  
 1276 Jones, N.B.; Paton-Walsh, C.; Griffith, D.W.T.; Smale, D.; et al. Validation of  
 1277 MOPITT carbon monoxide using ground-based Fourier transform infrared  
 1278 spectrometer data from NDACC. *Atmos. Meas. Tech.* 2017, 10, 1927–1956.
- 1279 Buchholz, R. R., Worden, H. M., Park, M., Francis, G., Deeter, M. N., Edwards, D. P.,  
 1280 Emmons, L. K., Gaubert, B., Gille, J., Martinez-Alonso, S., Tang, W., Kumar, R.,  
 1281 Drummond, J. R., Clerbaux, C., George, M., Coheur, P.-F., Hurtmans, D., Bowman,  
 1282 K. W., Luo, M., Payne, V. H., Worden, J. R., Chin, M., Levy, R. C., Warner, J., Wei,  
 1283 Z., and Kulawik, S. S.: Air pollution trends measured from Terra: CO and AOD over  
 1284 industrial, fire-prone, and background regions, *Remote Sens. Environ.*, 256, 112275,  
 1285 <https://doi.org/10.1016/j.rse.2020.112275>, 2021.
- 1286 Bucsela, E. J., K. E. Pickering, T. L. Huntemann, R. C. Cohen, A. Perring, J. F. Gleason, R.  
 1287 J. Blakeslee, R. I. Albrecht, R. Holzworth, J. P. Cipriani, D. Vargas-Navarro, I. Mora-  
 1288 Segura, A. Pacheco-Hernández, S. Laporte-Molina, (2010) Lightning-generated NO<sub>x</sub>  
 1289 seen by OMI during NASA's TC<sup>4</sup> experiment, *J. Geophys. Res.*, 115, D00J10,  
 1290 doi:10.1029/2009JD013118.
- 1291 Bucsela, E., Pickering, K. E., Allen, D., Holzworth, R., and Krotkov, N. (2019), Midlatitude  
 1292 lightning NO<sub>x</sub> Production Efficiency Inferred from OMI and WLLN Data, *J.*  
 1293 *Geophys. Res.*, <https://doi.org/10.1029/2019JD030561>.
- 1294 Canadell, J.G., P.M.S. Monteiro, M.H. Costa, L. Cotrim da Cunha, P.M. Cox, A.V. Eliseev,  
 1295 S. Henson, M. Ishii, S. Jaccard, C. Koven, A. Lohila, P.K. Patra, S. Piao, J. Rogelj, S.  
 1296 Syampungani, S. Zaehle, and K. Zickfeld: Global Carbon and other Biogeochemical  
 1297 Cycles and Feedbacks. In *Climate Change 2021: The Physical Science Basis.*  
 1298 Contribution of Working Group I to the Sixth Assessment Report of the  
 1299 Intergovernmental Panel on Climate Change [Masson-Delmotte, V., P. Zhai, A.  
 1300 Pirani, S.L. Connors, C. Péan, S. Berger, N. Caud, Y. Chen, L. Goldfarb, M.I. Gomis,  
 1301 M. Huang, K. Leitzell, E. Lonnoy, J.B.R. Matthews, T.K. Maycock, T. Waterfield, O.  
 1302 Yelekçi, R. Yu, and B. Zhou (eds.)]. Cambridge University Press, Cambridge, United  
 1303 Kingdom and New York, NY, USA, pp. 673–816, doi: [10.1017/9781009157896.007](https://doi.org/10.1017/9781009157896.007),  
 1304 2021.
- 1305 Cazorla, M. and Herrera, E.: An ozonesonde evaluation of spaceborne observations in the  
 1306 Andean tropics, *Sci Rep*, 12, <https://doi.org/10.1038/s41598-022-20303-7>, 2022.
- 1307 Chang K-L, Petropavlovskikh I, Cooper OR, Schultz MG, Wang T. Regional trend analysis  
 1308 of surface ozone observations from monitoring networks in eastern North America,  
 1309 Europe and East Asia. *Elem Sci Anth.*, 5:50. DOI: 10.1525/elementa.243, 2017.
- 1310 Chang, K.-L., Cooper, O. R., Gaudel, A., Petropavlovskikh, I., and Thouret, V.: Statistical  
 1311 regularization for trend detection: an integrated approach for detecting long-term  
 1312 trends from sparse tropospheric ozone profiles, *Atmos. Chem. Phys.*, 20, 9915–9938,  
 1313 <https://doi.org/10.5194/acp-20-9915-2020>, 2020.
- 1314 Chang, K.-L., Cooper, O. R., Gaudel, A., Allaart, M., Ancellet, G., Clark, H., et al.  
 1315 (2022). Impact of the COVID-19 economic downturn on tropospheric ozone trends:  
 1316 An uncertainty weighted data synthesis for quantifying regional anomalies above  
 1317 western North America and Europe. *AGU Advances*, 3,  
 1318 e2021AV000542. <https://doi.org/10.1029/2021AV000542>, 2022.

- 1319 Chang K-L, Martin G. Schultz, Gerbrand Koren, Niklas Selke, Guidance note on best  
1320 statistical practices for TOAR analyses, <https://doi.org/10.48550/arXiv.2304.14236>,  
1321 2023.
- 1322 Chang, K.-L., Cooper, O. R., Gaudel, A., Petropavlovskikh, I., Effertz, P., Morris, G., and  
1323 McDonald, B. C.: Technical note: Challenges of detecting free tropospheric ozone  
1324 trends in a sparsely sampled environment, EGU sphere [preprint],  
1325 <https://doi.org/10.5194/egusphere-2023-2739>, 2024.
- 1326 Chen, Z., Jane Liu, Xiushu Qie, Xugeng Cheng, Mengmiao Yang, Lei Shu, Zhou  
1327 Zang, Stratospheric influence on surface ozone pollution in China, *Nature*  
1328 *Communications*, 10.1038/s41467-024-48406-x, **15**, 1, 2024.
- 1329 Christiansen, A., Mickley, L. J., Liu, J., Oman, L. D., and Hu, L.: Multidecadal increases in  
1330 global tropospheric ozone derived from ozonesonde and surface site observations: can  
1331 models reproduce ozone trends?, *Atmos Chem Phys*, 22, 14751–14782,  
1332 <https://doi.org/10.5194/acp-22-14751-2022>, 2022.
- 1333 Cooper, O. R., Schultz, M. G., Schröder, S., Chang, K. L., Gaudel, A., Benítez, G. C.,  
1334 Cuevas, E., Fröhlich, M., Galbally, I. E., Molloy, S., Kubistin, D., Lu, X., McClure-  
1335 Begley, A., Nédélec, P., O’Brien, J., Oltmans, S. J., Petropavlovskikh, I., Ries, L.,  
1336 Senik, I., Sjöberg, K., Solberg, S., Spain, G. T., Spangl, W., Steinbacher, M.,  
1337 Tarasick, D., Thouret, V., and Xu, X.: Multi-decadal surface ozone trends at globally  
1338 distributed remote locations, *Elementa*, 8, <https://doi.org/10.1525/elementa.420>, 2020.
- 1339 Cummings, K. A., T. L. Huntemann, and K. E. Pickering (2013), Cloud-resolving chemistry  
1340 simulation of a Hector thunderstorm, *Atmos. Chem. Phys.*, 13(5), 2757–2777,  
1341 doi:10.5194/acp-13-2757.
- 1342 DeCaria, A., K. Pickering, G. Stenchikov, J. Scala, J. Stith, J. Dye, B. Ridley, and P.  
1343 Laroche, A cloud-scale model study of lightning-generated NO<sub>x</sub> in an individual  
1344 thunderstorm during STERAO-A, *J. Geophys. Res.*, 105, 11,601–11,616, 2000.
- 1345 DeCaria, A. J., K. E. Pickering, G. L. Stenchikov, and L. E. Ott (2005), Lightning-generated  
1346 NO<sub>x</sub> and its impact on tropospheric ozone production: A three-dimensional modeling  
1347 study of a STERAO-A thunderstorm, *J. Geophys. Res.*, 110, D14303,  
1348 doi:10.1029/2004JD005556. Deeter, M., Francis, G., Gille, J., Mao, D., Martínez-  
1349 Alonso, S., Worden, H., Ziskin, D., Drummond, J., Commane, R., Diskin, G., and  
1350 McKain, K.: The MOPITT Version 9 CO product: sampling enhancements and  
1351 validation, *Atmos. Meas. Tech.*, 15, 2325–2344, <https://doi.org/10.5194/amt-15-2325-2022>, 2022.
- 1353 De Smedt, I., Theys, N., Yu, H., Danckaert, T., Lerot, C., Compennolle, S., Van Roozendael,  
1354 M., Richter, A., Hilboll, A., Peters, E., Pedernana, M., Loyola, D., Beirle, S.,  
1355 Wagner, T., Eskes, H., van Geffen, J., Boersma, K. F., and Veeffkind, P.: Algorithm  
1356 theoretical baseline for formaldehyde retrievals from S5P TROPOMI and from the  
1357 QA4ECV project, *Atmos. Meas. Tech.*, 11, 2395–2426, <https://doi.org/10.5194/amt-11-2395-2018>, 2018 Fadnavis, S., Sagalgile, A., Sonbawne, S., Vogel, B., Peter, T.,  
1359 Wienhold, F. G., Dirksen, R., Oelsner, P., Naja, M., and Müller, R.: Comparison of  
1360 ozonesonde measurements in the upper troposphere and lower Stratosphere in  
1361 Northern India with reanalysis and chemistry-climate-model data, *Sci Rep*, 13, 7133,  
1362 <https://doi.org/10.1038/s41598-023-34330-5>, 2023.

- 1363 Duncan, B. N., Strahan, S. E., Yoshida, Y., Steenrod, S. D., and Livesey, N.: Model study of  
 1364 the cross-tropopause transport of biomass burning pollution, *Atmos. Chem. Phys.*, 7,  
 1365 3713–3736, <https://doi.org/10.5194/acp-7-3713-2007>, 2007.
- 1366 Elguindi, N., Granier, C., Stavrakou, T., Darras, S., Bauwens, M., Cao, H., Chen, C., Denier  
 1367 van der Gon, H. A. C., Dubovik, O., Fu, T. M., Henze, D. K., Jiang, Z., Keita, S.,  
 1368 Kuenen, J. J. P., Kurokawa, J., Liousse, C., Miyazaki, K., Müller, J. F., Qu, Z.,  
 1369 Solmon, F., and Zheng, B.: Intercomparison of Magnitudes and Trends in  
 1370 Anthropogenic Surface Emissions From Bottom-Up Inventories, Top-Down  
 1371 Estimates, and Emission Scenarios, *Earths Future*, 8, e2020EF001520,  
 1372 <https://doi.org/10.1029/2020EF001520>, 2020.
- 1373 Elshorbany, Y. F., Kurtenbach, R., Wiesen, P. Lissi, E., Rubio, M., Villena, G., Gramsch, E.,  
 1374 Rickard, A. R., Pilling, M. J., Kleffmann, J.: Oxidation capacity of the city air of  
 1375 Santiago, Chile, *Atmospheric Chemistry and Physics*, 9, 2257-2273, 2009.
- 1376 Elshorbany, Y. F., Barnes, I., Becker, K. H., Kleffmann, J., and Wiesen, P.: Sources and  
 1377 Cycling of Tropospheric Hydroxyl Radicals-An Overview, *Zeitschrift für*  
 1378 *Physikalische Chemie*, 224, 967-987, DOI:10.1524/zpch.2010.6136, 2010.
- 1379 Elshorbany, Y. F., Kleffmann, J., Hofzumahaus, A., Kurtenbach, R., Wiesen, P., Dorn, H.-P.,  
 1380 Schlosser, E., Brauers, T., Fuchs, H., Rohrer, F., Wahner, A., Kanaya, Y., Yoshino,  
 1381 A., Nishida, S., Kajii, Y., Martinez, M., Rudolf, M., Harder, H., Lelieveld, J., Elste,  
 1382 T., Plass-Dülmer, C., Stange, G., and Berresheim, H.: HO<sub>x</sub> Budgets during  
 1383 HO<sub>x</sub>Comp: a Case Study of HO<sub>x</sub> Chemistry under NO<sub>x</sub> limited Conditions, *J.*  
 1384 *Geophys. Res.*, 117, D03307, doi: 10.1029/2011JD017008, 2012.
- 1385 Elshorbany, Y. F., Crutzen, P. J., Steil, B., Pozzer, A., Tost, H., and Lelieveld, J.: Global and  
 1386 regional impacts of HONO on the chemical composition of clouds and aerosols,  
 1387 *Atmos. Chem. Phys.*, 14, 1167–1184, <https://doi.org/10.5194/acp-14-1167-2014>,  
 1388 2014.
- 1389 Elshorbany, Y. F.; Hannah C. Kapper; Jerald R. Ziemke; Scott A. Parr; (2021). The Status of  
 1390 Air Quality in the United States During the COVID-19 Pandemic: A Remote Sensing  
 1391 Perspective . *Remote Sensing*, doi:10.3390/rs13030369, 2021.
- 1392 Fadnavis et al., 2024, in preparation.
- 1393 Fehr, T., H. Höller, and H. Huntrieser (2004), Model study on production and transport of  
 1394 lightning-produced NO<sub>x</sub> in a EULINOX supercell storm, *J. Geophys. Res.*, 109,  
 1395 D09102, doi:10.1029/2003JD003935.
- 1396 Finney, D. L., R. M. Doherty, O. Wild, H. Huntrieser, H. C. Pumphrey, and A. M. Blyth  
 1397 (2014), Using cloud ice flux to parameterize large-scale lightning, *Atmos. Chem.*  
 1398 *Phys.*, 14, 12665–12682, [www.atmos-chem-phys.net/14/12665/2014/](http://www.atmos-chem-phys.net/14/12665/2014/)  
 1399 doi:10.5194/acp-14-12665-2014.
- 1400 Finney, D. L., R. M. Doherty, O. Wild, P. J. Young, and A. Butler (2016), Response of  
 1401 lightning NO<sub>x</sub> emissions and ozone production to climate change: Insights from the  
 1402 Atmospheric Chemistry and Climate Model Intercomparison Project, *Geophys. Res.*  
 1403 *Lett.*, 43, 5492–5500, doi:[10.1002/2016GL068825](https://doi.org/10.1002/2016GL068825).

- 1404 Finney, D. L., R. M. Doherty, O. Wild, D. S. Stevenson, I. A. MacKenzie, and A. M. Blyth  
 1405 (2018), A projected decrease in lightning under climate change, *Nature Climate*  
 1406 *Change*, 8, 210-213.
- 1407 Fiore, A. M., Jacob, D. J., Field, B. D., Streets, D. G., Fernandes, S. D., and Jang, C.: Linking  
 1408 air pollution and climate change: The case for controlling methane, *Geophys. Res.*  
 1409 *Let.*, 29, 1919, doi:10.1029/2002GL015601, 2002.
- 1410 Fiore, A. M., L. W. Horowitz, E. J. Dlugokencky, and J. J. West (2006), Impact of  
 1411 meteorology and emissions on methane trends, 1990–2004, *Geophys. Res. Let.*, 33,  
 1412 L12809, doi:10.1029/2006GL026199.
- 1413 Fisher, B. L., Lamsal, L. N., Fasnacht, Z., Oman, L. D., Joiner, J., Krotkov, N. A., ... &  
 1414 Yang, E. S.: Revised estimates of NO<sub>2</sub> reductions during the COVID-19 lockdowns  
 1415 using updated TROPOMI NO<sub>2</sub> retrievals and model simulations. *Atmospheric*  
 1416 *Environment*, 326, 120459, 2024.
- 1417 Fleming, Z.L., Doherty, R.M., von Schneidmesser, E., Malley, C.S., Cooper, O.R., Pinto,  
 1418 J.P., Colette, A., Xu, X., Simpson, D., Schultz, M.G., Lefohn, A.S., Hamad, S.,  
 1419 Moolla, R., Solberg, S. and Feng, Z., Tropospheric Ozone Assessment Report:  
 1420 Present-day ozone distribution and trends relevant to human health. 2018. *Elem Sci*  
 1421 *Anth*, 6(1), p.12. DOI: 10.1525/elementa.73.
- 1422 Flynn, C. M., K. E. Pickering, J. H. Crawford, A. Weinheimer, K. L. Thornhill, C. Loughner,  
 1423 P. Lee, Variability of O<sub>3</sub> and NO<sub>2</sub> profile shapes during DISCOVER-AQ:  
 1424 Implications for satellite observations and comparisons to model-simulated profiles,  
 1425 *Atmos. Environ.*, 147, 133-156, 2016.
- 1426 Fortems-Cheiney, A., Chevallier, F., Pison, I., Bousquet, P., Szopa, S., Deeter, M. N., and  
 1427 Clerbaux, C.: Ten years of CO emissions as seen from Measurements of Pollution in  
 1428 the Troposphere (MOPITT), *J. Geophys. Res.*, 116, D05304,  
 1429 <https://doi.org/10.1029/2010JD014416>, 2011.
- 1430 Fortems-Cheiney, A., Chevallier, F., Pison, I., Bousquet, P., Saunoy, M., Szopa, S., Cressot,  
 1431 C., Kurosu, T. P., Chance, K., and Fried, A.: The formaldehyde budget as seen by a  
 1432 global-scale multi-constraint and multi-species inversion system, *Atmos. Chem.*  
 1433 *Phys.*, 12, 6699–6721, <https://doi.org/10.5194/acp-12-6699-2012>, 2012.
- 1434 Forster, P., T. Storelvmo, K. Armour, W. Collins, J.-L. Dufresne, D. Frame, D.J. Lunt, T.  
 1435 Mauritsen, M.D. Palmer, M. Watanabe, M. Wild, and H. Zhang, 2021: The Earth's  
 1436 Energy Budget, Climate Feedbacks, and Climate Sensitivity. In *Climate Change*  
 1437 *2021: The Physical Science Basis. Contribution of Working Group I to the Sixth*  
 1438 *Assessment Report of the Intergovernmental Panel on Climate Change [Masson-*  
 1439 *Delmotte, V., P. Zhai, A. Pirani, S.L. Connors, C. Péan, S. Berger, N. Caud, Y. Chen,*  
 1440 *L. Goldfarb, M.I. Gomis, M. Huang, K. Leitzell, E. Lonnoy, J.B.R. Matthews, T.K.*  
 1441 *Maycock, T. Waterfield, O. Yelekçi, R. Yu, and B. Zhou (eds.)]. Cambridge*  
 1442 *University Press, 923 Cambridge, United Kingdom and New York, NY, USA, pp.*  
 1443 *923–1054, doi:10.1017/9781009157896.009, 2021.*
- 1444 Fullekrug, M. E. Williams, C. Price, S. Goodman, R. Holzworth, K. Virts, and D. Buechler  
 1445 (2022) Sidebar 2.1: Lightning, in *State of the Climate: 2021*, *Bull. Amer. Meteor.*  
 1446 *Soc.*, 108, S79-S81, doi:10.1175/BAMS-D-22-0092.1



- 1447 Fung, K. M., Val Martin, M., and Tai, A. P. K.: Modeling the interinfluence of fertilizer-  
1448 induced NH<sub>3</sub> emission, nitrogen deposition, and aerosol radiative effects using  
1449 modified CESM2, *Biogeosciences*, 19, 1635–1655, [https://doi.org/10.5194/bg-19-](https://doi.org/10.5194/bg-19-1635-2022)  
1450 1635-2022, 2022.
- 1451 Gaubert, B., Emmons, L. K., Raeder, K., Tilmes, S., Miyazaki, K., Arellano Jr., A. F., Elguindi,  
1452 N., Granier, C., Tang, W., Barré, J., Worden, H. M., Buchholz, R. R., Edwards, D. P.,  
1453 Franke, P., Anderson, J. L., Saunois, M., Schroeder, J., Woo, J.-H., Simpson, I. J.,  
1454 Blake, D. R., Meinardi, S., Wennberg, P. O., Crouse, J., Teng, A., Kim, M.,  
1455 Dickerson, R. R., He, H., Ren, X., Pusede, S. E., and Diskin, G. S.: Correcting model  
1456 biases of CO in East Asia: impact on oxidant distributions during KORUS-AQ, *Atmos.*  
1457 *Chem. Phys.*, 20, 14617–14647, <https://doi.org/10.5194/acp-20-14617-2020>, 2020.
- 1458 Ghude, S.D., Van der A, R.J., Beig, G., Fadnavis, S., Polade, S.D.: Satellite derived trends in  
1459 NO<sub>2</sub> over the major global hotspot regions during the past decade and their inter-  
1460 comparison. *Environ. Pollut.* 157, 1873–1878. [https://doi.org/10.1016/j.](https://doi.org/10.1016/j.envpol.2009.01.013)  
1461 *envpol.2009.01.013*, 2009.
- 1462 Gaudel, A., Cooper, O.R., Ancellet, G., Barret, B., Boynard, A., Burrows, J.P., Clerbaux, C.,  
1463 Coheur, P.-F., Cuesta, J., Cuevas, E., Doniki, S., Dufour, G., Ebojie, F., Foret, G.,  
1464 Garcia, O., Granados Muños, M.J., Hannigan, J.W., Hase, F., Huang, G., Hassler, B.,  
1465 Hurtmans, D., Jaffe, D., Jones, N., Kalabokas, P., Kerridge, B., Kulawik, S.S., Latter,  
1466 B., Leblanc, T., Le Flochmoën, E., Lin, W., Liu, J., Liu, X., Mahieu, E., McClure-  
1467 Begley, A., Neu, J.L., Osman, M., Palm, M., Petetin, H., Petropavlovskikh, I., Querel,  
1468 R., Rappoe, N., Rozanov, A., Schultz, M.G., Schwab, J., Siddans, R., Smale, D.,  
1469 Steinbacher, M., Tanimoto, H., Tarasick, D.W., Thouret, V., Thompson, A.M.,  
1470 Trickl, T., Weatherhead, E., Wespes, C., Worden, H.M., Vigouroux, C., Xu, X.,  
1471 Zeng, G. and Ziemke, J., Tropospheric Ozone Assessment Report: Present-day  
1472 distribution and trends of tropospheric ozone relevant to climate and global  
1473 atmospheric chemistry model evaluation, *Elem Sci Anth*, 6(1), p.39. DOI:  
1474 10.1525/elementa.291, 2018.
- 1475 Granier, C., Bessagnet, B., Bond, T., D'Angiola, A., Denier van der Gon, H., Frost, G. J., ...  
1476 & van Vuuren, D. P.: Evolution of anthropogenic and biomass burning emissions of  
1477 air pollutants at global and regional scales during the 1980–2010 period. *Climatic*  
1478 *change*, 109, 163-190, 2011.
- 1479 Gelaro, Ronald, et al. "The modern-era retrospective analysis for research and applications,  
1480 version 2 (MERRA-2)." *Journal of climate* 30.14 (2017): 5419-5454.
- 1481 Gódde and Conrad: <https://doi.org/10.1007/s003740000247>
- 1482 Grewe, V., Brunner, D., Dameris, M., Grenfell, J. L., Hein, R., Shindell, D., & Staehelin, J.  
1483 (2001), Origin and variability of upper tropospheric nitrogen oxides and ozone at  
1484 northern mid-latitudes, *Atmos. Env.*, 35, 3421-3433.
- 1485 Griffiths, P. T., Murray, L. T., Zeng, G., Shin, Y. M., Abraham, N. L., Archibald, A. T., Deushi,  
1486 M., Emmons, L. K., Galbally, I. E., Hassler, B., Horowitz, L. W., Keeble, J., Liu, J., Moeni, O.,  
1487 Naik, V., O'Connor, F. M., Oshima, N., Tarasick, D., Tilmes, S., Turnock, S. T., Wild, O.,  
1488 Young, P. J., and Zanis, P.: Tropospheric ozone in CMIP6 simulations, *Atmos. Chem. Phys.*, 21,  
1489 4187–4218, <https://doi.org/10.5194/acp-21-4187-2021>, 2021.

- 1490 Gulev, S.K., P.W. Thorne, J. Ahn, F.J. Dentener, C.M. Domingues, S. Gerland, D. Gong,  
 1491 D.S. Kaufman, H.C. Nnamchi, J. Quaas, J.A. Rivera, S. Sathyendranath, S.L. Smith,  
 1492 B. Trewin, K. von Schuckmann, and R.S. Vose: Changing State of the Climate  
 1493 System. In *Climate Change 2021: The Physical Science Basis. Contribution of*  
 1494 *Working Group I to the Sixth Assessment Report of the Intergovernmental Panel on*  
 1495 *Climate Change* [Masson-Delmotte, V., P. Zhai, A. Pirani, S.L. Connors, C. Péan, S.  
 1496 Berger, N. Caud, Y. Chen, L. Goldfarb, M.I. Gomis, M. Huang, K. Leitzell, E.  
 1497 Lonnoy, J.B.R. Matthews, T.K. Maycock, T. Waterfield, O. Yelekçi, R. Yu, and B.  
 1498 Zhou (eds.)]. Cambridge University Press, Cambridge, United Kingdom and New  
 1499 York, NY, USA, pp. 287–422, doi: [10.1017/9781009157896.004](https://doi.org/10.1017/9781009157896.004), 2021.
- 1500 Hoor, P., Borken-Kleefeld, J., Caro, D., Dessens, O., Endresen, O., Gauss, M., Grewe, V.,  
 1501 Hauglustaine, D., Isaksen, I. S. A., Jöckel, P., Lelieveld, J., Myhre, G., Meijer, E.,  
 1502 Olivie, D., Prather, M., Schnadt Poberaj, C., Shine, K. P., Staehelin, J., Tang, Q., van  
 1503 Aardenne, J., van Velthoven, P., and Sausen, R.: The impact of traffic emissions on  
 1504 atmospheric ozone and OH: results from QUANTIFY, *Atmos. Chem. Phys.*, 9, 3113–  
 1505 3136, <https://doi.org/10.5194/acp-9-3113-2009>, 2009.
- 1506 Holzworth, R. H., Brundell, J. B., McCarthy, M. P., Jacobson, A. R., Rodger, C. J., &  
 1507 Anderson, T. S. (2021). Lightning in the Arctic. *Geophysical Research Letters*, 48,  
 1508 e2020GL091366.  
 1509 <https://doi.org/10.1029/2020GL091366>.
- 1510 Hubert, D., Heue, K.-P., Lambert, J.-C., Verhoelst, T., Allaart, M., Compernelle, S., Cullis,  
 1511 P. D., Dehn, A., Félix, C., Johnson, B. J., Keppens, A., Kollonige, D. E., Lerot, C.,  
 1512 Loyola, D., Maata, M., Mitro, S., Mohamad, M., Piters, A., Romahn, F., Selkirk, H.  
 1513 B., da Silva, F. R., Stauffer, R. M., Thompson, A. M., Veeffkind, J. P., Vömel, H.,  
 1514 Witte, J. C., and Zehner, C.: TROPOMI tropospheric ozone column data: geophysical  
 1515 assessment and comparison to ozonesondes, GOME-2B and OMI, *Atmos Meas Tech*,  
 1516 14, 7405–7433, <https://doi.org/10.5194/amt-14-7405-2021>, 2021.
- 1517 Hudman et al., (2012) [www.atmos-chem-phys.net/12/7779/2012/](http://www.atmos-chem-phys.net/12/7779/2012/)
- 1518 Huntrieser, H., U. Schumann, H. Schlager, H. Höller, A. Giez, H.-D. Betz, D. Brunner, C.  
 1519 Forster, O. Pinto Jr., and R. Calheiros (2008), Lightning activity in Brazilian  
 1520 thunderstorms during TROCCINOX: Implications for NO<sub>x</sub> production, *Atmos. Chem.*  
 1521 *Phys.*, 8, 21–953.
- 1522 Huntrieser, H., H. Schlager, M. Lichtenstern, P. Stock, T. Hamburger, H. Hoeller, K.  
 1523 Schmidt, H.-D. Betz, A. Ulanovsky, and F. Ravegnani (2011) Mesoscale convective  
 1524 systems observed during AMMA and their impact on the NO<sub>x</sub> and O<sub>3</sub> budget over  
 1525 West Africa, *Atmos. Chem. Phys.*, 11, 2503–2536, [www.atmos-chem-](http://www.atmos-chem-phys.net/11/2503/2011)  
 1526 [phys.net/11/2503/2011](http://www.atmos-chem-phys.net/11/2503/2011), doi:10.5194/acp-11-2503-2011
- 1527 Ichoku, C., & Ellison, L.: Global top-down smoke-aerosol emissions estimation using  
 1528 satellite fire radiative power measurements. *Atmospheric Chemistry and*  
 1529 *Physics*, 14(13), 6643-6667, 2014.
- 1530 IPCC, AR5, chrome-  
 1531 extension://efaidnbmnnnibpcajpcgclefindmkaj/[https://www.ipcc.ch/site/assets/upload](https://www.ipcc.ch/site/assets/uploads/2018/03/TAR-06.pdf)  
 1532 [s/2018/03/TAR-06.pdf](https://www.ipcc.ch/site/assets/uploads/2018/03/TAR-06.pdf), 2018.

1533 Isaksen, I.S.A.; Berntsen, T.K.; Dalsøren, S.B.; Eleftheratos, K.; Orsolini, Y.; Rognerud, B.;  
1534 Stordal, F.; Søvde, O.A.; Zerefos, C.; Holmes, C.D. Atmospheric Ozone and Methane  
1535 in a Changing Climate. *Atmosphere*, 5, 518-535.  
1536 <https://doi.org/10.3390/atmos5030518>, 2014.

1537 Janssens-Maenhout, G., Pagliari, V., Guizzardi, D., & Muntean, M.: Global emission  
1538 inventories in the emission database for global atmospheric research (EDGAR)–  
1539 Manual (I). *Gridding: EDGAR emissions distribution on global gridmaps*,  
1540 *Publications Office of the European Union, Luxembourg*, 775, 2013.

1541 Jin, X., Fiore, A., Boersma, K. F., Smedt, I. D., and Valin, L.: Inferring Changes in  
1542 Summertime Surface Ozone–NO<sub>x</sub> –VOC Chemistry over U.S. Urban Areas from  
1543 Two Decades of Satellite and Ground-Based Observations, *Environmental Science*  
1544 *Technology*, 54, 6518–6529, <https://doi.org/10.1021/acs.est.9b07785>, 2020

1545 J. Jung, Y. Choi, S. Mousavinezhad, D. Kang, J. Park, A. Pouyaei, *et al.*: Changes in the  
1546 ozone chemical regime over the contiguous United States inferred by the inversion of  
1547 NO<sub>x</sub> and VOC emissions using satellite observation, *Atmos. Res.*, 270, 106076,  
1548 <https://doi.org/10.1016/j.atmosres.2022.106076>, 2022

1549 Kang, D., K. Foley, R. Mathur, S. Roselle, K. Pickering, and D. Allen, Lightning NO<sub>x</sub>  
1550 Production in CMAQ Part II – Performance Evaluations, *Geosci. Model Devel.*, 12,  
1551 4409–4424, <https://doi.org/10.5194/gmd-12-4409-2019>, 2019.

1552 Kaynak, B., Hu, Y., Martin, R. V., Russell, A. G., Choi, Y., & Wang, Y. (2008). The effect  
1553 of lightning NO<sub>x</sub> production on surface ozone in the continental United States.  
1554 *Atmospheric Chemistry and Physics*, 8, 5151–5159.

1555 Koven et al., (2013) <https://bg.copernicus.org/articles/10/7109/2013/>

1556 Kitagawa, N., (1989) Long-term variations in thunder-day frequencies in Japan. *J. Geophys.*  
1557 *Res.*, 94, 13 183–13 189, <https://doi.org/10.1029/JD094iD11p13183>.

1558 Koehler, T. L. (2020) Cloud-to-Ground Lightning Flash Density and Thunderstorm Day  
1559 Distributions over the Contiguous United States Derived from NLDN Measurements:  
1560 1993–2018, *Mon. Weather Rev.*, DOI: 10.1175/MWR-D-19-0211.1

1561 Kopacz, M., Jacob, D. J., Fisher, J. A., Logan, J. A., Zhang, L., Megretskaia, I. A., Yantosca,  
1562 R. M., Singh, K., Henze, D. K., Burrows, J. P., Buchwitz, M., Khlystova, I., McMillan,  
1563 W. W., Gille, J. C., Edwards, D. P., Eldering, A., Thouret, V., and Nedelec, P.: Global  
1564 estimates of CO sources with high resolution by adjoint inversion of multiple satellite  
1565 datasets (MOPITT, AIRS, SCIAMACHY, TES), *Atmos. Chem. Phys.*, 10, 855–876,  
1566 <https://doi.org/10.5194/acp-10-855-2010>, 2010.

1567 Koshak, W., Peterson, H., Biazar, A., Khan, M., & Wang, L. (2014). The NASA Lightning  
1568 Nitrogen Oxides Model (LNOM): application to air quality modeling. *Atmospheric*  
1569 *Research*, 135, 363-369.

1570 Koshak, W.J., Cummins, K.L., Buechler, D.E., Vant-Hull, B., Blakeslee, R.J., Williams,  
1571 E.R. and Peterson, H.S. (2015) Variability of CONUS lightning in 2003–12 and  
1572 associated impacts. *Journal of Applied Meteorology and Climatology*, 54, 15– 41,  
1573 <https://doi.org/10.1175/JAMC-D-14-0072.1>.

- 1574 Krizan, P. and Lastovicka, J.: Trends in positive and negative ozone laminae in the Northern  
 1575 Hemisphere, *Journal of Geophysical Research: Atmospheres*, 110,  
 1576 <https://doi.org/https://doi.org/10.1029/2004JD005477>, 2005.
- 1577 Labow, G. J., Ziemke, J. R., McPeters, R. D., Haffner, D. P., and Bhartia, P. K.: A total  
 1578 ozone-dependent ozone profile climatology based on ozonesondes and Aura MLS  
 1579 data, *Journal of Geophysical Research: Atmospheres*, 120, 2537–2545,  
 1580 <https://doi.org/10.1002/2014JD022634>, 2015.
- 1581 Labrador, L. J., Kuhlmann, R. V., and Lawrence, M. G. (2005), The effects of lightning-  
 1582 produced NO<sub>x</sub> and its vertical distribution on atmospheric chemistry: sensitivity  
 1583 simulations with MATCH-MPIC, *Atmos. Chem. Phys.*, 5, 1815-1834.
- 1584 Lacis, A. A., Wuebbles, D. J., and Logan, J. A. (1990), Radiative forcing of climate by  
 1585 changes in the vertical distribution of ozone, *J. Geophys. Res.*, 95, 9971-9982.
- 1586 Lamsal, L. N., Duncan, B. N., Yoshida, Y., Krotkov, N. A., Pickering, K. E., Streets, D. G.,  
 1587 Zifeng Lu, Z.: U.S. NO<sub>2</sub> trends (2005–2013): EPA Air Quality System (AQS) data  
 1588 versus improved observations from the Ozone Monitoring Instrument (OMI),  
 1589 *Atmospheric Environment*, <https://doi.org/10.1016/j.atmosenv.2015.03.055>, 2015.
- 1590 Lapierre, J. L., Laughner, J. L., Geddes, J. A., Koshak, W. J., Cohen, R. C., Pusede, S. E.  
 1591 (2020), Observing U.S. regional variability in lightning NO<sub>2</sub> production rates, *J.*  
 1592 *Geophys. Res.*, 125 (5), <https://doi.org/10.1029/2019JD031362>.
- 1593 Lavigne, T., C. Liu, and N. Liu, (2019) How does the trend in thunder days relate to  
 1594 the variation of lightning flash density? *J. Geophys. Res. Atmos.*, 124, 4955–  
 1595 4974, <https://doi.org/10.1029/2018JD029920>
- 1596 Lefohn, AS, Malley, CS, Smith, L, Wells, B, Hazucha, M, Simon, H, Naik, V, Mills, G,  
 1597 Schultz, MG, Paoletti, E, De Marco, A, Xu, X, Zhang, L, Wang, T, Neufeld, HS,  
 1598 Musselman, RC, Tarasick, D, Brauer, M, Feng, Z, Tang, H, Kobayashi, K, Sicard, P,  
 1599 Solberg, S and Gerosa, G, 2018. Tropospheric ozone assessment report: Global ozone  
 1600 metrics for climate change, human health, and crop/ecosystem research. *Elem Sci*  
 1601 *Anth*, 6: 28. DOI: 10.1525/elementa.279.
- 1602 Lelieveld, J.; P. J. Crutzen (1991). The role of clouds in tropospheric photochemistry. , 12(3),  
 1603 229–267. doi:10.1007/bf00048075
- 1604 Liaskos, C. E., Allen, D. J., & Pickering, K. E. (2015), Sensitivity of tropical tropospheric  
 1605 composition to lightning NO<sub>x</sub> production as determined by replay simulations with  
 1606 GEOS-5, *J. Geophys. Res. Atmos.*, 120, 8512–8534, doi:[10.1002/2014JD022987](https://doi.org/10.1002/2014JD022987).
- 1607 Liu, J., Jose M. Rodriguez, Luke D. Oman, Anne R. Douglass, Mark A. Olsen, Lu  
 1608 Hu, Stratospheric impact on the Northern Hemisphere winter and spring ozone  
 1609 interannual variability in the troposphere, *Atmospheric Chemistry and Physics*,  
 1610 10.5194/acp-20-6417-2020, 20, 11, 6417-6433, 2020.
- 1611 Liu, Y., Williams, E. R., Guha, A., & Said, R. (2021), How will lightning change during the  
 1612 pollution-reduced COVID-19 pandemic period? A data study on the global lightning  
 1613 activity, AGU Fall Meeting 2021.
- 1614 Liu et al., (2021) <https://acp.copernicus.org/articles/21/17743/2021/>

- 1615 Liu, J., Strode, S. A., Liang, Q., Oman, L.D., Colarco, P. R., Fleming, E. L., et al. (2022).  
 1616 Change in tropospheric ozone in the recent decades and its contribution to global total  
 1617 ozone. *Journal of Geophysical Research: Atmospheres*, 127, e2022JD037170.  
 1618 <https://doi.org/10.1029/2022JD037170>
- 1619 Li et al. (2011) <https://doi.org/10.1016/j.chnaes.2010.11.006>
- 1620 Luecken, D. J.; Napelenok, S. L.; Strum, M.; Scheffe, R.; Phillips, S. Sensitivity of ambient  
 1621 atmospheric formaldehyde and ozone to precursor species and source types across the  
 1622 united states. *Environ. Sci. Technol.*, 52, 4668–4675, DOI: 10.1021/acs.est.7b05509,  
 1623 2018
- 1624 Marais, E. A., Jacob, D. J., Choi, S., Joiner, J., Belmonte-Rivas, M., Cohen, R. C., et al.  
 1625 (2018). Nitrogen oxides in the global upper troposphere: interpreting cloud-sliced  
 1626 NO<sub>2</sub> observations from the OMI satellite instrument, *Atmospheric Chemistry and*  
 1627 *Physics*, <https://doi.org/10.5194/acp-18-17017-2018>
- 1628 Marais, E. A., Jacob, D. J., Kurosu, T. P., Chance, K., Murphy, J. G., Reeves, C., Mills, G.,  
 1629 Casadio, S., Millet, D. B., Barkley, M. P., Paulot, F., and Mao, J.: Isoprene emissions  
 1630 in Africa inferred from OMI observations of formaldehyde columns, *Atmos. Chem.*  
 1631 *Phys.*, 12, 6219–6235, <https://doi.org/10.5194/acp-12-6219-2012>, 2012.
- 1632 Martin, R. V., Sauvage, B., Folkins, I., Sioris, C. E., Boone, Bernath, C. P., & Ziemke, J.  
 1633 (2007), Space-based constraints on the production of nitric oxide by lightning, *J.*  
 1634 *Geophys. Res.*, 112, D09309, doi:10.1029/2006JD007831.
- 1635 Matandirotya, N.R., Burger, R. An assessment of NO<sub>2</sub> atmospheric air pollution over three  
 1636 cities in South Africa during 2020 COVID-19 pandemic. *Air Qual Atmos Health* 16,  
 1637 263–276 (2023). <https://doi.org/10.1007/s11869-022-01271-3>
- 1638 McDuffie, E. E., Smith, S. J., O'Rourke, P., Tibrewal, K., Venkataraman, C., Marais, E. A.,  
 1639 Zheng, B., Crippa, M., Brauer, M., and Martin, R. V.: A global anthropogenic emission  
 1640 inventory of atmospheric pollutants from sector- and fuel-specific sources (1970–  
 1641 2017): an application of the Community Emissions Data System (CEDS), *Earth Syst.*  
 1642 *Sci. Data*, 12, 3413–3442, <https://doi.org/10.5194/essd-12-3413-2020>, 2020.
- 1643 Meng, L., Liu, J., Tarasick, D. W., Randel, W. J., Steiner, A. K., Wilhelmsen, H., Wang, L.,  
 1644 and Haimberger, L. (2021). Continuous rise of the tropopause in the Northern  
 1645 Hemisphere over 1980–2020. *Science Advances*,  
 1646 <https://doi.org/10.1126/sciadv.abi8065>, 2021.
- 1647 Mills G, Pleijel H, Malley CS, Sinha B, Cooper OR, Schultz MG, Neufeld HS, Simpson D,  
 1648 Sharps K, Feng Z, Gerosa G, Harmens H, Kobayashi K, Saxena P, Paoletti E, Sinha  
 1649 V, Xu X,. [Tropospheric Ozone Assessment Report: Present-day tropospheric ozone](#)  
 1650 [distribution and trends relevant to vegetation](#). *Elem Sci Anth*. 2018;6(1):47. DOI:  
 1651 10.1525/elementa.302.
- 1652 Miyazaki, K., H. J. Eskes, K. Sudo, and C. Zhang, (2014) Global lightning NO<sub>x</sub> production  
 1653 estimated by an assimilation of multiple satellite data sets, *Atmos. Chem Phys.*, 14,  
 1654 3277–3305,  
 1655 [www.atmos-chem-phys.net/14/3277/2014/doi:10.5194/acp-14-3277-2014](http://www.atmos-chem-phys.net/14/3277/2014/doi:10.5194/acp-14-3277-2014).
- 1656 Miyazaki, K., Bowman, K., Sekiya, T., Eskes, H., Boersma, F., Worden, H., Livesey, N.,  
 1657 Payne, V. H., Sudo, K., Kanaya, Y., Takigawa, M., and Ogochi, K.: Updated

1658 tropospheric chemistry reanalysis and emission estimates, TCR-2, for 2005–2018,  
 1659 Earth Syst. Sci. Data, 12, 2223–2259, <https://doi.org/10.5194/essd-12-2223-2020>,  
 1660 2020.

1661 McPeters, R. D. and Labow, G. J.: Climatology 2011: An MLS and sonde derived ozone  
 1662 climatology for satellite retrieval algorithms, *Journal of Geophysical Research:*  
 1663 *Atmospheres*, 117, n/a-n/a, <https://doi.org/10.1029/2011JD017006>, 2012.

1664 Molod, A., Takacs, L., Suarez, M., and Bacmeister, J.: Development of the GEOS-5  
 1665 atmospheric general circulation model: evolution from MERRA to MERRA2,  
 1666 *Geosci. Model Dev.*, 8, 1339–1356, <https://doi.org/10.5194/gmd-8-1339-2015>, 2015.

1667 Murray, L. T. (2018), An uncertain future for lightning, *Nature Climate Change*, 8, 191-192.

1668 Murray, L. T. (2016), Lightning NO<sub>x</sub> and Impacts on Air Quality, *Curr Pollution Rep* (2016)  
 1669 2:115–133, DOI 10.1007/s40726-016-0031-7

1670 Murray, L. T., D. J. Jacob, J. A. Logan, R. C. Hudman, and W. J. Koshak (2012), Optimized  
 1671 regional and interannual variability of lightning in a global chemical transport model  
 1672 constrained by LIS/OTD satellite data, *J. Geophys. Res.*, 117, D20307,  
 1673 doi:[10.1029/2012JD017934](https://doi.org/10.1029/2012JD017934).

1674 Nault, B. A., Garland, C., Wooldridge, J. L., Brune, W. H., Campuzano-Jost, P., Crouse, J.  
 1675 D., et al. (2016). Observational Constraints on the Oxidation of NO<sub>x</sub> in the Upper  
 1676 Troposphere, *The Journal of Physical Chemistry A*, 120 (9), 1468-1478, doi:  
 1677 10.1021/acs.jpca.5b07824

1678 Nault, B. A., Laughner, J. L., Wooldridge, P. J., Crouse, J. D., Dibb, J., Diskin, et al.  
 1679 (2017). Lightning NO<sub>x</sub> emissions: reconciling measured and modeled estimates with  
 1680 updated NO<sub>x</sub> chemistry. *Geophysical Research Letters*, 44, 9479–9488.

1681 Newton, R., Vaughan, G., Ricketts, H. M. A., Pan, L. L., Weinheimer, A. J., and Chemel, C.:  
 1682 Ozone profiles from the West Pacific Warm Pool: measurements and  
 1683 validation, *Atmos Chem Phys*, 16, 619–634, [https://doi.org/10.5194/acp-16-619-](https://doi.org/10.5194/acp-16-619-2016)  
 1684 2016, 2016.

1685 Nielsen, J. Eric, et al. "Chemical mechanisms and their applications in the Goddard Earth  
 1686 Observing System (GEOS) earth system model." *Journal of Advances in Modeling*  
 1687 *Earth Systems* 9.8 (2017): 3019-3044.

1688 Nussbaumer, C. M., Fischer, H., Lelieveld, J., and Pozzer, A.: What controls ozone  
 1689 sensitivity in the upper tropical troposphere?, *Atmos. Chem. Phys.*, 23, 12651–12669,  
 1690 <https://doi.org/10.5194/acp-23-12651-2023>, 2023.

1691 Oleribe OO, Suliman AAA, Taylor-Robinson SD, Corrah T. Possible Reasons Why Sub-  
 1692 Saharan Africa Experienced a Less Severe COVID-19 Pandemic in 2020. *J*  
 1693 *Multidiscip Healthc.* 2021;14:3267-3271, <https://doi.org/10.2147/JMDH.S331847>,  
 1694 2021.

1695 Oltmans, SJ, Lefohn, AS, Shadwick, D, Harris, JM, Scheel, HE, et al.: Recent tropospheric  
 1696 ozone changes — A pattern dominated by slow or no growth, *Atmos. Environ*, 2013.

1697 Orbe, C., Oman, L. D., Strahan, S. E., Waugh, D. W., Pawson, S., Takacs, L. L., and Molod,  
 1698 A. M. (2017). Large-scale atmospheric transport in GEOS replay simulations. *Journal*

- 1699 of Advances in Modeling Earth Systems, 9, 2545–2560.  
1700 <https://doi.org/10.1002/2017MS001053>
- 1701 Ott, L. E., K. E. Pickering, G. L. Stenchikov, H. Huntrieser, and U. Schumann (2007),  
1702 Effects of lightning NO<sub>x</sub> production during the 21 July European Lightning Nitrogen  
1703 Oxides Project storm studied with a three-dimensional cloud-scale chemical transport  
1704 model, *J. Geophys. Res.*, *112*, D05307, doi:10.1029/2006JD007365.
- 1705 Ott, L. E., K. E. Pickering, G. L. Stenchikov, D. J. Allen, A. J. DeCaria, B. Ridley, R.-F. Lin,  
1706 S. Lang, and W.-K. Tao (2010), Production of lightning NO<sub>x</sub> and its vertical  
1707 distribution calculated from three-dimensional cloud-scale chemical transport model  
1708 simulations, *J. Geophys. Res.*, *115*, D04301, doi:10.1029/2009JD011880 Philipona, R.,  
1709 C. Mears, M. Fujiwara, P. Jeannot, P. Thorne, G. Bodeker, L. Haimberger, M. Hervo,  
1710 C. Popp, G. Romanens, W. Steinbrecht, R. Stubi, R. Van Malderen, adiosondes show  
1711 that after decades of cooling, the lower stratosphere is now warming. *J. Geophys.*  
1712 *Res. Atmos.* *123*, 12509–12522 (2018).
- 1713 Pickering, K. E., A. M. Thompson, R. R. Dickerson, W. T. Luke, D. P. McNamara, J. P.  
1714 Greenberg, and P. R. Zimmerman, Model calculations of tropospheric ozone  
1715 production potential following observed convective events, *J. Geophys. Res.*,  
1716 *95*:14,049-14,062, 1990.
- 1717 Pickering, K. E., Y. Wang, W.-K. Tao, C. Price, and J.-F. Mueller, Vertical distributions of  
1718 lightning NO<sub>x</sub> for use in regional and global chemical transport models, *J. Geophys.*  
1719 *Res.*, *103*: 31,203-31,216, 1998.
- 1720 Pickering, K. E., E. Bucsela, D. Allen, A. Ring, R. Holzworth, and N. Krotkov (2016),  
1721 Estimates of lightning NO<sub>x</sub> production based on OMI NO<sub>2</sub> observations over the Gulf  
1722 of Mexico, *J. Geophys. Res. Atmos.*, *121*, doi:[10.1002/2015JD024179](https://doi.org/10.1002/2015JD024179).
- 1723 Pickering, K. E., Y. Li, K. A. Cummings, M. C. Barth, D. J. Allen, E. Bruning, (2023)  
1724 Lightning NO<sub>x</sub> in the May 29-30, 2012 Deep Convective Clouds and Chemistry  
1725 (DC3) Severe Storm and its Downwind Chemical Consequences, *J. Geophys. Res.-*  
1726 *Atmos.*, to be submitted.
- 1727 Pinto, O., Jr., K. P. Naccarato, and I. R. C. A. Pinto, 2013: Thunderstorm incidence in  
1728 southeastern Brazil estimated from different data sources. *Ann. Geophys.*, *31*,  
1729 1213–1219, <https://doi.org/10.5194/angeo-31-1213-2013>.
- 1730 Prodromos Zanis, Dimitris Akritidis, Steven Turnock, Vaishali Naik, Sophie  
1731 Szopa, Aristeidis K Georgoulas, Susanne E Bauer, Makoto Deushi, Larry W  
1732 Horowitz, James Keeble, Climate change penalty and benefit on surface ozone: a  
1733 global perspective based on CMIP6 earth system models, *Environmental Research*  
1734 *Letters*, Volume 17, Number 2, DOI: <https://doi.org/10.1088/1748-9326/ac4a34>.
- 1735 Pollack, I. B., C. R. Homeyer, T. B. Ryerson, K. C. Aikin, J. Peischl, E. C. Apel, T. Campos,  
1736 F. Flocke, R. S. Hornbrook, D. J. Knapp, et al. (2016), Airborne quantification of  
1737 upper tropospheric NO<sub>x</sub> production from lightning in deep convective storms over the  
1738 United States Great Plains, *J. Geophys. Res. Atmos.*, *121*, 2002–2028,  
1739 doi:[10.1002/2015JD023941](https://doi.org/10.1002/2015JD023941).
- 1740 Prather, M. J. and D. J. Jacob (1997) A persistent imbalance in HO<sub>x</sub> and NO<sub>x</sub> photochemistry  
1741 of the upper troposphere driven by deep tropical convection, *Geophys. Res. Lett.*, *24*,  
1742 3189 – 3192.

- 1743 Price, C., J. Penner, and M. Prather (1997), NO<sub>x</sub> from lightning 1. Global distribution based  
1744 on lightning physics, *J. Geophys. Res.*, 102 (D5), 5929-5941.
- 1745 Price, C. G., (2013) Lightning Applications in Weather and Climate Research, *Surv.*  
1746 *Geophys.* (2013) 34:755–767, DOI 10.1007/s10712-012-9218-7
- 1747 Putero, D., Cristofanelli, P., Chang, K.-L., Dufour, G., Beachley, G., Couret, C., Effertz, P.,  
1748 Jaffe, D. A., Kubistin, D., Lynch, J., Petropavlovskikh, I., Puchalski, M., Sharac, T.,  
1749 Sive, B. C., Steinbacher, M., Torres, C., and Cooper, O. R.: Fingerprints of the  
1750 COVID-19 economic downturn and recovery on ozone anomalies at high-elevation  
1751 sites in North America and western Europe, *Atmos. Chem. Phys.*, 23, 15693–15709,  
1752 <https://doi.org/10.5194/acp-23-15693-2023>, 2023.
- 1753 Qie, K., Qie, X., & Tian, W. (2021), Increasing trend of lightning activity in the South Asian  
1754 region, *Science Bulletin*, 66 (1), 78-84.
- 1755 Qie, K., Tian, W., Wang, W., Wu, X., Yuan, T., Tian, H., Luo, J., Zhang, R., & Want, T.  
1756 Regional trends of lightning activity in the tropics and subtropics, *Atmos.*  
1757 *Res.*, 242 (2020), Article 104960, [10.1016/j.atmosres.2020.104960](https://doi.org/10.1016/j.atmosres.2020.104960)
- 1758 Randel, W. J., L. Polvani, F. Wu, D. E. Kinnison, C.-Z. Zou, C. Mears, Troposphere  
1759 stratosphere temperature trends derived from satellite data compared with ensemble  
1760 simulations from WACCM. *J. Geophys. Res. Atmos.* 122, 9651–9667 (2017).
- 1761 Ren, X., J. R. Olson, J. H. Crawford, W. H. Brune, J. Mao, R. B. Long, G. Chen, M. A.  
1762 Avery, G. W. Sachse, J. D. Barrick, G. S. Diskin, L. G. Huey, Alan Fried, Ronald C.  
1763 Cohen, Brian Heikes, Paul Wennberg, Hanwant B. Singh, Donald R. Blake, Richard  
1764 E. Shetter,(2008) HO<sub>x</sub> Chemistry during INTEX–A 2004: Observation, Model  
1765 Calculations and comparison with previous studies, *J. Geophys. Res.*, 113, D05310,  
1766 doi:10.1029/2007JD009166.
- 1767 Ridley, B., Ott, L., Pickering, K., Emmons, L., Montzka, D., Weinheimer, A., et al. (2004),  
1768 Florida thunderstorms: A faucet of reactive nitrogen to the upper troposphere, *J.*  
1769 *Geophys. Res.*, 109 (D17), [10.1029/2004JD004769](https://doi.org/10.1029/2004JD004769).
- 1770 Romps, D. M., Seeley, J. T., Vollaro, D., & Molinar, J. (2014), Projected increase in  
1771 lightning strikes in the United States due to global warming, *Science*, 851-854.
- 1772 Romps, D. M., Charn, A. B., Holzworth, R. H., Lawrence, W. E., Molinari, J., & Vollaro, D.  
1773 (2018). CAPE times P explains lightning over land but not the land-ocean contrast.  
1774 *Geophysical Research Letters*, 45, 12,623–12,630.  
1775 <https://doi.org/10.1029/2018GL080267>
- 1776 Romps, D. M. (2019). Evaluating the future of lightning in cloud-resolving models.  
1777 *Geophysical Research Letters*, 46, <https://doi.org/10.1029/2019GL085748>
- 1778 Sanap, S. D. (2021) Global and regional variations in aerosol loading during COVID-19  
1779 imposed lockdown, *Atmos. Environ.*, 246, <https://doi.org/10.1016/j.atmosenv.2020.118132>.
- 1780 Sauvage, B., R. V. Martin, A. van Donkelaar, and J. R. Ziemke (2007) Quantification of the  
1781 factors controlling tropical tropospheric ozone and the South Atlantic maximum, *J.*  
1782 *Geophys. Res.*, 112, D11309, doi:10.1029/2006JD008008.
- 1783 Sanap, S. D. (2021) Global and regional variations in aerosol loading during COVID-19



- 1784 imposed lockdown, *Atmos. Environ.*, 246, <https://doi.org/10.1016/j.atmosenv.2020.118132>.
- 1785 Sauvage, B., R. V. Martin, A. van Donkelaar, and J. R. Ziemke (2007) Quantification of the  
1786 factors controlling tropical tropospheric ozone and the South Atlantic maximum, *J.*  
1787 *Geophys. Res.*, 112, D11309, doi:10.1029/2006JD008008.
- 1788 Sanap, S. D. (2021) Global and regional variations in aerosol loading during COVID-19  
1789 imposed lockdown, *Atmos. Environ.*, 246, <https://doi.org/10.1016/j.atmosenv.2020.118132>.
- 1790 Saunio, M., R. Stavert, A., Poulter, B., Bousquet, P., G. Canadell, J., B. Jackson, R., A.  
1791 Raymond, P., J. Dlugokencky, E., Houweling, S., K. Patra, P., Ciais, P., K. Arora, V.,  
1792 Bastviken, D., Bergamaschi, P., R. Blake, D., Brailsford, G., Bruhwiler, L., M.  
1793 Carlson, K., Carrol, M., Castaldi, S., Chandra, N., Crevoisier, C., M. Crill, P., Covey,  
1794 K., L. Curry, C., Etiope, G., Frankenberg, C., Gedney, N., I. Hegglin, M., Höglund-  
1795 Isaksson, L., Hugelius, G., Ishizawa, M., Ito, A., Janssens-Maenhout, G., M. Jensen,  
1796 K., Joos, F., Kleinen, T., B. Krummel, P., L. Langenfelds, R., G. Laruelle, G., Liu, L.,  
1797 MacHida, T., Maksyutov, S., C. McDonald, K., McNorton, J., A. Miller, P., R.  
1798 Melton, J., Morino, I., Müller, J., Murguia-Flores, F., Naik, V., Niwa, Y., Noce, S.,  
1799 O'Doherty, S., J. Parker, R., Peng, C., Peng, S., P. Peters, G., Prigent, C., Prinn, R.,  
1800 Ramonet, M., Regnier, P., J. Riley, W., A. Rosentreter, J., Segers, A., J. Simpson, I.,  
1801 Shi, H., J. Smith, S., Paul Steele, L., F. Thornton, B., Tian, H., Tohjima, Y., N.  
1802 Tubiello, F., Tsuruta, A., Viovy, N., Voulgarakis, A., S. Weber, T., Van Weele, M.,  
1803 R. Van Der Werf, G., F. Weiss, R., Worthy, D., Wunch, D., Yin, Y., Yoshida, Y.,  
1804 Zhang, W., Zhang, Z., Zhao, Y., Zheng, B., Zhu, Q., Zhu, Q., and Zhuang, Q.: The  
1805 global methane budget 2000-2017, *Earth Syst Sci Data*, 12,  
1806 <https://doi.org/10.5194/essd-12-1561-2020>, 2020.
- 1807 Sauvage, B., R. V. Martin, A. van Donkelaar, and J. R. Ziemke (2007) Quantification of the  
1808 factors controlling tropical tropospheric ozone and the South Atlantic maximum, *J.*  
1809 *Geophys. Res.*, 112, D11309, doi:10.1029/2006JD008008.
- 1810 Schumann, U., and H. Huntrieser (2007), The global lightning-induced nitrogen oxides  
1811 source, *Atmos. Chem. Phys.*, 7, 3823-3907.
- 1812 Seguel, R. J., Castillo, L., Opazo, C., Rojas, N. Y., Nogueira, T., Cazorla, M., Gavidia-  
1813 Calderón, M., Gallardo, L., Garreaud, R., Carrasco-Escaff, T., and Elshorbany, Y.:  
1814 Changes in South American Surface Ozone Trends: Exploring the Influences of  
1815 Precursors and Extreme Events, *EGUsphere* [preprint],  
1816 <https://doi.org/10.5194/egusphere-2024-328>, 2024.
- 1817 Sen, P (1968). Estimated of the regression coefficient based on Kendall's Tau. *J Am Stat*  
1818 *Assoc* 39:1379-1389
- 1819 Shi, Z., H. Wang, Y. Tan, L. Li, C. Li, (2020) Influence of aerosols on lightning activities in  
1820 central eastern parts of China, *Atmos Sci Lett.*, 21:e957,  
1821 <https://doi.org/10.1002/asl.957>.
- 1822 Sokhi, R. S., Singh, V., Querol, X., Finardi, S., Targino, A. C., Andrade, M. de F., Pavlovic,  
1823 R., Garland, R. M., Massagué, J., Kong, S., Baklanov, A., Ren, L., Tarasova, O.,  
1824 Carmichael, G., Peuch, V. H., Anand, V., Arbilla, G., Badali, K., Beig, G.,  
1825 Belalcazar, L. C., Bolignano, A., Brimblecombe, P., Camacho, P., Casallas, A.,  
1826 Charland, J. P., Choi, J., Chourdakis, E., Coll, I., Collins, M., Cyrus, J., da Silva, C.  
1827 M., Di Giosa, A. D., Di Leo, A., Ferro, C., Gavidia-Calderon, M., Gayen, A.,

- 1828 Ginzburg, A., Godefroy, F., Gonzalez, Y. A., Guevara-Luna, M., Haque, S. M.,  
 1829 Havenga, H., Herod, D., Hörrak, U., Hussein, T., Ibarra, S., Jaimes, M., Kaasik, M.,  
 1830 Khaiwal, R., Kim, J., Kousa, A., Kukkonen, J., Kulmala, M., Kuula, J., La Violette,  
 1831 N., Lanzani, G., Liu, X., MacDougall, S., Manseau, P. M., Marchegiani, G.,  
 1832 McDonald, B., Mishra, S. V., Molina, L. T., Mooibroek, D., Mor, S., Moussiopoulos,  
 1833 N., Murena, F., Niemi, J. V., Noe, S., Nogueira, T., Norman, M., Pérez-Camaño, J.  
 1834 L., Petäjä, T., Piketh, S., Rathod, A., Reid, K., Retama, A., Rivera, O., Rojas, N. Y.,  
 1835 Rojas-Quincho, J. P., San José, R., Sánchez, O., Seguel, R. J., Sillanpää, S., Su, Y.,  
 1836 Tapper, N., Terrazas, A., Timonen, H., Toscano, D., Tsegas, G., Velders, G. J. M.,  
 1837 Vlachokostas, C., von Schneidmesser, E., VPM, R., Yadav, R., Zalakeviciute, R.,  
 1838 and Zavala, M.: A global observational analysis to understand changes in air quality  
 1839 during exceptionally low anthropogenic emission conditions, *Environ Int*, 157,  
 1840 <https://doi.org/10.1016/j.envint.2021.106818>, 2021.
- 1841 Souri, A. H., Johnson, M. S., Wolfe, G. M., Crawford, J. H., Fried, A., Wisthaler, A., Brune,  
 1842 W. H., Blake, D. R., Weinheimer, A. J., Verhoelst, T., Compernelle, S., Pinardi, G.,  
 1843 Vigouroux, C., Langerock, B., Choi, S., Lamsal, L., Zhu, L., Sun, S., Cohen, R. C.,  
 1844 Min, K.-E., Cho, C., Philip, S., Liu, X., and Chance, K.: Characterization of errors in  
 1845 satellite-based HCHONO<sub>2</sub> tropospheric column ratios with respect to chemistry,  
 1846 column-to-PBL translation, spatial representation, and retrieval uncertainties,  
 1847 *Atmospheric Chemistry and Physics*, 23, 1963–1986, [https://doi.org/10.5194/acp-23-](https://doi.org/10.5194/acp-23-1963-2023)  
 1848 [1963-2023](https://doi.org/10.5194/acp-23-1963-2023), 2023
- 1849 Stauffer, R. M., Thompson, A. M., Kollonige, D., Tarasick, D., Van Malderen, R., Smit, H.  
 1850 G. J., Vömel, H., Morris, G., Johnson, B. J., Cullis, P., and et al.: An Examination of  
 1851 the Recent Stability of Ozone Global Network Data, *Earth and Space Science*  
 1852 *Open Archive*, 48, <https://doi.org/10.1002/essoar.10511590.1>, 2022.
- 1853 Steinbrecht, W., Claude, H., Köhler, U., and Hoinka, K. P.: Correlations between tropopause  
 1854 height and total ozone: Implications for long-term changes, *J. Geophys. Res.*, 103,  
 1855 19183–19192, <https://doi.org/10.1029/98JD01929>, 1998.
- 1856 Steinbrecht, W., Kubistin, D., Plass-Dülmer, C., Davies, J., Tarasick, D. W., von der  
 1857 Gathen, P., et al.: COVID-19 crisis reduces free tropospheric ozone across the Northern  
 1858 Hemisphere. *Geophysical Research Letters*, 48, e2020GL091987.  
 1859 <https://doi.org/10.1029/2020GL091987>, 2021
- 1860 Steiner, A. K., F. Ladst.ter, W. J. Randel, A. C. Maycock, Q. Fu, C. Claud, H. Gleisner, L.  
 1861 Haimberger, S. -P. Ho, P. Keckhut, T. Leblanc, C. Mears, L. M. Polvani, B. D.  
 1862 Santer, T. Schmidt, V. Sofieva, R. Wing, C. -Z. Zou, Observed temperature changes  
 1863 in the troposphere and stratosphere from 1979 to 2018. *J. Climate* 33, 8165–8194  
 1864 (2020).
- 1865 Stohl, A., Bonasoni, P., Cristofanelli, P., Collins, W., Feichter, J., Frank, A., Forster, C.,  
 1866 Gerasopoulos, E., Gäggeler, H., James, P., Kentarchos, T., Kromp-Kolb, H., Krüger,  
 1867 B., Land, C., Meloen, J., Papayannis, A., Priller, A., Seibert, P., Sprenger, M.,  
 1868 Roelofs, G. J., Scheel, H. E., Schnabel, C., Siegmund, P., Tobler, L., Trickl, T.,  
 1869 Wernli, H., Wirth, V., Zanis, P., and Zerefos, C.: Stratosphere-troposphere exchange:  
 1870 A review, and what we have learned from STACCATO, *J. Geophys. Res.*, 108, 8516,  
 1871 <https://doi.org/10.1029/2002JD002490>, 2003.

- 1872 Strahan, S. E., Duncan, B. N., and Hoor, P. (2007). Observationally derived transport  
 1873 diagnostics for the lowermost stratosphere and their application to the GMI chemistry  
 1874 and transport model. *Atmospheric Chemistry and Physics*, 7(9), 2435–2445.  
 1875 <https://doi.org/10.5194/acp-7-2435-2007>.
- 1876 Sue et al. 2011: <https://doi.org/10.1126/science.1208839>
- 1877 Schultz, M.G., Schröder, S., Lyapina, O., Cooper, O., Galbally, I., Petropavlovskikh, I., von  
 1878 Schneidmesser, E., Tanimoto, H., Elshorbany, Y., Naja, M., Seguel, R., Dauert, U.,  
 1879 Eckhardt, P., Feigenspahn, S., Fiebig, M., Hjellbrekke, A.-G., Hong, Y.-D., Christian  
 1880 Kjeld, P., Koide, H., Lear, G., Tarasick, D., Ueno, M., Wallasch, M., Baumgardner,  
 1881 D., Chuang, M.-T., Gillett, R., Lee, M., Molloy, S., Moolla, R., Wang, T., Sharps, K.,  
 1882 Adame, J.A., Ancellet, G., Apadula, F., Artaxo, P., Barlasina, M., Bogucka, M.,  
 1883 Bonasoni, P., Chang, L., Colomb, A., Cuevas, E., Cupeiro, M., Degorska, A., Ding,  
 1884 A., Fröhlich, M., Frolova, M., Gadhavi, H., Gheusi, F., Gilge, S., Gonzalez, M.Y.,  
 1885 Gros, V., Hamad, S.H., Helmig, D., Henriques, D., Hermansen, O., Holla, R., Huber,  
 1886 J., Im, U., Jaffe, D.A., Komala, N., Kubistin, D., Lam, K.-S., Laurila, T., Lee, H.,  
 1887 Levy, I., Mazzoleni, C., Mazzoleni, L., McClure-Begley, A., Mohamad, M., Murovic,  
 1888 M., Navarro-Comas, M., Nicodim, F., Parrish, D., Read, K.A., Reid, N., Ries, L.,  
 1889 Saxena, P., Schwab, J.J., Scorgie, Y., Senik, I., Simmonds, P., Sinha, V., Skorokhod,  
 1890 A., Spain, G., Spangl, W., Spoor, R., Springston, S.R., Steer, K., Steinbacher, M.,  
 1891 Suharguniyawan, E., Torre, P., Trickl, T., Weili, L., Weller, R., Xu, X., Xue, L. and  
 1892 Zhiqiang, M., *Tropospheric Ozone Assessment Report: Database and Metrics Data of*  
 1893 *Global Surface Ozone Observations*. 2017. *Elem Sci Anth*, 5, p.58. DOI:  
 1894 [10.1525/elementa.244](https://doi.org/10.1525/elementa.244).
- 1895 Szopa, S., Naik, V., Adhikary, B., Artaxo, P., Berntsen, T., Collins, W.D., Fuzzi, S.,  
 1896 Gallardo, L., Kiendler-Scharr, A., Klimont, Z., Liao, H., Unger, N., and Zanis, P.:  
 1897 Short-Lived Climate Forcers. In *Climate Change 2021: The Physical Science Basis.*  
 1898 *Contribution of Working Group I to the Sixth Assessment Report of the*  
 1899 *Intergovernmental Panel on Climate Change* [Masson-Delmotte, V., P. Zhai,  
 1900 A. Pirani, S.L. Connors, C. Péan, S. Berger, N. Caud, Y. Chen, L. Goldfarb,  
 1901 M.I. Gomis, M. Huang, K. Leitzell, E. Lonnoy, J.B.R. Matthews, T.K. Maycock,  
 1902 T. Waterfield, O. Yelekçi, R. Yu, and B. Zhou (eds.)]. Cambridge University Press,  
 1903 Cambridge, United Kingdom and New York, NY, USA, pp. 817–922,  
 1904 doi:[10.1017/9781009157896.008](https://doi.org/10.1017/9781009157896.008), 2021.
- 1905 Tarasick, D., Galbally, I.E., Cooper, O.R., Schultz, M.G., Ancellet, G., Leblanc, T.,  
 1906 Wallington, T.J., Ziemke, J., Liu, X., Steinbacher, M., Staehelin, J., Vigouroux, C.,  
 1907 Hannigan, J.W., García, O., Foret, G., Zanis, P., Weatherhead, E., Petropavlovskikh,  
 1908 I., Worden, H., Osman, M., Liu, J., Chang, K.-L., Gaudel, A., Lin, M., Granados-  
 1909 Muñoz, M., Thompson, A.M., Oltmans, S.J., Cuesta, J., Dufour, G., Thouret, V.,  
 1910 Hassler, B., Trickl, T. and Neu, J.L., 2019. *Tropospheric Ozone Assessment Report:*  
 1911 *Tropospheric ozone from 1877 to 2016, observed levels, trends and uncertainties.*  
 1912 *Tropospheric Ozone Assessment Report: Tropospheric ozone from 1877 to 2016,*  
 1913 *observed levels, trends and uncertainties.* *Elem Sci Anth*, 7(1), p.39. DOI :  
 1914 [10.1525/elementa.376](https://doi.org/10.1525/elementa.376), 2019.
- 1915 Thompson, A. M., Witte, J. C., Sterling, C., Jordan, A., Johnson, B. J., Oltmans, S. J.,  
 1916 Fujiwara, M., Vömel, H., Allaart, M., Piters, A., Coetzee, G. J. R., Posny, F.,  
 1917 Corrales, E., Diaz, J. A., Félix, C., Komala, N., Lai, N., Ahn Nguyen, H. T., Maata,

- 1918 M., Mani, F., Zainal, Z., Ogino, S., Paredes, F., Penha, T. L. B., Silva, F. R., Sallons-  
 1919 Mitro, S., Selkirk, H. B., Schmidlin, F. J., Stübi, R., and Thiongo, K.: First  
 1920 Reprocessing of Southern Hemisphere Additional Ozonesondes (SHADOZ) Ozone  
 1921 Profiles (1998–2016): 2. Comparisons With Satellites and Ground-Based Instruments,  
 1922 Journal of Geophysical Research: Atmospheres, 122,  
 1923 <https://doi.org/10.1002/2017JD027406>, 2017.
- 1924 Tsvilidou, M., Sauvage, B., Barret, B., Wolff, P., Clark, H., Bennouna, Y., Blot, R.,  
 1925 Boulanger, D., Nédélec, P., Le Flochmoën, E., and Thouret, V.: Tropical tropospheric  
 1926 ozone and carbon monoxide distributions: characteristics, origins and control factors,  
 1927 as seen by IAGOS and IASI, Atmos. Chem. Phys. Discuss. (preprint),  
 1928 <https://doi.org/10.5194/acp-2022-686>, in review, 2022.
- 1929 Turnock, S. T., Allen, R. J., Andrews, M., Bauer, S. E., Deushi, M., Emmons, L., Good, P.,  
 1930 Horowitz, L., John, J. G., Michou, M., Nabat, P., Naik, V., Neubauer, D., O'Connor,  
 1931 F. M., Olivié, D., Oshima, N., Schulz, M., Sellar, A., Shim, S., Takemura, T., Tilmes,  
 1932 S., Tsigaridis, K., Wu, T., and Zhang, J.: Historical and future changes in air  
 1933 pollutants from CMIP6 models, Atmos. Chem. Phys., 20, 14547–14579,  
 1934 <https://doi.org/10.5194/acp-20-14547-2020>, 2020.
- 1935 Theil, H. (1950), “A rank-invariant method of linear and polynomial regression analysis. I,  
 1936 II, III”, Nederl. Akad. Wetensch., Proc., 53: 386–392, 521–525, 1397–1412.
- 1937 Trickl, T., Bärtsch-Ritter, N., Eisele, H., Furger, M., Mücke, R., Sprenger, M., and Stohl, A.:  
 1938 High-ozone layers in the middle and upper troposphere above Central Europe:  
 1939 potential import from the stratosphere along the subtropical jet stream, Atmos. Chem.  
 1940 Phys., 11, 9343–9366, <https://doi.org/10.5194/acp-11-9343-2011>, 2011.
- 1941 Verma, S., Yadava, P. K., Lal, D. M., Mall, R. K., Harshbardhan, K., & Payra, S. (2021),  
 1942 Role of Lightning NO<sub>x</sub> in ozone formation: A review, Pure and Applied Geophysics,  
 1943 178, 1425-1443.
- 1944 Wang, H., Shi, Z., Wang, X., Tan, Y., Wang, H., Li, L., & Lin, X. (2021), Cloud-to-Ground  
 1945 Lightning Response to Aerosol over Air-Polluted Urban Areas in China. *Remote*  
 1946 *Sens.* 13, 2600. <https://doi.org/10.3390/rs13132600>
- 1947 Wang, H., Lu, X., Jacob, D. J., Cooper, O. R., Chang, K.-L., Li, K., Gao, M., Liu, Y., Sheng,  
 1948 B., Wu, K., Wu, T., Zhang, J., Sauvage, B., Nédélec, P., Blot, R., and Fan, S.: Global  
 1949 tropospheric ozone trends, attributions, and radiative impacts in 1995–2017: an  
 1950 integrated analysis using aircraft (IAGOS) observations, ozonesonde, and multi-  
 1951 decadal chemical model simulations, Atmos Chem Phys, 22, 13753–13782,  
 1952 <https://doi.org/10.5194/acp-22-13753-2022>, 2022.
- 1953 Wang, Y., A. W. DeSilva, G. C. Goldenbaum, and R. R. Dickerson, (1998) Nitric oxide  
 1954 production by simulated lightning: Dependence on current, energy, and pressure, *J.*  
 1955 *Geophys. Res.*, 103, 19,149-19,159.
- 1956 Wilcox, R. (2001). Fundamentals of Modern Statistical Methods: Substantially Improving  
 1957 Power and Accuracy. Springer Science and Business Media.
- 1958 Williams, R. S., Hegglin, M. I., Kerridge, B. J., Jöckel, P., Latter, B. G., and Plummer, D. A.:  
 1959 Characterising the seasonal and geographical variability in tropospheric ozone,  
 1960 stratospheric influence and recent changes, Atmos. Chem. Phys., 19, 3589–3620,  
 1961 <https://doi.org/10.5194/acp-19-3589-2019>, 2019.

- 1962 Wu, D., Zhang, J., Wang, M., An, J., Wang, R., Haider, H., et al. (2022). Global and regional  
 1963 patterns of soil nitrous acid emissions and their acceleration of rural photochemical  
 1964 reactions. *Journal of Geophysical Research: Atmospheres*, 127, e2021JD036379.  
 1965 <https://doi.org/10.1029/2021JD036379>
- 1966 WMO, 1992, *International Meteorological Vocabulary* (2nd ed.), Geneva: Secretariat of the  
 1967 World Meteorological Organization. 1992. p. 636. ISBN 978-92-63-02182-3)
- 1968 Wang and Chen, 2012: <https://doi.org/10.1016/j.geoderma.2011.11.009>
- 1969 Xue, X., Ren, G. Y., Xu, X. D., Sun, X. B., Yang, G. W., Zhang, P. F., & Zhang, S. Q.  
 1970 (2021), The trends of warm-season thunderstorm and lightning days in China and the  
 1971 influence of environmental factors, *J. Geophys. Res.*, 126 (15),  
 1972 10.1029/2021JD034950.
- 1973 Yang, X., and Z. Li, 2014: Increases in thunderstorm activity and relationships with air  
 1974 pollution in southeast China, *J. Geophys. Res. Atmos.*, 119, 1835–1844,  
 1975 doi:10.1002/2013JD021224.
- 1976 Yin, Y., Chevallier, F., Ciais, P., Broquet, G., Fortems-Cheiney, A., Pison, I., and Saunois, M.:  
 1977 Decadal trends in global CO emissions as seen by MOPITT, *Atmos. Chem. Phys.*, 15,  
 1978 13433–13451, <https://doi.org/10.5194/acp-15-13433-2015>, 2015.
- 1979 Young, P.J., Naik, V., Fiore, A.M., Gaudel, A., Guo, J., Lin, M.Y., Neu, J.L., Parrish, D.D.,  
 1980 Rieder, H.E., Schnell, J.L., Tilmes, S., Wild, O., Zhang, L., Ziemke, J.R., Brandt, J.,  
 1981 Delcloo, A., Doherty, R.M., Geels, C., Hegglin, M.I., Hu, L., Im, U., Kumar, R.,  
 1982 Luhar, A., Murray, L., Plummer, D., Rodriguez, J., Saiz-Lopez, A., Schultz, M.G.,  
 1983 Woodhouse, M.T. and Zeng, G. Tropospheric Ozone Assessment Report: Assessment  
 1984 of global-scale model performance for global and regional ozone distributions,  
 1985 variability, and trends. 2018. *Elem Sci Anth*, 6(1), p.10. DOI: 10.1525/elementa.265.
- 1986 Zeng, G., Morgenstern, O., Braesicke, P., Pyle, J.A., 2010. Impact of stratospheric ozone  
 1987 recovery on tropospheric ozone and its budget: impact of ozone recovery on  
 1988 tropospheric ozone. *Geophys. Res. Lett.* 37, n/a-n/a. [https://doi.org/10.1029/](https://doi.org/10.1029/2010GL042812)  
 1989 2010GL042812.
- 1990 Yetong Li, Yan Xia, Fei Xie, Yingying Yan, Influence of stratosphere-troposphere exchange  
 1991 on long-term trends of surface ozone in CMIP6, *Atmospheric Research*, 297, doi:  
 1992 <https://doi.org/10.1016/j.atmosres.2023.107086>, 2024.
- 1993 Zhang, X., Yin, Y., van der A, R., Lapierre, J. L., Chen, Q., Kuang, X., Yan, S., Chen, J., He,  
 1994 C., and Shi, R. (2020), Estimates of lightning NO<sub>x</sub> production based on high-  
 1995 resolution OMI NO<sub>2</sub> retrievals over the continental US, *Atmos. Meas. Tech.*, 13,  
 1996 1709–1734, <https://doi.org/10.5194/amt-13-1709-2020> .
- 1997 Zhang et al., 2020: <https://doi.org/10.1016/j.atmosenv.2020.117596>
- 1998 Zhang, L., T. Wang, Q. Zhang, J. Zheng, Z. Xu, and M. Lv (2016), Potential sources of nitrous  
 1999 acid (HONO) and their impacts on ozone: A WRF-Chem study in a polluted subtropical  
 2000 region, *J. Geophys. Res. Atmos.*, 121, 3645–3662, doi:10.1002/2015JD024468.
- 2001 Zheng, B.; Chevallier, F.; Yin, Y.; Ciais, P.; Fortems-Cheiney, A.; Deeter, M.N.; Parker,  
 2002 R.J.; Wang, Y.; Worden, H.M.; Zhao, Y. Global atmospheric carbon monoxide  
 2003 budget 2000-2017 inferred from multi-species atmospheric inversions. *Earth Sys. Sci.*  
 2004 *Data*, 11, 1411–1436, <https://doi.org/10.5194/essd-11-1411-2019>, 2019